Mathematics and Computations of Liquid Crystal Elastomers

Rabin Poudel

A thesis submitted in candidature for the degree of

Doctor of Philosophy

Cardiff University

March 2026

Abstract

Liquid crystal elastomers (LCEs) are soft materials in which liquid crystal (LC) mesogens are covalently attached to a polymer network while retaining the ability to freely re-orient relative to the polymer matrix. This coupling between polymer deformation and LC rotation leads to complex mechanical behaviours, particularly when the material is subjected to external loads. In this thesis, a theoretical and computational framework is developed to model the elastic and viscous responses of nematic LCEs. The approach combines large-strain viscoelastic responses of the polymer network with the viscoelastic rotation of the nematic director, allowing the separate yet interacting mechanisms to be represented within a unified constitutive model. A finite element framework is formulated and implemented to approximate the resulting nonlinear viscoelastic behaviour. The occurrence of different localisation mechanisms in inhomogeneous deformation characteristic of LCEs can be demonstrated both theoretically and numerically using this framework. Numerical simulations successfully reproduce the mechanical phenomena and illustrate the influence of model parameters during loading and unloading. The modelling approach also provides a foundation for incorporating more complex constitutive functions and additional couplings with environmental stimuli.

Contents

Abstract **i**

Acknowledgements **vi**

1 Introduction **1**

2 Theory of liquid crystal elastomers **7**

2.1 Theory of liquid crystals 8

2.2 Continuum theory of LCEs 10

2.2.1 Kinematics 10

2.2.2 Balance of linear momentum 15

2.2.3 Thermodynamics consideration 17

2.2.4 Constitutive functions for uniaxial LCEs 22

3 Key instabilities in LCEs **26**

3.1 Shear striping instability 26

3.1.1 Analysis of shear striping under uniaxial stress 27

3.1.2 Optimal stripe width 35

3.2 Necking 37

3.2.1 Neoclassical model cannot predict necking 39

3.3 Discussion 41

4 Viscoelasticity in LCEs **43**

4.1 Coupled viscoelastic response 43
4.2 Continuum models for viscoelastic response 44
4.2.1 Kinematics and model function 45
4.2.2 Thermodynamics consistency and evolution equations . 47
4.3 Discussion 48

5 Finite element formulation **50**
5.1 Strong form in reference configuration 50
5.2 Weak formulation by the principle of virtual work 51
5.3 Mixed variational formulation 53
5.4 Linearization of the variational form 58
5.5 Discretization 60
5.5.1 Concept of isoparametric element 62
5.5.2 Discretization of kinematic quantities 65
5.5.3 Discretization of variational formulation 69
5.5.4 Discretization of linearized variational formulation . . . 71
5.6 Discussion 76

6 Numerical simulations **78**
6.1 Set up of boundary value problem 78
6.2 Simulation of elastic model for an LCE 79
6.2.1 Stretching at angle $\theta_0 = 80^\circ$ to initial director 80
6.2.2 Stretching at angle $\theta_0 = 90^\circ$ to initial director 82
6.3 Simulation of necking in an LCE sample 86
6.4 Simulation of the viscoelastic model 88
6.4.1 Vertical initial director 88
6.4.2 Non-vertical initial director 90
Effect of anisotropy parameter a 93

Effect of constitutive parameters $\mu_{neq}^{(1)}$ and $\eta^{(1)}$ for viscous director rotation 94

Effect of constitutive parameters $\mu_{neq}^{(2)}$ and $\eta^{(2)}$ for viscous polymer network 96

7 Conclusion **97**

A Stresses and their derivatives **99**

A.1 Strain-energy density function 99

Bibliography **102**

From falsehood lead me to truth,

From darkness lead me to light,

From death lead me to immortality.

Brihadaranyaka Upanishad 1.3.28

Acknowledgements

First and foremost, I would like to express my deepest gratitude to my supervisors, Dr. Yasemin Şengül Tezel and Prof. Angela Mihai for their invaluable guidance, patience, and support that ultimately led to this work. Their unwavering belief in my potential, even when I doubted it myself, has been the cornerstone of my development. Next, I wish to thank the School of Mathematics for the award of a full studentship, which provided the financial security necessary to focus entirely on my research. The School and its staff have provided a vibrant and intellectually stimulating environment that has made my time here truly rewarding.

Next, I extend my sincere thanks to Prof. Samuel Evans for his technical support during the initial stage of my work with FEBio. His guidance was instrumental in helping me navigate the software's complexities and set the foundation for programming the computational model.

Furthermore, I would like to acknowledge the organisers of the research programme "Uncertainty quantification and stochastic modelling of material" for hosting me for two weeks in such a stimulating academic environment at the Isaac Newton Institute for Mathematical Sciences, University of Cambridge, in summer 2023. This experience allowed me to engage with a broader research community. I would specifically thank Dr. Ajay B. Harish and Dr. Yang Liu for the insightful discussions whose perspectives provided a fresh impetus to my work at a crucial stage.

Moreover, I owe a great debt to all my previous teachers from my early schooling through to my master's degrees. Each of them has contributed a brick to the foundation of my knowledge upon which this entire research has been built.

On a personal note, I would like to express my deepest thanks to my wife, Preety Rakhal. She has been my anchor through the inevitable frustrations and low points of this journey. Thank you for your immense patience and support.

A special and most profound debt of gratitude is owed to my elder brother, Narayan, for being my guardian and advocate for my studies. By selflessly taking on responsibilities and making personal sacrifices, he lightened the burden on my shoulders and gave me the freedom to succeed.

Finally, a very special thanks to my father and mother for their unconditional love and support. To all my brothers and sisters, thank you for being by my side and for always believing in me.

Dedicated to my parents...

Chapter 1

Introduction

Liquid crystal elastomers (LCEs) are advanced stimuli-responsive materials that combine the self-organisation of liquid crystals (LCs) with the elasticity of polymer networks [1, 2, 3]. Structurally, they are formed from cross-linked polymeric chains with embedded LC molecules [1] also called mesogens. Owing to the strong coupling between mechanical deformation and mesogenic ordering, LCEs have attracted considerable attention for applications in bioinspired actuators, artificial muscles, and other modern engineering systems [4, 5, 6, 7, 8, 9, 10, 11].

Their special architecture enables LCEs to exhibit both orientational order characteristic of LC fluids and large reversible deformations typical of elastomer solids. As a result, these materials can undergo significant shape changes when the LC orientation varies in response to external stimuli such as temperature changes [12, 13], illumination [14, 15, 16], and electric or magnetic [8, 17, 18, 19] fields. Conversely, the LC alignment itself may evolve under applied mechanical loads, and this is the focus of theoretical and computational investigation in this thesis.

In modern laboratories, LCEs are synthesised through a range of fabrication techniques. Most commonly, the resulting samples are initially polydomain, meaning that the material contains multiple regions with different nematic alignments. The unit vector describing the local direction of uniaxial nematic alignment is known as the *director*. Through the application of electric or magnetic fields, or by mechanically deforming the material, these polydomain structures can be transformed into monodomain configurations in which the director field is aligned in a preferred direction [20, 21, 22, 23, 24]. A defining feature of nematic elastomers is the coupling between deformation and director rotation. Under mechanical loading, the director typically rotates in order to align with the direction of largest principal stretch [3, 25]. This reorientation process is not always spatially uniform and may give rise to striking macroscopic instabilities.

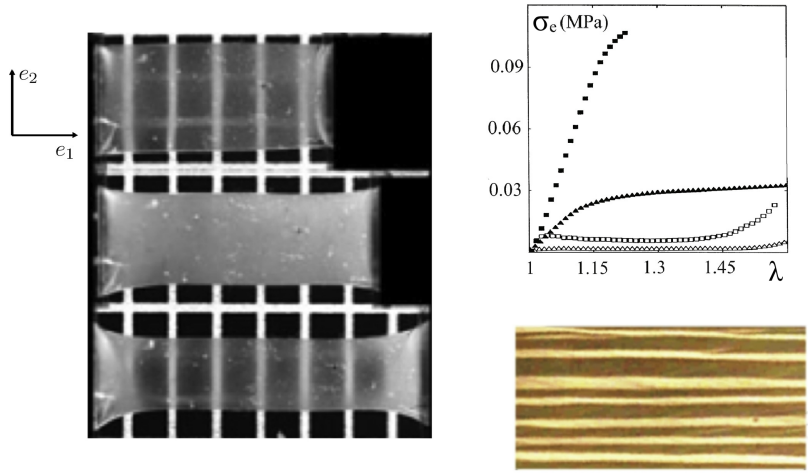


FIGURE 1.1: Experimental observation on shear striping instabilities in LCE sample stretched perpendicular to director. Left: Sample appearing opaque during rotation phase and translucent when uniformly aligned. Top right: Nominal stress plotted against uniaxial extension of different samples. Bottom right: Stripes domains in response to the perpendicular stretch [26].

One characteristic deformation pattern observed in stretched nematic elastomers is the formation of parallel stripe domains (see figure 1.1) in which neighbouring stripes undergo equal and opposite shear deformations [26, 27]. This phenomenon is typically interpreted through the concept of *soft* or *semi-soft elasticity*, where the material minimises its energy by forming a microstructure composed of many homogeneously deformed regions whose collective macroscopic deformation remains compatible [28]. The resulting stress–strain response exhibits a plateau or much slower stress increase compared with the surrounding deformation regimes. Shear-stripe formation in elongated nematic LCEs has been widely documented experimentally [26, 29, 30, 31, 32, 33, 34, 35] and studied extensively through theoretical analysis [3, 18, 26, 28, 36, 37, 38, 39, 40, 41, 42, 43, 44, 45] and numerical simulations [46, 47]. As a result, the formation of such stripe microstructures is relatively well understood.

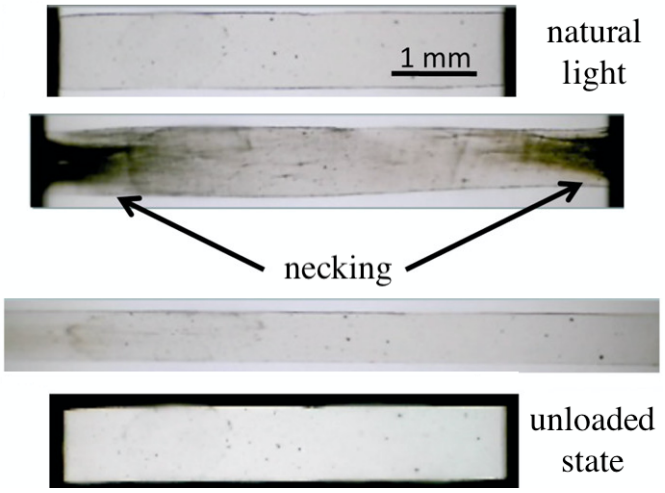


FIGURE 1.2: Experimental observation of necking in an LCE sample under tensile loading [30].

Another notable example is localised necking (see figure 1.2) observed in certain LCEs subjected to sufficiently large tensile forces [20]. In such cases,

there exists a critical extension ratio beyond which the force required to extend the material decreases rather than increases. Once this critical point is reached, the homogeneous deformation becomes unstable and the sample elongates preferentially within a narrow region, producing a pronounced reduction in the local cross-section. Experimental evidence of necking in LCEs has been reported in [30, 48, 49]. Since this behaviour cannot be captured by the neoclassical LCE model [36, 37] based on the neo-Hookean strain-energy function [50], a satisfactory mathematical description of LCE necking is still needed.

In addition to these elastic phenomena, experiments indicate that nematic LCEs exhibit strain-rate-dependent hysteresis during loading and unloading (see figure 1.3) [51, 52, 53, 54, 55]. Although the overall shape of the nonlinear stress–strain curve is often largely independent of strain rate, the presence of hysteresis suggests the existence of dissipative mechanisms within the material. For fixed strain rates, the macroscopic deformation behaviour can often be described using nonlinear hyperelastic models [36, 37, 39, 40, 41, 42, 43, 56, 57].

While the viscoelastic behaviour of polymers has been extensively studied (see, e.g., recent review articles [58, 59] and the references therein), a comprehensive viscoelastic description of LCEs must incorporate dissipation arising both from the viscous deformation of the polymer network and from the rotation and ordering dynamics of the mesogens. Developing constitutive models that fully capture this coupling remains a significant challenge. Experimental studies have revealed dissipative effects associated with the time evolution of mesogen order and director reorientation [60, 61, 62]. Recent modelling efforts therefore treat nematic LCEs as finite-deformation viscoelastic networks coupled with viscous director dynamics. For example, in

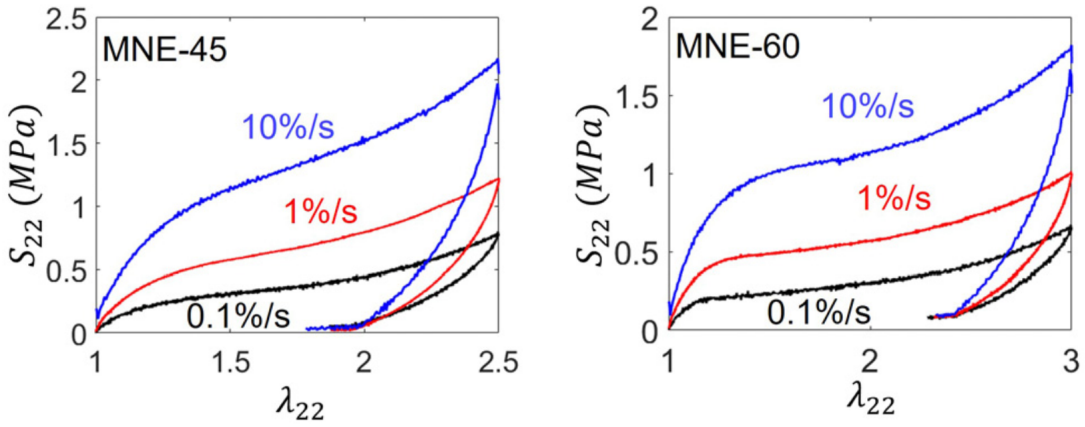


FIGURE 1.3: Experimental observation of strain-rate-dependent hysteresis: Loading and unloading nominal stress (S_{22}) as a function of applied stretch (λ_{22}) for monodomain nematic elastomer (MNE) with initial director angle 45° (MNE-45) and 60° (MNE-60) under uniaxial tension at different strain rates [55].

[63, 64], the director is assumed to evolve viscously and may not return to its original orientation after unloading. Other approaches incorporate additional dissipative mechanisms, such as viscous mesogen ordering, viscous director rotation, and viscoelastic deformation of the polymer network [65, 66], while some models focus primarily on viscosity within the polymeric network itself [67]. Despite these advances, a complete constitutive framework capable of capturing the coupled viscoelastic and orientational dynamics of LCEs has yet to be established.

The aim of this thesis is to answer these important open questions on the complex theoretical description and computer simulation of nematic LCEs. For the numerical examples, the finite element method [47, 68] is employed and implemented by augmenting existing C++ procedures within the open-source software FEBio [69].

The thesis is organised as follows:

- Chapter 2 offers the technical background for the study of LCEs and introduces notation.
- In Chapter 3, nematic-hyperelastic models that capture LCE necking and shear striping are devised.
- Chapter 4 focuses on viscoelastic modelling of LCEs.
- Chapter 5 is dedicated to the purpose-built finite element method for the numerical simulation of elastic and viscoelastic effects in LCEs.
- Numerical examples are presented and discussed in Chapter 6. These are based on and compared to experimental evidence from the literature.
- Chapter 7 includes concluding remarks and ideas for future developments building on this work.

Key research findings presented in this thesis have been published in [57] and [70]. Numerical data for this research are openly available at following GitHub repositories:

- https://github.com/PoudelRabin/FELCE_Deformation_Localisation.
- https://github.com/PoudelRabin/FELCE_Viscoelastic_Behaviour.

Chapter 2

Theory of liquid crystal elastomers

Liquid crystal elastomers (LCEs) are a unique class of materials that are formed by chemically incorporating liquid crystal (LC) molecules into a cross-linked polymer matrix of elastomers. This combination results in materials that exhibit both the elastic properties of elastomers and directional properties of LCs. The coupling between the polymer network and the LC mesogens gives rise to many interesting mechanical properties that are not observed in either fluid LCs or elastomers alone (see figure 2.1).

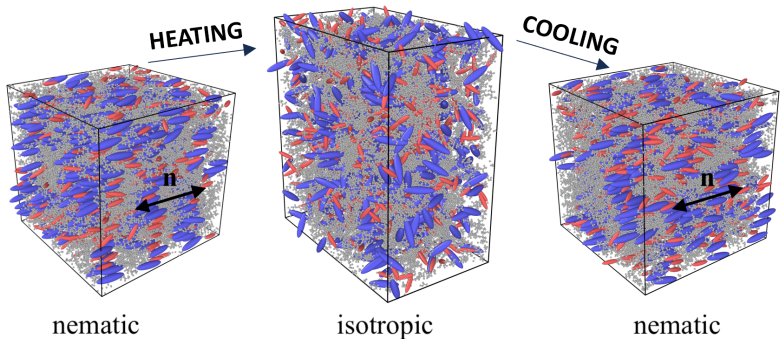


FIGURE 2.1: All-atom molecular dynamics simulation of a thermotropic LCE: The material extends along the director as the LCs align in the nematic phase at low temperature and contracts in the isotropic phase at high temperatures. The director vector $\boldsymbol{n}$ indicates the direction of mesogens alignment [71].

2.1 Theory of liquid crystals

LCs represent a distinct state of matter presenting properties of both liquids and crystalline solids. They were first observed in the late 19th century by Friedrich Reinitzer [72], who noticed that the matter exhibits two distinct melting point, one transitioning form solid to a cloudy fluid and then to a clear liquid. The cloudy phase, later termed the liquid crystal phase, flowed like a liquid but had some degree of order like a crystal. LCs are typically composed of anisotropic rod-like molecules.

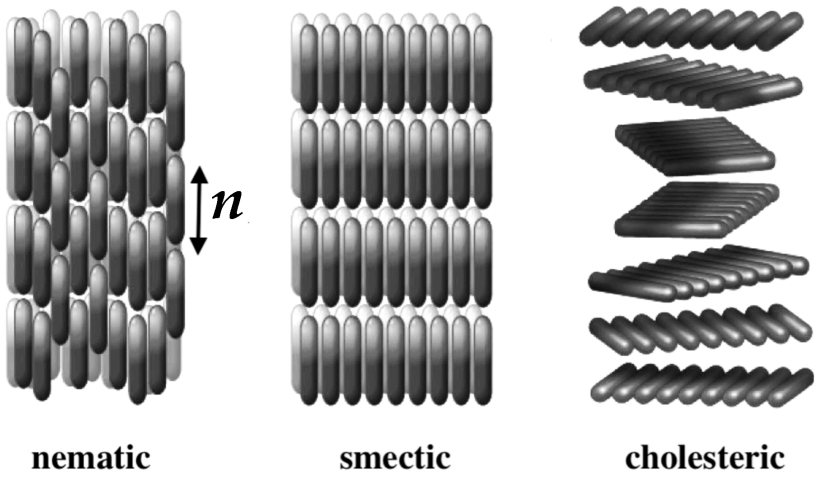


FIGURE 2.2: Liquid crystal phases.

LC phases can be classified into three main categories: nematic, smectic, and cholesteric, as shown in the figure 2.2. The nematic phase is the one in which molecules are oriented in the same direction, but do not have a positional order. The smectic phase has orientation similar to nematics but has also a layered structure. The cholesteric phase displays a helical arrangement of molecular orientation.

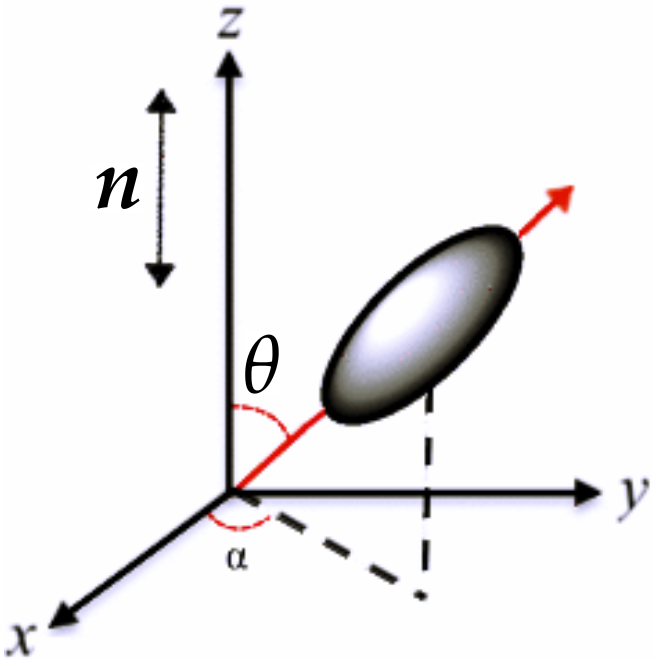


FIGURE 2.3: Schematic of the angle θ between the director $\boldsymbol{n}$ and the molecular axis used in derivation of uniaxial order parameter Q [3].

The mathematical description of nematic LCs involves the concept of a director field, which represents the average orientation of the molecules. This director field is denoted by a unit vector $\boldsymbol{n}$ which describes the local orientation of the LC molecules. One of the physical properties of LCs is their head to tail symmetry which makes the director field $\boldsymbol{n}$ and $-\boldsymbol{n}$ indistinguishable. While the director vector $\boldsymbol{n}$ gives the direction of alignment, it does not provide information about the degree of order. The order degree is quantified by the scalar order parameter Q. If θ is the angle between the director $\boldsymbol{n}$ and the molecular axis (see figure 2.3), then the order parameter Q can be defined as:

$$Q = \frac{1}{2}\langle 3\cos^2\theta - 1\rangle, \tag{2.1}$$

where the angle brackets $\langle\cdot\rangle$ denote an average over orientational distributions of all molecules. The limits of Q are 0 for completely disordered isotropic

phase and 1 for perfectly ordered nematic phase. In practice, the intermediate values, typically in order of 0.3 to 0.8, are for the real partially ordered nematic phases [73].

While the Q scalar parameter is sufficient to capture the degree of order in uniformly aligned uniaxial nematics, it falls short of describing the more complex alignment like the biaxial nematic phase. In general, the tensorial order parameter $\boldsymbol{Q}$ is required. This is a second order symmetric traceless tensor defined as

$$\boldsymbol{Q} = Q\left(\boldsymbol{n} \otimes \boldsymbol{n} - \frac{1}{3}\boldsymbol{I}\right), \tag{2.2}$$

where $\boldsymbol{I}$ is the identity tensor [74].

2.2 Continuum theory of LCEs

2.2.1 Kinematics

Consider a continuum body of LCE material occupying a region $\Omega_0 \subset \mathbb{R}^3$ in a reference state at time $t = 0$. A material point in the reference state is represented by position vector $\boldsymbol{X} \in \Omega_0$. In the deformed state at time t, the body occupies a different region $\Omega \subset \mathbb{R}^3$. In this current configuration, the material point has the new position vector $\boldsymbol{x} \in \Omega$.

In the material description (i.e., in terms of variables in the reference configuration), the motion of the particle from the reference to the current configuration is equal to

$$\boldsymbol{x} = \boldsymbol{x}(\boldsymbol{X}, t), \tag{2.3}$$

and in the spatial description (i.e., in terms of variables in the current configuration) is

$$\boldsymbol{X} = \boldsymbol{X}(\boldsymbol{x}, t). \tag{2.4}$$

Throughout this work, material description is employed. Kinematic relations, balance equations and other derived quantities are described with respect to the material particle in the reference configuration.

The displacement field $\boldsymbol{u}$ is defined by

$$\boldsymbol{u}(\boldsymbol{X}, t) = \boldsymbol{x}(\boldsymbol{X}, t) - \boldsymbol{X}. \tag{2.5}$$

In LCEs, deformation of the body is not sufficient to describe the kinematics. There is also a change in the director from the reference state $\boldsymbol{n}_0$ to the current state $\boldsymbol{n}$ caused by mesogen rotation.

The deformation gradient $\boldsymbol{F}$ is the primary measure of deformation which maps the line element $d\boldsymbol{X}$ in the reference state into the $d\boldsymbol{x}$ in the current state. It is defined as

$$\boldsymbol{F} = \frac{\partial \boldsymbol{x}(\boldsymbol{X}, t)}{\partial \boldsymbol{X}} = \operatorname{Grad} \boldsymbol{x}. \tag{2.6}$$

The determinant of the deformation gradient $J = \det \boldsymbol{F} > 0$, called the Jacobian, measures the change of volume of a material element as

$$dv = JdV, \tag{2.7}$$

where dV and dv are the volume elements in the reference and current configurations, respectively. For incompressible materials $J = 1$.

Similarly, the change of area of a surface element is given by

$$d\boldsymbol{a} = J\boldsymbol{F}^{-T}d\boldsymbol{A}, \tag{2.8}$$

with $d\boldsymbol{A}$ and $d\boldsymbol{a}$ the vector elements of surface area defined in the reference and current configurations, respectively.

Strain measure. The deformation gradient $\boldsymbol{F}$ is invariant with respect to rigid body translations but not with respect to rigid body rotations. Due to this fact, it cannot be used as a strain measure. One can retain the pure deformation while eliminating the rotational component by removing the rotational tensor through polar decomposition of $\boldsymbol{F}$. By the polar decomposition theorem, there exist three tensors $\boldsymbol{U}$, $\boldsymbol{V}$ and $\boldsymbol{R}$ [75], such that

$$\boldsymbol{F} = \boldsymbol{R}\boldsymbol{U} = \boldsymbol{V}\boldsymbol{R}, \tag{2.9}$$

where $\boldsymbol{R}$ is a proper orthogonal rotation tensor, $\boldsymbol{U}$ is the right stretch tensor operating before rotation and $\boldsymbol{V}$ is the left stretch tensor operating after rotation. The right and the left Cauchy-Green deformation tensors $\boldsymbol{C}$ and $\boldsymbol{B}$, respectively, are defined as

$$\boldsymbol{C} = \boldsymbol{U}^2 = \boldsymbol{F}^T\boldsymbol{F}, \tag{2.10}$$

$$\boldsymbol{B} = \boldsymbol{V}^2 = \boldsymbol{F}\boldsymbol{F}^T. \tag{2.11}$$

Subsequently, a strain tensor called Green-Lagrange based on $\boldsymbol{C}$ is defined as

$$\boldsymbol{E} = \frac{1}{2}(\boldsymbol{C} - \boldsymbol{I}). \tag{2.12}$$

For any deformation, there are always three mutually perpendicular direction along which material undergoes a pure stretch without shear. These directions are called the principle directions $\boldsymbol{m}_i\,(i = 1,2,3)$ and the associate stretch ratios are called the principle stretches $\lambda_i\,(i = 1,2,3)$. These are the eigen directions and eigenvalues, respectively, of the tensor $\boldsymbol{U}$. The tensor $\boldsymbol{V}$ shares the same eigenvalues λ_i but the eigen directions are $\hat{\boldsymbol{m}}_i = \boldsymbol{R}\boldsymbol{m}_i$. The tensor $\boldsymbol{C}$ shares the eigen directions with $\boldsymbol{U}$ and the tensor $\boldsymbol{B}$ shares the eigen directions with $\boldsymbol{V}$. The eigenvalues of $\boldsymbol{C}$ (and $\boldsymbol{B}$) are the square of the principle stretches. Therefore, one can represent $\boldsymbol{C}$ as

$$\boldsymbol{C} = \sum_{i=1}^{3} \lambda_i^2 \boldsymbol{m}_i \otimes \boldsymbol{m}_i. \tag{2.13}$$

The principle invariants of $\boldsymbol{C}$ (and $\boldsymbol{B}$) take the form

$$I_1 = \operatorname{tr} \boldsymbol{C} = \lambda_1^2 + \lambda_2^2 + \lambda_3^2, \tag{2.14}$$

$$I_2 = \frac{1}{2}[(\operatorname{tr} \boldsymbol{C})^2 - \operatorname{tr}(\boldsymbol{C}^2)] = \lambda_1^2\lambda_2^2 + \lambda_1^2\lambda_3^2 + \lambda_2^2\lambda_3^2, \tag{2.15}$$

$$I_3 = \det \boldsymbol{C} = \lambda_1^2\lambda_2^2\lambda_3^2 = J^2. \tag{2.16}$$

Stress tensors. Consider a body acted upon by the external forces cut by a plane surface passing through a point $\boldsymbol{x} \in \Omega$, with normal vector $\boldsymbol{N}$. The infinitesimal resultant force acting on the plane is $d\boldsymbol{f}$. For every surface element, we have

$$d\boldsymbol{f} = \boldsymbol{t}da = \hat{\boldsymbol{t}}dA, \tag{2.17}$$

where $\boldsymbol{t}$ is the Cauchy traction vector defined in the current configuration and $\hat{\boldsymbol{t}}$ is the nominal traction vector defined in the reference configuration, acting on da and dA with outward normal $\boldsymbol{N}$ and $\boldsymbol{N}_0$, respectively (see figure 2.4).

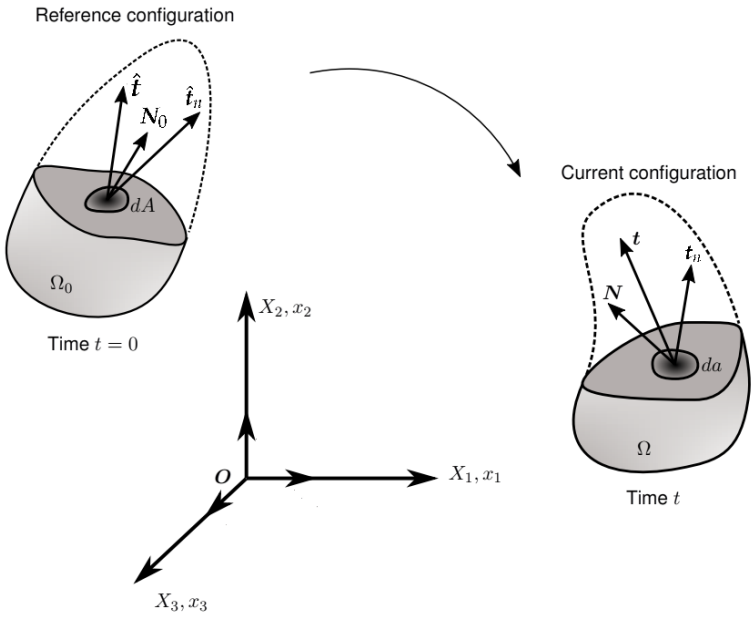


FIGURE 2.4: Cauchy traction and nominal traction vectors $\boldsymbol{t}$ and $\hat{\boldsymbol{t}}$ acting on an infinitesimal surface element da and dA with outward normal $\boldsymbol{N}$ and $\boldsymbol{N}_0$ in the current and reference configurations, respectively. Vectors $\boldsymbol{t}_n$ and $\hat{\boldsymbol{t}}_n$ denotes the generalised traction for the director field in the current and reference configurations, respectively.

Cauchy's theorem states that there exists a unique second order tensor field such that the surface traction depends linearly on outward normal [76, 77], such that

$$\boldsymbol{t} = \boldsymbol{\sigma}\boldsymbol{N}, \tag{2.18}$$

$$\hat{\boldsymbol{t}} = \boldsymbol{P}\boldsymbol{N}_0, \tag{2.19}$$

where $\boldsymbol{\sigma}$ is the Cauchy stress tensor (representing the internal force acting within the deformed solid on a unit of deformed area) and $\boldsymbol{P}$ is the first Piola-Kirchhoff stress tensor (representing the internal force acting within the deformed solid on an area element which, in the reference state, was one unit of area).

By analogy to the definition of the Cauchy stress tensor, we can define the generalised director stress tensor $\boldsymbol{\pi}$ and $\boldsymbol{\pi}_0$ in the current and reference configuration, respectively, such that

$$\boldsymbol{t}_n = \boldsymbol{\pi}\boldsymbol{N}, \tag{2.20}$$

$$\hat{\boldsymbol{t}}_n = \boldsymbol{\pi}_0\boldsymbol{N}_0, \tag{2.21}$$

where $\boldsymbol{t}_n$ and $\hat{\boldsymbol{t}}_n$ are the generalised traction force density for the director field in the current and reference configuration, respectively. Similarly to the standard traction force $\boldsymbol{t}$, the generalised traction force for director field $\boldsymbol{t}_n$ is the couple traction vector (torque per unit area) acting on the director field $\boldsymbol{n}$ in the current configuration. In LCE, applying a surface couple traction causes the nematic director at the boundary to rotate away from its preferred orientation.

2.2.2 Balance of linear momentum

Balance law of linear momentum is the foundation for describing of the mechanical behavior of LCEs. It states that the rate of change of linear momentum of a body is equal to the sum of the external forces acting on the body. The external forces can be categorized into body forces, which act throughout the volume of the body, and surface forces, which act on the boundary of the body.

When the body in the current configuration is acted upon by a traction force density $\hat{\boldsymbol{t}}$ and a body force density $\hat{\boldsymbol{b}}$, the balance of linear momentum takes the form

$$\frac{d}{dt}\int_{\Omega} \rho\boldsymbol{v}\, dv = \int_{\Omega} \hat{\boldsymbol{b}}\, dv + \int_{\partial\Omega} \hat{\boldsymbol{t}}\, da, \tag{2.22}$$

where ρ is the body density and v represents the velocity of the material. Similarly, for the director field $\boldsymbol{n}$ acted upon by the generalised external body force density $\hat{\boldsymbol{b}}_n$, internal body force density $\hat{\boldsymbol{g}}_n$ and traction force density $\hat{\boldsymbol{t}}_n$, the director momentum balance is

$$\frac{d}{dt}\int_{\Omega} \rho_i \dot{\boldsymbol{n}}\, dv = \int_{\Omega} \hat{\boldsymbol{b}}_n\, dv + \int_{\Omega} \hat{\boldsymbol{g}}_n\, dv + \int_{\partial\Omega} \hat{\boldsymbol{t}}_n\, da, \tag{2.23}$$

where ρ_i is the generalised inertial density for the director and the dot ($\dot{\bullet}$) above a variable represents differentiation with respect to time using Newton notation. Internal body force density $\hat{\boldsymbol{g}}_n$ is the volume-distributed force generated by the material's own response when its microstructure is disturbed.

Cauchy's theorem [76, 77] states the existence of a second order tensor $\boldsymbol{\sigma}$ (Cauchy's stress) and $\boldsymbol{\pi}$ (generalised director stress) in the current configuration, such that

$$\hat{\boldsymbol{t}} = \boldsymbol{\sigma}\boldsymbol{N} \quad \text{and} \quad \hat{\boldsymbol{t}}_n = \boldsymbol{\pi}\boldsymbol{N}. \tag{2.24}$$

By the divergence theorem, after inserting Cauchy's theorem (2.18) in (2.22) and (2.20) in (2.23), we obtain, respectively,

$$\int_{\Omega} (\mathrm{Div}\, \boldsymbol{\sigma} + \hat{\boldsymbol{b}} - \rho\dot{\boldsymbol{v}})\, dv = 0, \tag{2.25}$$

$$\int_{\Omega} (\mathrm{Div}\, \boldsymbol{\pi} + \hat{\boldsymbol{b}}_n + \hat{\boldsymbol{g}}_n - \rho_i \ddot{\boldsymbol{n}})\, dv = 0. \tag{2.26}$$

Since the above equations are valid for every material point at any time, we have their local forms in terms of variables $(\boldsymbol{X}, t)$ in the current configurations

as

$$\operatorname{Div}\boldsymbol{\sigma} + \hat{\boldsymbol{b}} - \rho\dot{\boldsymbol{v}} = 0, \tag{2.27}$$

$$\operatorname{Div}\boldsymbol{\pi} + \hat{\boldsymbol{b}}_n + \hat{\boldsymbol{g}}_n - \rho_i\ddot{\boldsymbol{n}} = 0. \tag{2.28}$$

Equivalently, in the reference configuration, we have

$$\operatorname{Div}\boldsymbol{P} + \boldsymbol{b} - \rho_0\dot{\boldsymbol{v}} = 0, \tag{2.29}$$

$$\operatorname{Div}\boldsymbol{\pi}_0 + \boldsymbol{b}_n + \boldsymbol{g}_n - \rho_{i0}\ddot{\boldsymbol{n}} = 0. \tag{2.30}$$

where $\boldsymbol{b}$, $\boldsymbol{b}_n$, $\boldsymbol{g}_n$ (without the hat) correspond to the relevant quantities in the reference configuration.

2.2.3 Thermodynamics consideration

Conservation of energy. The first law of thermodynamics imposes the conservation of energy in the system. Assuming that the thermal power can be neglected, the external power input due to the applied system of forces ($\boldsymbol{b}$, $\boldsymbol{t}$, $\boldsymbol{b}_n$, $\boldsymbol{t}_n$) is equal to

$$\mathcal{P}_{ext} = \int_{\Omega_0} (\boldsymbol{b}\cdot\boldsymbol{v} + \boldsymbol{b}_n\cdot\dot{\boldsymbol{n}})\, dV + \int_{\partial\Omega_0} (\boldsymbol{t}\cdot\boldsymbol{v} + \boldsymbol{t}_n\cdot\dot{\boldsymbol{n}})\, dA. \tag{2.31}$$

The kinetic energy $\mathcal{K}$ and internal energy $\mathcal{E}$ of the continuum LCE body in the reference configuration takes the form, respectively,

$$\mathcal{K} = \frac{1}{2}\int_{\Omega_0} \rho_0\boldsymbol{v}\cdot\boldsymbol{v}\, dV + \frac{1}{2}\int_{\Omega_0} \rho_{i0}\dot{\boldsymbol{n}}\cdot\dot{\boldsymbol{n}}\, dV, \tag{2.32}$$

$$\mathcal{E} = \int_{\Omega_0} U\, dV, \tag{2.33}$$

where U is the specific internal energy per unit reference volume. The sum of kinetic and internal energies characterises the total energy of the system. The first law of thermodynamics states that the rate of change of total energy of a system equals the external power and the rate of heat input to the system. Neglecting the heat input, we have

$$\dot{\mathcal{K}} + \dot{\mathcal{E}} = \mathcal{P}_{ext}. \tag{2.34}$$

From equations (2.18) and (2.20) by the divergence theorem, we obtain

$$\int_{\partial\Omega_0} \boldsymbol{t} \cdot \boldsymbol{v} = \int_{\partial\Omega_0} (\boldsymbol{P}\boldsymbol{N}_0) \cdot \boldsymbol{v}\, dA = \int_{\Omega_0} \mathrm{Div}(\boldsymbol{P}^T\boldsymbol{v})\, dV, \tag{2.35}$$

$$\int_{\partial\Omega_0} \boldsymbol{t}_n \cdot \dot{\boldsymbol{n}} = \int_{\partial\Omega_0} (\boldsymbol{\pi}_0\boldsymbol{N}_0) \cdot \dot{\boldsymbol{n}}\, dA = \int_{\Omega_0} \mathrm{Div}(\boldsymbol{\pi}_0^T\dot{\boldsymbol{n}})\, dV. \tag{2.36}$$

Expanding the integrant on the right-hand side of equations (2.35) and (2.36) gives

$$\mathrm{Div}(\boldsymbol{P}^T\boldsymbol{v}) = \boldsymbol{P} : \mathrm{Grad}\ \boldsymbol{v} + \boldsymbol{v} \cdot \mathrm{Div}\, \boldsymbol{P} = \boldsymbol{P} : \dot{\boldsymbol{F}} + \boldsymbol{v} \cdot \mathrm{Div}\, \boldsymbol{P}, \tag{2.37}$$

$$\mathrm{Div}(\boldsymbol{\pi}_0^T\dot{\boldsymbol{n}}) = \boldsymbol{\pi}_0 : \mathrm{Grad}\ \dot{\boldsymbol{n}} + \dot{\boldsymbol{n}} \cdot \mathrm{Div}\, \boldsymbol{\pi}_0 = \boldsymbol{\pi}_0 : \dot{\overline{\mathrm{Grad}\ \boldsymbol{n}}} + \dot{\boldsymbol{n}} \cdot \mathrm{Div}\, \boldsymbol{\pi}_0. \tag{2.38}$$

Next, inserting the above forms into equation (2.31) and rearranging yields

$$\begin{aligned}\mathcal{P}_{ext} = &\int_{\Omega_0} (\boldsymbol{v} \cdot \mathrm{Div}\, \boldsymbol{P} + \boldsymbol{b} \cdot \boldsymbol{v})\, dV + \int_{\Omega_0} (\dot{\boldsymbol{n}} \cdot \mathrm{Div}\, \boldsymbol{\pi}_0 + \boldsymbol{b}_n \cdot \dot{\boldsymbol{n}})\, dV \\ &+ \int_{\Omega_0} (\boldsymbol{P} : \dot{\boldsymbol{F}} + \boldsymbol{\pi}_0 : \dot{\overline{\mathrm{Grad}\ \boldsymbol{n}}})\, dV.\end{aligned} \tag{2.39}$$

Then, by equations (2.32), (2.33), (2.34), and (2.39), we have

$$\int_{\Omega_0} \rho_0 \dot{\boldsymbol{v}} \cdot \boldsymbol{v}\, dV + \int_{\Omega_0} \rho_{i0} \dot{\boldsymbol{n}} \cdot \dot{\boldsymbol{n}}\, dV + \int_{\Omega_0} \dot{U}\, dV = \int_{\Omega_0} (\boldsymbol{v} \cdot \operatorname{Div} \boldsymbol{P} + \boldsymbol{b} \cdot \boldsymbol{v})\, dV + \int_{\Omega_0} (\dot{\boldsymbol{n}} \cdot \operatorname{Div} \boldsymbol{\pi}_0 + \boldsymbol{b}_n \cdot \dot{\boldsymbol{n}})\, dV + \int_{\Omega_0} (\boldsymbol{P} : \dot{\boldsymbol{F}} + \boldsymbol{\pi}_0 : \dot{\overline{\operatorname{Grad}\ \boldsymbol{n}}})\, dV. \quad (2.40)$$

Equivalently,

$$\int_{\Omega_0} \dot{U}\, dV = \int_{\Omega_0} (\operatorname{Div} \boldsymbol{P} + \boldsymbol{b} - \rho_0 \dot{\boldsymbol{v}}) \cdot \dot{\boldsymbol{v}}\, dV + \int_{\Omega_0} (\operatorname{Div} \boldsymbol{\pi}_0 + \boldsymbol{b}_n - \rho_{i0} \dot{\boldsymbol{n}}) \cdot \dot{\boldsymbol{n}}\, dV + \int_{\Omega_0} (\boldsymbol{P} : \dot{\boldsymbol{F}} + \boldsymbol{\pi}_0 : \dot{\overline{\operatorname{Grad}\ \boldsymbol{n}}})\, dV, \quad (2.41)$$

which, by the balance of momentum (2.30)-(2.29), simplifies to

$$\int_{\Omega_0} \dot{U}\, dV = \int_{\Omega_0} (\boldsymbol{P} : \dot{\boldsymbol{F}} + \boldsymbol{\pi}_0 : \dot{\overline{\operatorname{Grad}\ \boldsymbol{n}}} - \mathbf{g}_n \cdot \dot{\boldsymbol{n}})\, dV. \quad (2.42)$$

Since this must hold for every subset of the system, the energy balance in the reference configuration takes the local form

$$\dot{U} = \boldsymbol{P} : \dot{\boldsymbol{F}} + \boldsymbol{\pi}_0 : \dot{\overline{\operatorname{Grad}\ \boldsymbol{n}}} - \mathbf{g}_n \cdot \dot{\boldsymbol{n}}. \quad (2.43)$$

Entropy inequality. Entropy inequality expresses the second law of thermodynamics which states that the rate of change of entropy of a system is greater than or equal to the rate of heat input divided by the temperature. While the first law of thermodynamics describes the phenomenon of conservation of energy in terms of heat and other forms, the second law describes the direction of flow of the heat and the irreversibility of the processes [75].

We define the entropy s contained in the system as

$$s = \int_{\Omega_0} \eta \, dV, \tag{2.44}$$

where η is the specific entropy density per unit reference volume. In this thesis, we model the mechanical behavior of the LCE independently of thermal effects. By assuming an adiabatic process with no external heat exchange, we simplify the total entropy production expression to be the rate of change of entropy $\dot{s}$. Assuming the absolute temperature of the system is T, the rate of internal dissipation is given by $\mathcal{D}_{int} = T\dot{s}$. The second law of thermodynamics requires that the rate of internal dissipation is nonnegative. Hence, we have the Clausius-Duhem inequality [77, 78],

$$\mathcal{D}_{int} = T\dot{s} = \int_{\Omega_0} T\dot{\eta} \, dV \geq 0. \tag{2.45}$$

In local form in terms of variables $(\boldsymbol{X}, t)$, equation (2.45) leads to

$$\mathcal{D}_{int} = T\dot{\eta} \ \geq 0. \tag{2.46}$$

To exploit the requirement of entropy production, we express the free energy density $\mathcal{W}$ in terms of internal energy U and the entropy η as

$$\mathcal{W} = U - T\eta. \tag{2.47}$$

For the isothermal process, time rate for free energy given by equation (2.47) is

$$\dot{\mathcal{W}} = \dot{U} - T\dot{\eta}. \tag{2.48}$$

From (2.43), (2.46), (2.48), we obtain

$$\mathcal{D}_{int} = -\dot{\mathcal{W}} + \boldsymbol{P} : \dot{\boldsymbol{F}} + \boldsymbol{\pi}_0 : \overline{\text{Grad } \boldsymbol{n}}^{\cdot} - \boldsymbol{g}_n \cdot \dot{\boldsymbol{n}} \geq 0. \tag{2.49}$$

The time differentiation of free energy density function $\mathcal{W}(\boldsymbol{F}, \boldsymbol{n}, \text{Grad } \boldsymbol{n})$ is

$$\dot{\mathcal{W}} = \frac{\partial \mathcal{W}}{\partial \boldsymbol{F}} : \dot{\boldsymbol{F}} + \frac{\partial \mathcal{W}}{\partial \boldsymbol{n}} : \dot{\boldsymbol{n}} + \frac{\partial \mathcal{W}}{\partial \, \text{Grad } \boldsymbol{n}} : \overline{\text{Grad } \boldsymbol{n}}^{\cdot}. \tag{2.50}$$

Then (2.49) becomes

$$\left(-\frac{\partial \mathcal{W}}{\partial \boldsymbol{F}} + \boldsymbol{P}\right) : \dot{\boldsymbol{F}} + \left(-\frac{\partial \mathcal{W}}{\partial \boldsymbol{n}} - \boldsymbol{g}_n\right) : \dot{\boldsymbol{n}} + \left(-\frac{\partial \mathcal{W}}{\partial \, \text{Grad } \boldsymbol{n}} + \boldsymbol{\pi}_0\right) : \overline{\text{Grad } \boldsymbol{n}}^{\cdot} \geq 0. \tag{2.51}$$

Following the arguments of Coleman and Noll [78], inequality (2.51) must hold for arbitrary values of $\dot{\boldsymbol{F}}$, $\dot{\boldsymbol{n}}$ and $\overline{\text{Grad } \boldsymbol{n}}^{\cdot}$. This results in their coefficients vanishing, so we have the following constitutive relations

$$\boldsymbol{P} = \frac{\partial \mathcal{W}}{\partial \boldsymbol{F}}, \qquad \boldsymbol{g}_n = -\frac{\partial \mathcal{W}}{\partial \boldsymbol{n}}, \qquad \boldsymbol{\pi}_0 = \frac{\partial \mathcal{W}}{\partial \, \text{Grad } \boldsymbol{n}}. \tag{2.52}$$

Then inequality (2.51) simplifies as

$$\mathcal{D}_{int} \geq 0. \tag{2.53}$$

The internal dissipation is zero for the purely elastic response of the LCE material and is positive for the irreversible response.

2.2.4 Constitutive functions for uniaxial LCEs

The macroscopic elastic behaviour of a nematic LCE is typically described by a strain-energy density function [57] given as

$$\mathcal{W}(\boldsymbol{F}, \boldsymbol{n}, \text{Grad } \boldsymbol{n}) = \mathcal{W}^{(1)}(\boldsymbol{F}) + \mathcal{W}^{(2)}(\boldsymbol{A}) + \mathcal{W}^{(3)}(\text{Grad}\, \boldsymbol{n}). \tag{2.54}$$

The first term $\mathcal{W}^{(1)}$ is the energy which characterises the soft-elastic behaviour of an LCE. The second term $\mathcal{W}^{(2)}$ is the isotropic polymer network depending only on the elastic deformation tensor. The third term $\mathcal{W}^{(3)}$ is the Frank free energy which characterises the distortion of the director field [57].

In the above equation, $\boldsymbol{A}$ is the local elastic deformation tensor which satisfies the following multiplicative decomposition (see figure 2.5) [57]

$$\boldsymbol{F} = \boldsymbol{G}\boldsymbol{A}\boldsymbol{G}_0^{-1}, \tag{2.55}$$

with $\boldsymbol{G}_0$ and $\boldsymbol{G}$ the natural tensors due to the LC mesogens in the reference and current configuration, respectively. Assuming that the LCE is intrinsically uniaxial, these tensors take the form [57]

$$\boldsymbol{G}_0 = a_0^{-1/6}\boldsymbol{I} + (a_0^{1/3} - a_0^{-1/6})\boldsymbol{n}_0 \otimes \boldsymbol{n}_0, \tag{2.56}$$

$$\boldsymbol{G} = a^{-1/6}\boldsymbol{I} + (a^{1/3} - a^{-1/6})\boldsymbol{n} \otimes \boldsymbol{n}, \tag{2.57}$$

where $\boldsymbol{n}_0$ and $\boldsymbol{n}$ are the local nematic directors, and a_0 and a are the natural shape parameters in the reference and current configuration, respectively. We assume a to be spatially-independent. The ratio $r = a^{1/3}/a^{-1/6} = a^{1/2}$ represents the anisotropy of the natural shape of the LCE mesogens. When $r = 1$, the natural shape is isotropic and the LCE behaves like a conventional

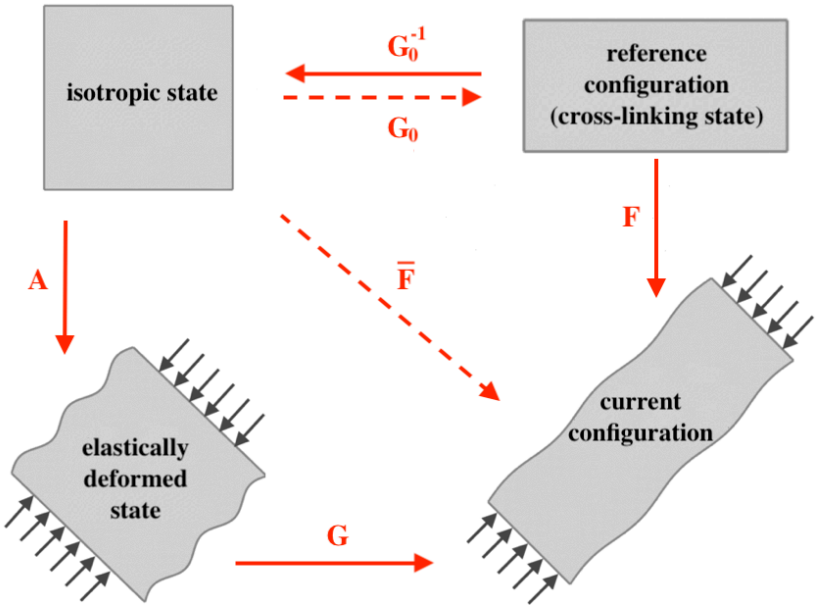


FIGURE 2.5: Schematic representation of multiplicative decomposition of $\boldsymbol{F} = \boldsymbol{G}\boldsymbol{A}\boldsymbol{G}_0^{-1}$.

elastomer. In a nematic phase, when $r > 1$, the natural shape is prolate and when $r < 1$, it is oblate.

The square of the natural deformation tensor, known as the *step-length tensor*, takes the form [1]

$$\boldsymbol{G}^2 = c(\boldsymbol{I} + 2\boldsymbol{Q}), \tag{2.58}$$

where c is the effective step length of the polymeric chain. The tensor $\boldsymbol{G}_0^{-1}$ maps the reference configuration in cross-linking state of LCEs to isotropic state where the mesogens are randomly oriented. The tensor $\boldsymbol{A}$ then maps the isotropic state to the elastically deformed isotropic state. Finally, the tensor $\boldsymbol{G}$ maps the elastically deformed isotropic state to the current configuration of LCEs.

Strain-energy function. One of the popular model for the strain-energy function $\mathcal{W}^{(2)}$ is the neoclassical model [1] which is based on the assumption of the anisotropic Gaussian distribution. It takes the form

$$\mathcal{W}^{(2)}(\boldsymbol{A}) = \frac{1}{2}\mu^{(2)}(\text{tr}(\boldsymbol{A}^T\boldsymbol{A}) - 3), \tag{2.59}$$

where $\mu^{(2)}$ is a constant material parameter. Using equation (2.55) together with (2.59), we can express $\mathcal{W}^{(2)}$ in terms of $\boldsymbol{F}$, $\boldsymbol{G}$ and $\boldsymbol{G}_0$ as

$$\mathcal{W}^{(2)}(\boldsymbol{F}, \boldsymbol{n}, \boldsymbol{n}_0) = \frac{1}{2}\mu^{(2)}(\text{tr}(\boldsymbol{G}^{-1}\boldsymbol{F}\boldsymbol{G}_0^2\boldsymbol{F}^T\boldsymbol{G}^{-T}) - 3). \tag{2.60}$$

The neoclassical model is enough to capture the ideal soft behaviour of the nematic LCEs. However, it has been seen in experiments [40] that the response of the LCEs are semi-soft opposed to soft. To capture this behaviour, an additional [43] neo-Hookean energy function $\mathcal{W}^{(1)}$ is added which is

$$\mathcal{W}^{(1)}(\boldsymbol{F}) = \frac{1}{2}\mu^{(1)}(\text{tr}(\boldsymbol{F}^T\boldsymbol{F}) - 3). \tag{2.61}$$

The Frank free energy $\mathcal{W}^{(3)}$ characterises the spread, twist or bend of the director field. It takes the form [1]

$$\mathcal{W}^{(3)} = \frac{1}{2}K_1(\text{Div } \boldsymbol{n})^2 + \frac{1}{2}K_2(\boldsymbol{n} \cdot \text{Curl } \boldsymbol{n})^2 + \frac{1}{2}K_3(\boldsymbol{n} \times \text{Curl } \boldsymbol{n})^2, \tag{2.62}$$

where K_1, K_2 and K_3 are the splay, twist and bend elastic constants, respectively. In our work, for the mathematical and computational simplicity, we assume *the one-constant approximation* where $K_1 = K_2 = K_3 = K$, which results

in [73]

$$\mathcal{W}^{(3)}(\text{Grad } \boldsymbol{n}) = \frac{1}{2}K|\text{ Grad } \boldsymbol{n}|^2. \tag{2.63}$$

Typical values of Frank constant K is 10^{-11} N [1].

Chapter 3

Key instabilities in LCEs

When a monodomain nematic LCE is stretched perpendicular to the director, the material sample becomes unstable and forms alternating shear stripes. An LCE can also show a localised deformation like necking. In this chapter, we analyse how a material model can predict these instabilities, and study the effects of material parameters on the mechanical behaviour.

3.1 Shear striping instability

One of the unique mechanical behaviours shown by the LCE, unknown in natural rubber, is the shear striping. When an LCE is stretched perpendicular to the director, it exhibits alternating shear domains. During this process, the LCE sample shows a unique stress-strain relationship having three distinct regimes. First, the stress increases sharply with respect to the stretch. When the stretch reaches a certain level, the second regime begins where stress remains almost constant while strain increases. Within this region, the director rotates, and rotation in two adjacent stripes occurs in opposite directions. When the rotations are completed and the director becomes parallel to the stretch direction, the third regime starts where the stress increases nonlinearly with strain [79]. This behaviour is referred to as the *soft (semi-soft) elasticity*.

In experiments, the LCE sample appears to be opaque during the director rotation phase, and translucent when the director is uniformly aligned, before and after rotation (see figure 1.1) [79].

3.1.1 Analysis of shear striping under uniaxial stress

An incompressible nematic LCE can be described by combining the neo-Hookean and neoclassical strain-energy density functions as

$$\mathcal{W}^{(lce)}(\boldsymbol{F},\boldsymbol{n}) = \mathcal{W}(\boldsymbol{F}) + \mathcal{W}^{(nc)}(\boldsymbol{F},\boldsymbol{n}), \tag{3.1}$$

where

$$\mathcal{W}(\boldsymbol{F}) = \frac{\mu^{(1)}}{2}[\mathrm{tr}(\boldsymbol{F}^T\boldsymbol{F}) - 3] \tag{3.2}$$

is a neo-Hookean-type strain-energy function with the constant material parameter $\mu^{(1)} \geq 0$, and

$$\mathcal{W}^{(nc)}(\boldsymbol{F},\boldsymbol{n}) = \frac{\mu^{(2)}}{2}[\mathrm{tr}(\boldsymbol{G}_0\boldsymbol{F}^T\boldsymbol{G}^{-2}\boldsymbol{F}\boldsymbol{G}_0) - 3] \tag{3.3}$$

is the neoclassical form with $\mu^{(2)} \geq 0$ constant.

We analyse shear striping under uniaxial stress. In this case, we assume that the nematic director only rotates in the biaxial plane while the uniaxial order parameter Q remains constant. This assumption about the order parameter is consistent with experimental observations showing relatively small variations before, during and after stripe formation [26].

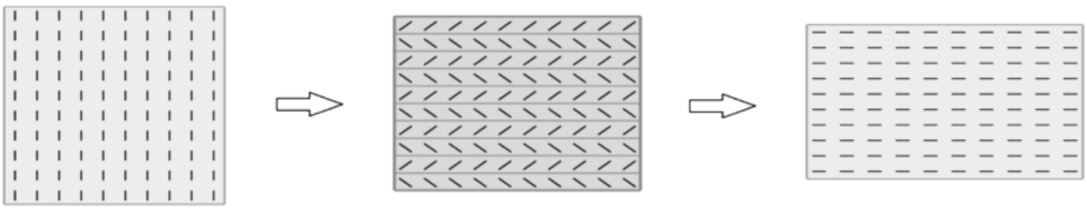


FIGURE 3.1: Schematics of nematic LCE with initial uniform director field aligned vertically developing periodic shear stripes under uniaxial stretch perpendicular to the director before the director is fully rotated in the horizontal direction.

In a Cartesian system of coordinates, we define the nematic director in the reference and stretched configuration, respectively, as

$$\boldsymbol{n}_0 = \begin{bmatrix} 1 \\ 0 \\ 0 \end{bmatrix}, \qquad \boldsymbol{n} = \begin{bmatrix} \cos\theta \\ \sin\theta \\ 0 \end{bmatrix}, \tag{3.4}$$

where $\theta \in [0, \pi/2]$ is the angle between $\boldsymbol{n}$ and $\boldsymbol{n}_0$. The associated natural deformation tensors take the form, respectively,

$$\boldsymbol{G}_0 = \begin{bmatrix} a^{1/3} & 0 & 0 \\ 0 & a^{-1/6} & 0 \\ 0 & 0 & a^{-1/6} \end{bmatrix}, \tag{3.5}$$

and

$$\boldsymbol{G} = \begin{bmatrix} a^{-1/6} + (a^{1/3} - a^{-1/6})\cos^2\theta & (a^{1/3} - a^{-1/6})\sin\theta\cos\theta & 0 \\ (a^{1/3} - a^{-1/6})\sin\theta\cos\theta & a^{-1/6} + (a^{1/3} - a^{-1/6})\sin^2\theta & 0 \\ 0 & 0 & a^{-1/6} \end{bmatrix}, \tag{3.6}$$

where a is defined in terms of Q as

$$a = \frac{1+2Q}{1-Q}, \tag{3.7}$$

and we emphasise that Q, and therefore a, is fixed.

To demonstrate shear striping, we take the following perturbed deformation gradient

$$\boldsymbol{F} = \begin{bmatrix} \lambda^{-1/2} & 0 & 0 \\ \varepsilon & \lambda & 0 \\ 0 & 0 & \lambda^{-1/2} \end{bmatrix}, \tag{3.8}$$

where $\lambda > 1$ is the finite stretch ratio in the tensile direction and $0 < \varepsilon \ll 1$ is the small shear perturbation. The corresponding elastic deformation tensor is equal to

$$\begin{aligned} \boldsymbol{A} = &\begin{bmatrix} \lambda^{-1/2}(a^{1/2}\sin^2\theta + \cos^2\theta) & \lambda(a^{-1/2}-1)\sin\theta\cos\theta & 0 \\ \lambda^{-1/2}(1-a^{1/2})\sin\theta\cos\theta & \lambda(a^{-1/2}\sin^2\theta + \cos^2\theta) & 0 \\ 0 & 0 & \lambda^{-1/2} \end{bmatrix} \\ &+ \varepsilon \begin{bmatrix} (1-a^{1/2})\sin\theta\cos\theta & 0 & 0 \\ (\sin^2\theta + a^{1/2}\cos^2\theta) & 0 & 0 \\ 0 & 0 & 0 \end{bmatrix}. \end{aligned} \tag{3.9}$$

We study these perturbations around two equilibrium solutions where λ is finite and fixed and $(\varepsilon, \theta) = (0, 0)$ or $(\varepsilon, \theta) = (0, \pi/2)$, corresponding to the director being perpendicular (when in the reference state) or parallel (when fully rotated) to the applied tensile force, respectively.

We denote by $\mathcal{W}(\lambda, \varepsilon, \theta)$ the strain-energy function (3.1), depending only on λ, ε and θ. This takes the form

$$\begin{aligned}\mathcal{W}(\lambda,\varepsilon,\theta) =& \frac{\mu^{(1)}}{2}(\lambda^2 + 2\lambda^{-1} + \varepsilon^2 - 3) \\ &+ \frac{\mu^{(2)}}{2}\{[\lambda^{-1/2}(a^{1/2}\sin^2\theta + \cos^2\theta) + \varepsilon(1-a^{1/2})\sin\theta\cos\theta]^2 \\ &+ [\lambda^{-1/2}(1-a^{1/2})\sin\theta\cos\theta + \varepsilon(\sin^2\theta + a^{1/2}\cos^2\theta)]^2 \\ &+ [\lambda(a^{-1/2}-1)\sin\theta\cos\theta]^2 + [\lambda(a^{-1/2}\sin^2\theta + \cos^2\theta)]^2 + \lambda^{-1} - 3\}.\end{aligned} \tag{3.10}$$

When the finite stretch ratio λ is specified, the equilibrium solution satisfies the following simultaneous equations for energy minimisation

$$\frac{\partial \mathcal{W}(\lambda,\varepsilon,\theta)}{\partial \varepsilon} = 0 \quad \text{and} \quad \frac{\partial \mathcal{W}(\lambda,\varepsilon,\theta)}{\partial \theta} = 0. \tag{3.11}$$

Differentiating $\mathcal{W}$ in equation (3.10) with respect to ε and θ, respectively, gives

$$\begin{aligned}\frac{\partial \mathcal{W}(\lambda,\varepsilon,\theta)}{\partial \varepsilon} =& \mu^{(1)}\varepsilon \\ &+ \mu^{(2)}\{[\lambda^{-1/2}(a^{1/2}\sin^2\theta + \cos^2\theta) \\ &+ \varepsilon(1-a^{1/2})\sin\theta\cos\theta](1-a^{1/2})\sin\theta\cos\theta \\ &+ [\lambda^{-1/2}(1-a^{1/2})\sin\theta\cos\theta \\ &+ \varepsilon(\sin^2\theta + a^{1/2}\cos^2\theta)](\sin^2\theta + a^{1/2}\cos^2\theta)\}\end{aligned} \tag{3.12}$$

and

$$\begin{aligned}\frac{\partial \mathcal{W}(\lambda,\varepsilon,\theta)}{\partial\theta} =&\mu^{(2)}\{(a^{1/2}-1)[2\lambda^{-1/2}\sin\theta\cos\theta+\varepsilon(\sin^2\theta-\cos^2\theta)]\\ &\times[\lambda^{-1/2}(a^{1/2}\sin^2\theta+\cos^2\theta)+\varepsilon(1-a^{1/2})\sin\theta\cos\theta]\\ &+(a^{1/2}-1)[\lambda^{-1/2}(\sin^2\theta-\cos^2\theta)-2\varepsilon\sin\theta\cos\theta]\\ &\times[\lambda^{-1/2}(1-a^{1/2})\sin\theta\cos\theta+\varepsilon(\sin^2\theta+a^{1/2}\cos^2\theta)]\\ &+\lambda^2(a^{-1}-1)\sin\theta\cos\theta\}.\end{aligned} \tag{3.13}$$

At $\varepsilon = 0$ and $\theta = 0$, the partial derivatives defined by equations (3.12)-(3.13) are equal to zero, i.e., this solution is always an equilibrium state. For sufficiently small values of ε and θ, we can write the second order approximation as

$$\mathcal{W}(\lambda,\varepsilon,\theta)\approx\mathcal{W}(\lambda,0,0)+\frac{1}{2}\left(\varepsilon^2\frac{\partial^2\mathcal{W}}{\partial\varepsilon^2}(\lambda,0,0)+2\varepsilon\theta\frac{\partial^2\mathcal{W}}{\partial\varepsilon\partial\theta}(\lambda,0,0)+\theta^2\frac{\partial^2\mathcal{W}}{\partial\theta^2}(\lambda,0,0)\right), \tag{3.14}$$

where

$$\frac{\partial^2\mathcal{W}}{\partial\varepsilon^2}(\lambda,0,0)=\mu^{(1)}+\mu^{(2)}a, \tag{3.15}$$

$$\frac{\partial^2\mathcal{W}}{\partial\varepsilon\partial\theta}(\lambda,0,0)=\mu^{(2)}\lambda^{-1/2}(1-a), \tag{3.16}$$

$$\frac{\partial^2\mathcal{W}}{\partial\theta^2}(\lambda,0,0)=\mu^{(2)}(\lambda^2-\lambda^{-1}a)(a^{-1}-1). \tag{3.17}$$

First, we find the equilibrium values θ_0 for θ as a function of ε by solving the second equation in (3.11). By the approximation (3.14), the corresponding equation takes the form

$$\varepsilon\frac{\partial^2\mathcal{W}}{\partial\varepsilon\partial\theta}(\lambda,0,0)+\theta\frac{\partial^2\mathcal{W}}{\partial\theta^2}(\lambda,0,0)=0, \tag{3.18}$$

implying

$$\theta_0(\varepsilon) = -\varepsilon \frac{\partial^2 \mathcal{W}}{\partial \varepsilon \partial \theta}(\lambda, 0, 0) / \frac{\partial^2 \mathcal{W}}{\partial \theta^2}(\lambda, 0, 0). \tag{3.19}$$

Next, substituting $\theta = \theta_0(\varepsilon)$ in (3.14) yields the following function in ε,

$$\mathcal{W}(\lambda, \varepsilon, \theta_0(\varepsilon)) - \mathcal{W}(\lambda, 0, 0) \approx \frac{\varepsilon^2}{2} \left[\frac{\partial^2 \mathcal{W}}{\partial \varepsilon^2}(\lambda, 0, 0) - \left(\frac{\partial^2 \mathcal{W}}{\partial \varepsilon \partial \theta}(\lambda, 0, 0) \right)^2 / \frac{\partial^2 \mathcal{W}}{\partial \theta^2}(\lambda, 0, 0) \right]. \tag{3.20}$$

Depending on whether the expression on the right-hand side is negative, zero, or positive, the respective equilibrium state is unstable, neutrally stable, or stable. We deduce that the equilibrium state with $\varepsilon = 0$ and $\theta = 0$ is unstable if

$$a^{1/3} \left(\frac{\eta + 1}{\eta + a} \right)^{1/3} < \lambda < a^{1/3}, \tag{3.21}$$

where $\eta = \mu^{(1)}/\mu^{(2)}$. Outside these bounds of stretch λ, the director $\boldsymbol{n}$ is aligned in the direction of applied force.

Similarly, at $\varepsilon = 0$ and $\theta = \pi/2$, both the partial derivatives defined by (3.12)-(3.13) are equal to zero, and

$$\frac{\partial^2 \mathcal{W}}{\partial \varepsilon^2}(\lambda, 0, \pi/2) = \mu^{(1)} + \mu^{(2)}, \tag{3.22}$$

$$\frac{\partial^2 \mathcal{W}}{\partial \varepsilon \partial \theta}(\lambda, 0, \pi/2) = \mu^{(2)} \lambda^{-1/2} (a - 1), \tag{3.23}$$

$$\frac{\partial^2 \mathcal{W}}{\partial \theta^2}(\lambda, 0, \pi/2) = \mu^{(2)} (\lambda^2 - \lambda^{-1} a)(1 - a^{-1}). \tag{3.24}$$

Thus the equilibrium state with $\varepsilon = 0$ and $\theta = \pi/2$ is unstable if

$$a^{1/3} < \lambda < a^{1/3} \left(\frac{\eta + a}{\eta + 1} \right)^{1/3}. \tag{3.25}$$

Outside these bounds of stretch λ, the director $\boldsymbol{n}$ is aligned in the direction of applied force.

Therefore, shear stripes can form when λ satisfies

$$a^{1/3}\left(\frac{\eta+1}{\eta+a}\right)^{1/3} < \lambda < a^{1/3}\left(\frac{\eta+a}{\eta+1}\right)^{1/3}. \tag{3.26}$$

For the corresponding equilibrium solution, the shear parameter and director angle take the following explicit forms, respectively,

$$\varepsilon_0 = \pm\frac{\sqrt{[\lambda^3(\eta+a)-a(\eta+1)][a(\eta+a)-\lambda^3(\eta+1)]}}{a\lambda^{1/2}(2\eta+a+1)}, \tag{3.27}$$

$$\theta_0 = \pm\arctan\sqrt{\frac{\lambda^3(\eta+a)-a(\eta+1)}{a(\eta+a)-\lambda^3(\eta+1)}}. \tag{3.28}$$

At these values of ε_0 and θ_0, the partial derivative defined by equation (3.12) is equal to zero. For the equation (3.13), only the term of $\mathcal{O}(\varepsilon^2)$ is non-zero. Since ε is the pertrubation parameter with value $0 < \varepsilon \ll 1$, the higher order term is sufficiently small to be neglected in our case.

The gradient tensors for alternating shear deformations in two adjacent stripe subdomains are $\boldsymbol{F}_\pm$ with $\varepsilon = \pm\varepsilon_0$, respectively. These two deformations are geometrically compatible in the sense that $\boldsymbol{F}_+$ and $\boldsymbol{F}_-$ are rank-one connected, i.e., $\operatorname{rank}(\boldsymbol{F}_+ - \boldsymbol{F}_-) = 1$.

The nondimensionalised strain-energy function $\mathcal{W}(\lambda, \varepsilon, \theta)$ (i.e., the function divided by $\mu^{(2)}$) described by equation (3.10), with $\eta = \mu^{(1)}/\mu^{(2)} = 1$, is illustrated in figure 3.2. For λ with values between the lower and upper bounds given by (3.26), the minimum energy is attained for $(\varepsilon, \theta) = (\varepsilon_0, \theta_0)$ provided by equations (3.27)-(3.28). Figure 3.3 depicts the positive values of the shear parameter ε_0 and director angle θ_0 described by equations (3.27) and (3.28), respectively, for different parameter ratios η. When $\eta = 0$, corresponding to the neoclassical form, shear stripes form for $\lambda \in (1, a^{2/3})$. When $\eta \to \infty$ there is no shear striping since the material is practically purely elastic.

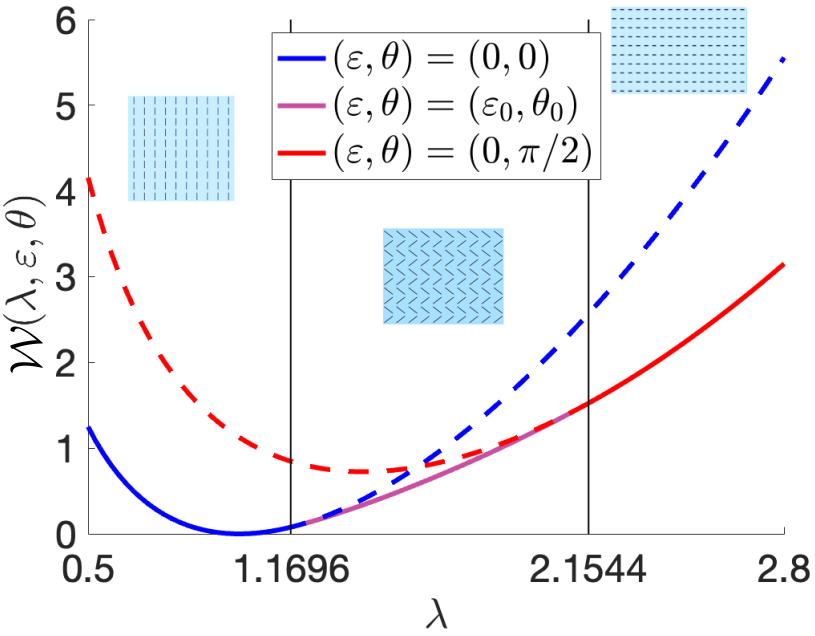


FIGURE 3.2: The nondimensionalised strain-energy function $\mathcal{W}(\lambda,\varepsilon,\theta)$ given by equation (3.10), for $(\varepsilon,\theta) = (0,0), (\varepsilon,\theta) = (\varepsilon_0,\theta_0)$ and $(\varepsilon,\theta) = (0,\pi/2)$, when $a = 4$ and $\eta = 1$. The two vertical lines correspond to the lower and upper bounds on λ. Between these bounds, the second solution, with $(\varepsilon,\theta) = (\varepsilon_0,\theta_0)$, minimises the energy.

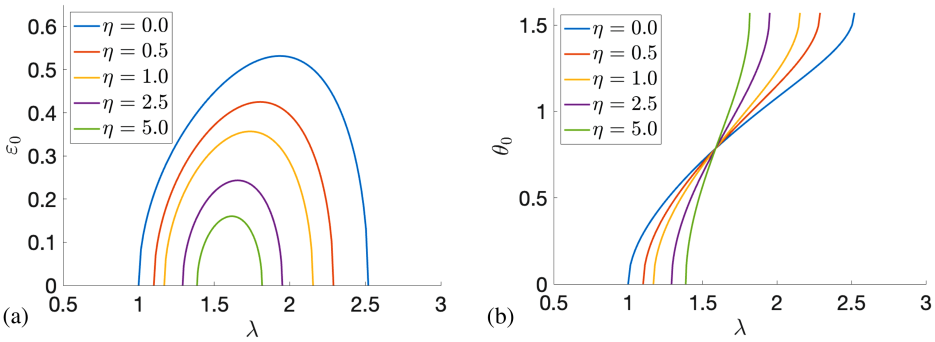


FIGURE 3.3: The positive values of the (a) shear parameter ε_0 and (b) director angle θ_0 given by equations (3.27)-(3.28), for different values of the parameter ratio η when $a = 4$.

3.1.2 Optimal stripe width

For shear striping, the width of each subdomain depends on the material properties, sample geometry and boundary conditions. Dirichlet conditions, where the director at both ends of the LCE sample in its initial orientation are fixed, i.e., perpendicular to the longitudinal direction, known as strong anchoring, play an important role in numerically capturing this property. To estimate the stripe width, we add the Frank energy density to our model function, as follows,

$$\mathcal{W}^{(nlce)} = \mathcal{W}^{(lce)} + \frac{K}{2}|\boldsymbol{F}^T \operatorname{Grad} \boldsymbol{n}|^2, \tag{3.29}$$

where $\mathcal{W}^{(lce)}$ is as defined in equation (3.1) and K is the Frank constant [1, 74].

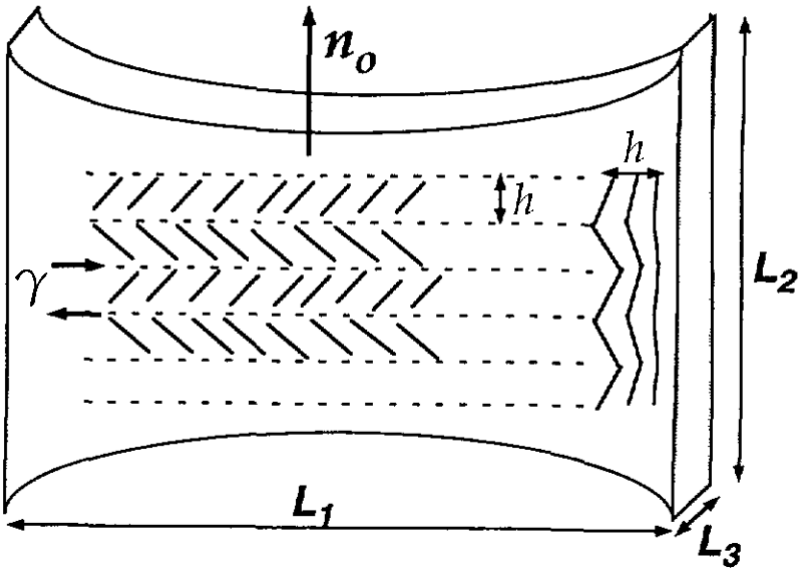


FIGURE 3.4: LCE sample with stripe domains. Local shear decay at the ends of the sample forming a strip band parallel to the initial director of width equal to the stripe width h [80].

We denote by L_1, L_2, L_3 the size of the undeformed LCE sample in the extension direction (which is perpendicular to the director orientation in the

undeformed state), the width direction (which is parallel to the initial director), and the thickness direction, respectively. Provided that Dirichlet boundary conditions are imposed at the ends, the width h of a strip band forming parallel to the initial director at each of these ends must be of the same order of magnitude as that of a shear stripe [80]. For geometric compatibility, the displacement in such a strip band must be equal to γh, where $\gamma = \lambda_{12}(x_1, x_2)$ denotes the shear strain in a shear stripe, so that

$$\frac{d\lambda_{12}}{dx_2} = \frac{d\lambda_{22}}{dx_1}, \tag{3.30}$$

with $\lambda_{22} \approx h$ representing the stretch ratio in the direction of the stripe width. Due to the infinitesimal scale of the strip band width, the linear elastic framework is suitable to analyse their deformation. The corresponding elastic energy is then approximately

$$E_{end} \approx \frac{1}{2}\mu\gamma^2(2L_3h^2)\frac{L_2}{h} = \mu\gamma^2 L_2 L_3 h, \tag{3.31}$$

where L_3h^2 is the volume of one end region for a single shear stripe and L_2/h is the number of stripes. This elastic energy in (3.31) decreases as h decreases.

There is additional elastic energy at the narrow interface between adjacent stripes with opposite shear deformation and director rotation. Since the director angle $\theta \in (-\theta_0, \theta_0)$ varies from one side of the interface to the other, so that it takes the value zero in the middle of the interval, this energy is approximately

$$E_{int} \approx L_1 L_3 \sqrt{\mu K}\left(\frac{L_2}{h} - 1\right) \tag{3.32}$$

where $\sqrt{\mu K}$ is the effective surface tension, L_1L_3 is the area of a single interface, and $L_2/h - 1$ is the number of interfaces. This energy in (3.32) tends

to decrease when h increases. The problem is then to find the optimal stripe width h that minimises the total energy

$$E_{stripe} = E_{end} + E_{int}. \tag{3.33}$$

Differentiating the above function in (3.33) with respect to h and solving for the critical value, we obtain

$$h \approx \left(L\sqrt{\frac{K}{\mu}} \right)^{1/2}. \tag{3.34}$$

This means the stripe width increases with sample initial length $L_1 = L$ and nematic penetration depth $\sqrt{K/\mu} \approx 10^{-8}$ m, which measures the competition between polymer and Frank elasticity. A typical value for the stripe width is $h \approx 10^{-5}$ m.

3.2 Necking

To study necking, we denote by $\mathcal{W}(\lambda)$ the strain-energy function given by equation (3.1) in terms of eigenvalues of the deformation gradient $\boldsymbol{F}$ as λ_1, λ_2, and λ_3 and of $\boldsymbol{A} = \boldsymbol{G}^{-1}\boldsymbol{F}\boldsymbol{G}_0$ as α_1, α_2, and α_3. In this case, we have,

$$\mathcal{W}^{(}\lambda) = \frac{\mu^{(1)}}{2}(\lambda_1^2 + \lambda_2^2 + \lambda_3^2 - 3) + \frac{\mu^{(2)}}{2}(\alpha_1^2 + \alpha_2^2 + \alpha_3^2 - 3). \tag{3.35}$$

The LCE is subject to the finite-strain deformation with $\lambda_1 = \lambda > 1$ and $\lambda_2 = \lambda_3 = \lambda^{-1/2}$, while the tensile force is parallel to the nematic director. The corresponding natural deformation tensors $\boldsymbol{G}$ is given by

$$\boldsymbol{G} = \mathrm{diag}(a^{-1/6}, a^{-1/6}, a^{1/3}), \tag{3.36}$$

where natural shape parameter $a = (1+2Q)/(1-Q)$. Taking $\boldsymbol{G}_0 = \boldsymbol{I}$, we have

$$\lambda_1 = \alpha_1 \left(\frac{1+2Q}{1-Q}\right)^{1/3} = \lambda, \quad \lambda_2 = \alpha_2 \left(\frac{1-Q}{1+2Q}\right)^{1/6}, \quad \lambda_3 = \alpha_3 \left(\frac{1-Q}{1+2Q}\right)^{1/6} \tag{3.37}$$

and

$$\alpha_1 = \lambda \left(\frac{1+2Q}{1-Q}\right)^{-1/3} = \alpha, \quad \alpha_2 = \alpha_3 = \lambda^{-1/2} \left(\frac{1-Q}{1+2Q}\right)^{-1/6} = \alpha^{-1/2}. \tag{3.38}$$

For uniaxial tension, the principal components of the first Piola-Kirchhoff stress tensor are, respectively,

$$P_1 = \frac{\partial \mathcal{W}}{\partial \lambda_1} - p\lambda_1^{-1} = P > 0, \tag{3.39}$$

$$P_2 = \frac{\partial \mathcal{W}}{\partial \lambda_2} - p\lambda_2^{-1} = 0, \tag{3.40}$$

$$P_3 = \frac{\partial \mathcal{W}}{\partial \lambda_3} - p\lambda_3^{-1} = 0, \tag{3.41}$$

where p is the Lagrange multiplier for the incompressibility constraint.

The first derivative of $\mathcal{W}$ with the stretch ratio λ as the only variable is equal to the applied tensile stress, i.e.,

$$\mathcal{W}'(\lambda) = (P_1 + p\lambda_1^{-1})\frac{\partial \lambda_1}{\partial \lambda} + p\lambda_2^{-1}\frac{\partial \lambda_2}{\partial \lambda} + p\lambda_3^{-1}\frac{\partial \lambda_3}{\partial \lambda} = P, \tag{3.42}$$

and necking forms when the applied stress P first increases, then decreases, then increases again as λ increases [81]. It is shown in the next section that, when Q is constant, $\mathcal{W}''(\lambda) > 0$, therefore, necking cannot occur.

We let Q depend on the deformation through the following constitutive relation obtained by calibration to experimental data of [82] (see figure 3.5(a)):

$$Q = 0.35\left[\frac{e^{16(\lambda-1.45)}-1}{e^{16(\lambda-1.45)}+1} - \frac{e^{16}-1}{e^{16}+1} + 2\right], \quad \text{for } \lambda \geq 1. \tag{3.43}$$

It remains to verify numerically that the second derivative $\mathcal{W}''(\lambda)$ of $\mathcal{W}(\lambda)$ will change sign for some $\lambda \in (1,2)$. For different values of $\eta = \mu^{(1)}/\mu^{(2)}$, the nondimensionalised function $\mathcal{W}(\lambda)$ (i.e., the function divided by $\mu^{(2)}$) and its first two derivatives are plotted in figure 3.5(b)-(d), respectively. These plots suggest that, as η increases, the necking interval (i.e., the interval where $\mathcal{W}''(\lambda) < 0$) decreases, and there is a critical value $\eta_{crt} \approx 4.55$ above which necking does not form. For example, when $\eta = 3$, $\mathcal{W}''(\lambda)$ changes from positive to negative at $\lambda_* \approx 1.28$, then from negative to positive at $\lambda^* \approx 1.37$. In this case, necking occurs for $1.28 < \lambda < 1.37$. When $\eta \to \infty$ the model reduces to the neo-Hookean model for rubber, which does not exhibit necking.

3.2.1 Neoclassical model cannot predict necking

In this section, we consider the following strain-energy function describing a nematic LCE,

$$\mathcal{W}^{(nc)}(\boldsymbol{F}, \boldsymbol{n}) = \mathcal{W}(\boldsymbol{A}), \tag{3.44}$$

where $\boldsymbol{F}$ represents the macroscopic deformation gradient from the cross-linking state, $\boldsymbol{n}$ is the nematic director in the present configuration, and $\mathcal{W}(\boldsymbol{A})$ is the strain-energy density of the isotropic polymer network, depending only on the (local) elastic deformation tensor $\boldsymbol{A} = \boldsymbol{G}^{-1}\boldsymbol{F}\boldsymbol{G}_0$, with $\boldsymbol{G}_0$ and $\boldsymbol{G}$ the natural deformation tensors due to liquid crystal director in the reference and current configuration, respectively.

The LCE is subject to the finite-strain deformation with $\lambda_1 = \lambda > 1$ and

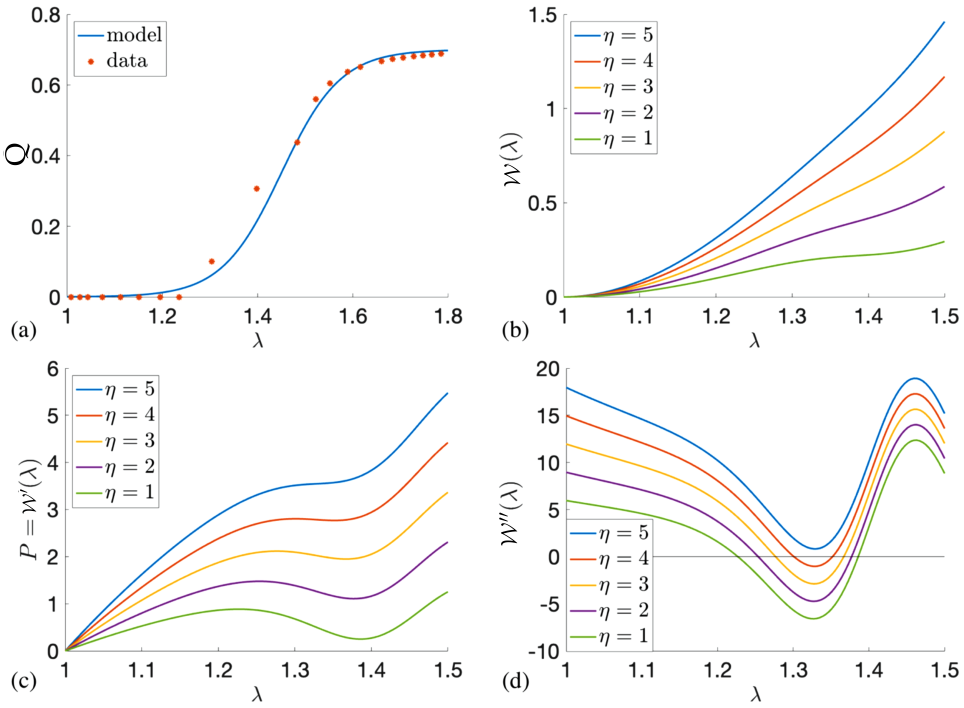


FIGURE 3.5: (a) The uniaxial order parameter Q given by equation (12) and the associated experimental data [14]; (b) The nondimensionalised strain-energy function $\mathcal{W}(\lambda)$, for different values of $\eta = \mu^{(1)}/\mu^{(2)}$; (c) The applied tensile stress $P = \mathcal{W}'(\lambda)$; (d) The second derivative $\mathcal{W}''(\lambda)$ of the strain-energy function $\mathcal{W}(\lambda)$.

$\lambda_2 = \lambda_3 = \lambda^{-1/2}$, while the tensile force is parallel to the nematic director. Let $\boldsymbol{G}_0 = \boldsymbol{I}$, so that

$$\alpha_1 = \lambda \left(\frac{1+2Q}{1-Q}\right)^{-1/3} = \alpha, \quad \alpha_2 = \alpha_3 = \lambda^{-1/2} \left(\frac{1-Q}{1+2Q}\right)^{-1/6} = \alpha^{-1/2}, \tag{3.45}$$

where $Q \in (0,1)$ is the scalar uniaxial order parameter in the current configuration.

For hyperelastic materials where the force-extension curve does not have a maximum, the homogeneous deformation is the only absolute minimiser of the elastic energy, hence necking cannot occur [83]. Here, we show that, if Q is constant and the hyperelastic model described by $\mathcal{W}(\boldsymbol{A})$ does not exhibit

necking, then the LCE model $\mathcal{W}^{(nc)}(\boldsymbol{F})$ does not present necking either.

To prove this, we denote by $w(\lambda)$ the strain-energy function $\mathcal{W}^{(nc)}(\boldsymbol{F})$ given by equation (3.44), depending only on λ, and by $\tilde{w}(\alpha)$ the strain-energy function depending only on α as follows:

$$w(\lambda) = \frac{\mu^{(2)}}{2}(\lambda_1^2+\lambda_2^2+\lambda_3^2-3) = \frac{\mu^{(2)}}{2}(\lambda^2+2\lambda^{-1}-3), \tag{3.46}$$

$$\tilde{w}(\alpha) = \frac{\mu^{(2)}}{2}(\alpha_1^2+\alpha_2^2+\alpha_3^2-3) = \frac{\mu^{(2)}}{2}(\alpha^2+2\alpha^{-1}-3). \tag{3.47}$$

Calculating the first and second derivatives, we obtain

$$\frac{dw(\lambda)}{d\lambda} = \frac{d\tilde{w}(\alpha)}{d\alpha}\frac{d\alpha}{d\lambda} = \frac{d\tilde{w}(\alpha)}{d\alpha}\left(\frac{1+2Q}{1-Q}\right)^{-1/3} \tag{3.48}$$

and

$$\frac{d^2w(\lambda)}{d\lambda^2} = \frac{d^2\tilde{w}(\alpha)}{d\alpha^2}\left(\frac{d\alpha}{d\lambda}\right)\left(\frac{1+2Q}{1-Q}\right)^{-1/3} = \frac{d^2\tilde{w}(\alpha)}{d\alpha^2}\left(\frac{1+2Q}{1-Q}\right)^{-2/3} > 0. \tag{3.49}$$

The last inequality holds since, by assumption, there is no necking for the polymeric network, hence $d^2\tilde{w}/d\alpha^2 > 0$. It follows that $d^2w/d\lambda^2 > 0$, i.e., for the LCE described by equation (3.44), necking will not form.

In particular, since we did not specify the hyperelastic strain-energy function and incompressible neo-Hookean or Mooney-Rivlin hyperelastic models do not exhibit necking, this property is inherited by the associated LCE models of the form given by equation (3.44).

3.3 Discussion

The original contributions of this chapter consist of:

- The analytical solution for shear-striping instability when Q is constant, including derivation of the optimal stripe width.
- A novel model with Q depending on the deformation, so that necking instability is captured.

Finite element simulation of these phenomena are presented and discussed in chapter 6.

Chapter 4

Viscoelasticity in LCEs

Many studies have reported the viscoelastic nature of LCEs [51, 84]. While the traditional natural rubber's viscoelasticity is due to the dynamics of viscous network, LCEs viscous response is both due to the network and reorientation of LC molecules. The coupled behaviour results in unique rate dependent characteristics under loading and unloading test.

4.1 Coupled viscoelastic response

A number of previous studies shows that the characteristic time scales for the mesogen rotation and the network extension are different from each other. The study of [85] shows that the director rotates about one order of magnitude faster than the relaxation of the mechanical deformation. Similarly, the study in [52] shows two distinct regions for long-time stress relaxation. They found that short time relaxation is facilitated by the director rotation due to polydomain-to-monodomain transformation, while the long-time relaxation is due to mechanical extension of network when the sample behaves like an isotropic rubber. The shape recovery of LCEs takes a very long

time and requires a very slow loading rate of around $10^{-4}\ s^{-1}$ to reach quasi-equilibrium [52, 84]. All these finding point to one main conclusion that the director rotates slightly faster in comparison to the network deformation.

Cross-linking condition, director angle, nematic order and other parameters could affect the viscoelastic response of LCE. However, the comprehensive understanding of viscoelasticity in LCEs is challenging due to the complicated coupling of network and directors.

4.2 Continuum models for viscoelastic response

To capture the viscous effect of both mesogen and polymeric network, some viscoelastic models have been developed. The viscoelastic model developed by Wang et al. [64] is based on the multiplicative decomposition which is widely used for modelling viscoelastic elastomers [64, 86]. This model is based on the neoclassical free energy and the semi-soft energy density. However, only the network deformation gradient is multiplicatively decomposed while the director is treated as an internal variable which is governed by the dissipative equation. The free energy of the model is devoid of the Frank energy.

Here, we build a new model in which both the network deformation gradient and the soft-elasticity deformation gradient are multiplicatively decomposed and the Frank energy is also considered. In our model, director rotation is an independent variable having its own governing equation.

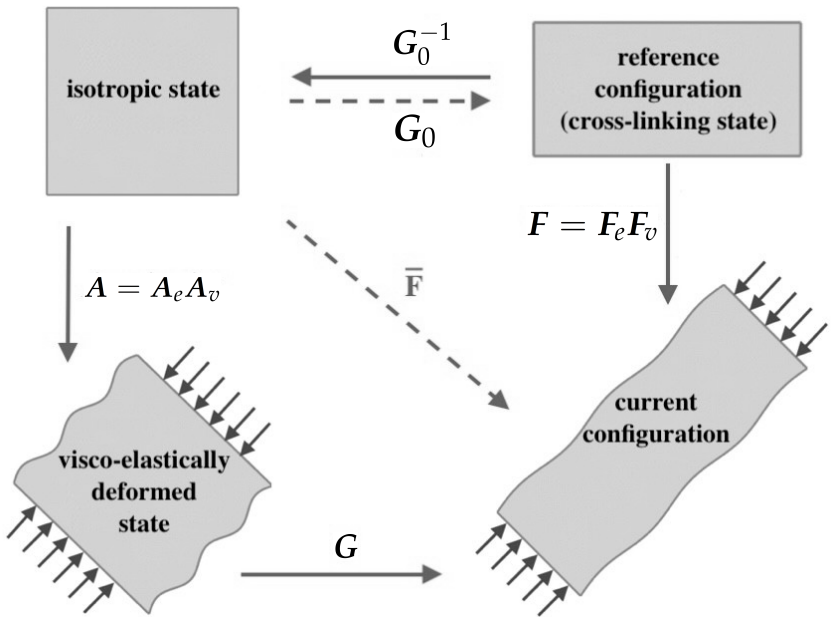


FIGURE 4.1: Multiplicative decomposition of the deformation gradients

4.2.1 Kinematics and model function

The elastic behaviour of a nematic LCE can be described by a strained-energy density function introduced in chapter 2

$$\mathcal{W}(\boldsymbol{F}, \boldsymbol{n}, \text{Grad } \boldsymbol{n}) = \mathcal{W}^{(1)}(\boldsymbol{F}) + \mathcal{W}^{(2)}(\boldsymbol{A}) + \mathcal{W}^{(3)}(\text{Grad } \boldsymbol{n}). \tag{4.1}$$

To model the viscoelastic properties of the LCE, one popular approach used for the rubber network [86] is to decompose the deformation gradient into an elastic and a viscous part. Here, we extend this approach to both the tensors $\boldsymbol{F}$ and $\boldsymbol{A}$, which we decompose multiplicatively as (see figure 4.1)

$$\boldsymbol{F} = \boldsymbol{F}_e \boldsymbol{F}_v, \qquad \boldsymbol{A} = \boldsymbol{A}_e \boldsymbol{A}_v. \tag{4.2}$$

The rheological model is composed of a Maxwell unit with a non-equilibrium spring and a dashpot connected in series for both the network branch and

soft-elasticity branch as shown in figure 4.2.

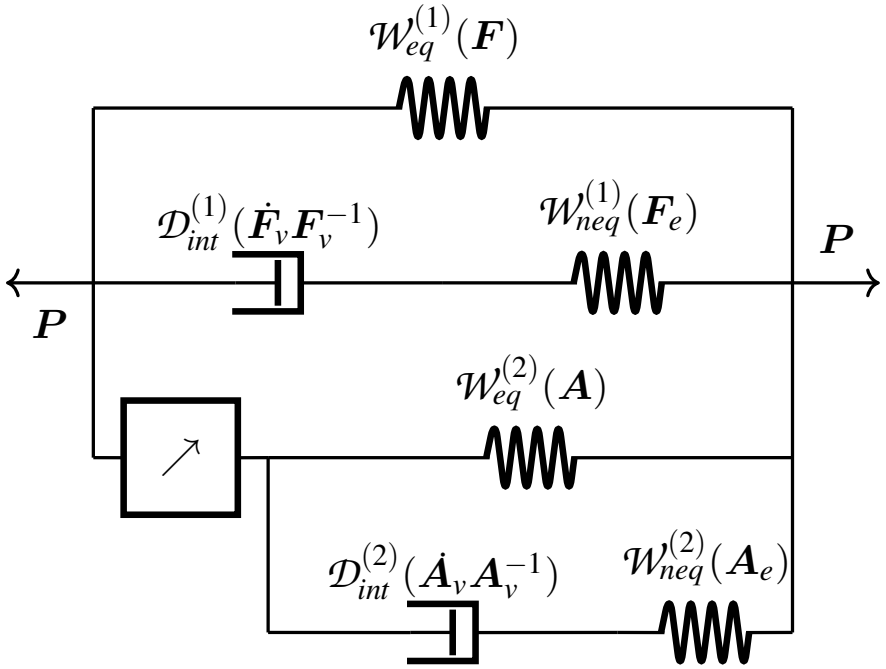


FIGURE 4.2: Rheology model for the viscoelastic behaviour of a nematic LCE consisting of a Maxwell unit with a non-equilibrium spring and a dashpot connected in series for both the network branch and soft-elasticity branch.

The new model function for the viscoelastic LCE is

$$\mathcal{W}(\boldsymbol{F},\boldsymbol{n},\text{Grad }\boldsymbol{n},\boldsymbol{F}_v,\boldsymbol{A}_v) = \mathcal{W}_{eq}^{(1)}(\boldsymbol{F}) + \mathcal{W}_{neq}^{(1)}(\boldsymbol{F}_v) + \mathcal{W}_{eq}^{(2)}(\boldsymbol{A}) + \mathcal{W}_{neq}^{(2)}(\boldsymbol{A}_v) + \mathcal{W}^{(3)}(\text{Grad }\boldsymbol{n}), \tag{4.3}$$

where the equilibrium terms with an '*eq*' index describe the rate-independent elastic response and the non-equilibrium terms with a '*neq*' index characterise the rate-dependent viscous response of the material. Note that $\mathcal{W}_{eq}^{(1)}(\boldsymbol{F})$, $\mathcal{W}_{eq}^{(2)}(\boldsymbol{A})$ and $\mathcal{W}^{(3)}(\text{Grad }\boldsymbol{n})$ correspond to the first, second, and third terms, respectively, of the elastic version of the model in equation (4.1).

For simplicity, we choose

$$\mathcal{W}^{(1)}_{eq}(\boldsymbol{F}) = \frac{\mu^{(1)}_{eq}}{2}\left[\mathrm{tr}\,(\boldsymbol{F}^T\boldsymbol{F}) - 3\right], \qquad \mathcal{W}^{(1)}_{neq}(\boldsymbol{F}_v) = \frac{\mu^{(1)}_{neq}}{2}\left[\mathrm{tr}\,(\boldsymbol{F}_e^T\boldsymbol{F}_e) - 3\right], \quad (4.4)$$

$$\mathcal{W}^{(2)}_{eq}(\boldsymbol{F},\boldsymbol{n}) = \frac{\mu^{(1)}_{eq}}{2}\left[\mathrm{tr}\,(\boldsymbol{A}^T\boldsymbol{A}) - 3\right], \qquad \mathcal{W}^{(2)}_{neq}(\boldsymbol{A}_v) = \frac{\mu^{(1)}_{neq}}{2}\left[\mathrm{tr}\,(\boldsymbol{A}_e^T\boldsymbol{A}_e) - 3\right], \quad (4.5)$$

i.e., neo-Hookean-type models for the components of $\mathcal{W}^{(1)}$ and neo-classical-type models [1] for the components of $\mathcal{W}^{(2)}$. These can be replaced with more sophisticated models, like Gent model, if necessary. It is well known that, in rubber elasticity, the neo-Hookean model can only describe elastic behaviours at lower strains [87]. By contrast, for LCEs where director rotation occurs, larger strain deformation phenomena can be captured by neo-Hookean-based model. Notably, shear-stripes formation in elongated LCEs is demonstrated both theoretically and numerically by the neoclassical and other neo-Hookean-based models. We further set $\mathcal{W}^{(3)}(\mathrm{Grad}\ \boldsymbol{n}) = \frac{K}{2}\left|\mathrm{Grad}\ \boldsymbol{n}\right|^2$, which is the one-term Frank energy density [1].

4.2.2 Thermodynamics consistency and evolution equations

Assuming an in-plane nematic orientation $\boldsymbol{n} = (\cos\theta, \sin\theta, 0)$, the second law of thermodynamics gives the isothermal Clausius-Duhem inequality requirement (derived in chapter 2)

$$\mathcal{D}_{int} = \boldsymbol{P} : \dot{\boldsymbol{F}} - \dot{\mathcal{W}} + g_\theta\dot{\theta} + \boldsymbol{\pi}_\theta \cdot (\mathrm{Grad}\,\theta)^{\cdot} \geq 0, \quad (4.6)$$

where $\mathcal{D}_{int}$ is the internal dissipation rate, $\boldsymbol{P}$ is the first Piola-Kirchhoff stress tensor, g_θ and $\boldsymbol{\pi}_\theta$ are the orientational stresses., and the over-dot represents

differentiation with respect to time in Newton notation. Following the Coleman-Noll procedure [78] similar to the one used in chapter 2, we have

$$\boldsymbol{P} = \frac{\partial \mathcal{W}}{\partial \boldsymbol{F}} + \frac{\partial \mathcal{W}}{\partial \boldsymbol{A}}, \qquad g_\theta = \frac{\partial \mathcal{W}}{\partial \theta}, \qquad \boldsymbol{\pi}_\theta = \frac{\partial \mathcal{W}}{\partial \mathrm{Grad}\,\theta}, \tag{4.7}$$

and the inequality (4.6) reduces to

$$\mathcal{D}_{int} = -\frac{\partial \mathcal{W}}{\partial \boldsymbol{F}_v} : \dot{\boldsymbol{F}}_v - \frac{\partial \mathcal{W}}{\partial \boldsymbol{A}_v} : \dot{\boldsymbol{A}}_v \geq 0. \tag{4.8}$$

To satisfy the inequality (4.8), we choose

$$\mathcal{D}_{int} = \frac{\eta^{(1)}}{2} \dot{\boldsymbol{F}}_v \boldsymbol{F}_v^{-1} : \dot{\boldsymbol{F}}_v \boldsymbol{F}_v^{-1} + \frac{\eta^{(2)}}{2} \dot{\boldsymbol{A}}_v \boldsymbol{A}_v^{-1} : \dot{\boldsymbol{A}}_v \boldsymbol{A}_v^{-1}, \tag{4.9}$$

where $\eta^{(1)}$ and $\eta^{(2)}$ are the viscous parameters. By comparing the above expression with inequality (4.8), we obtain

$$\frac{\partial \mathcal{W}}{\partial \boldsymbol{F}_v} = -\frac{\eta^{(1)}}{2} \dot{\boldsymbol{F}}_v \boldsymbol{F}_v^{-1} \boldsymbol{F}_v^{-T}, \qquad \frac{\partial \mathcal{W}}{\partial \boldsymbol{A}_v} = -\frac{\eta^{(2)}}{2} \dot{\boldsymbol{A}}_v \boldsymbol{A}_v^{-1} \boldsymbol{A}_v^{-T} \tag{4.10}$$

as the evolution equations for $\boldsymbol{F}_v$ and $\boldsymbol{A}_v$, respectively.

4.3 Discussion

The key novel contribution of this chapter is accounting for the viscoelastic response of LCEs due to director relaxation and the coupling between polymer and director viscoelastic responses. The model is thermodynamically consistent and can be used to simulate the viscoelastic response of LCEs under various loading conditions. It can capture the distinct regimes of stress-strain curves, initial response, the semi-soft behaviour and the large deformation network response. Finite element simulation of these phenomena

are presented and discussed in chapter 6. The decomposition of both deformation tensors, $\boldsymbol{F}$ and $\boldsymbol{A}$, into elastic and viscous parts allows us to capture the different time scales of the director and polymeric network relaxation. Though only one branch of the Maxwell unit (spring and dashpot connected in series) is used for each deformation tensor in the model, more branches can be added to capture more nonlinear viscoelastic behaviour if necessary.

Chapter 5

Finite element formulation

This chapter presents the systematic process of finite element (FE) formulation for solving initial boundary value problems (IBVPs) of liquid crystal elastomers. An IBVP consists of governing equations together with boundary conditions and constitutive relations. For the FE formulation, first the strong form of the governing equation is transformed into weak form by the principle of virtual work (or variational formulation). The weak form is linearized and then discretized both in time and space. Since the problem and equations obtained by the variational formulation are nonlinear, linearized versions are needed to apply Newton-Raphson method [88]. The spatial discretization is obtained by the isoparametric FE method and the temporal discretization by backward Euler method.

5.1 Strong form in reference configuration

The strong form of the governing equations are already derived in chapter 2. The initial boundary value problem in strong form is to find the displacement field $\boldsymbol{u}$ and director vector $\boldsymbol{n}$ determined by the following governing equations

$$\text{Div}\, \boldsymbol{P} = 0 \quad \text{in} \quad \Omega_0, \tag{5.1}$$

$$\text{Div}\, \boldsymbol{\pi}_0 + \boldsymbol{g}_n = 0 \quad \text{in} \quad \Omega_0, \tag{5.2}$$

with boundary conditions

$$\boldsymbol{P}\boldsymbol{N}_0 = \boldsymbol{t} \quad \text{on} \quad \Gamma_1, \tag{5.3}$$

$$\boldsymbol{\pi}_0 \boldsymbol{N}_0 = \boldsymbol{t}_n \quad \text{on} \quad \Gamma_2, \tag{5.4}$$

and initial conditions

$$\boldsymbol{u}(t_0) = \boldsymbol{u}_0, \tag{5.5}$$

$$\boldsymbol{n}(t_0) = \boldsymbol{n}_0, \tag{5.6}$$

where Γ_1 and Γ_2 are the parts of the boundary of the body where force traction and director traction conditions are applied, respectively.

5.2 Weak formulation by the principle of virtual work

The virtual work done by the body due to arbitrary infinitesimal virtual displacement $\delta\boldsymbol{u}$ is given by

$$\delta \mathbb{W}_u = \int_{\Omega_0} \text{Div}\, \boldsymbol{P} \cdot \delta \boldsymbol{u} = 0. \tag{5.7}$$

Using product rule and divergence theorem, this becomes

$$\delta \mathbb{W}_u = \int_{\Omega_0} \boldsymbol{P} : \text{Grad}\, \delta \boldsymbol{u}\, dV - \int_{\partial\Omega_0} \boldsymbol{P}\boldsymbol{N}_0 \cdot \delta \boldsymbol{u}\, dA = 0. \tag{5.8}$$

Using Grad $\delta \boldsymbol{u} = \delta \boldsymbol{F}$ and boundary condition $\boldsymbol{P}\boldsymbol{N}_0 = \boldsymbol{t}_0$, we have

$$\delta \mathbb{W}_u = \int_{\Omega_0} \boldsymbol{P} : \delta \boldsymbol{F}\, dV - \int_{\partial\Omega_0} \boldsymbol{t} \cdot \delta \boldsymbol{u}\, dA = 0. \tag{5.9}$$

In the above equation, the internal work done by the stress is given by the term

$$\delta \mathbb{W}_{u,int} = \int_{\Omega_0} \boldsymbol{P} : \delta \boldsymbol{F}\, dV, \tag{5.10}$$

and the external work is given by the term

$$\delta \mathbb{W}_{u,ext} = -\int_{\partial\Omega_0} \boldsymbol{t} \cdot \delta \boldsymbol{u}\, dA. \tag{5.11}$$

In classical continuum mechanics, the work done by the first Piola-Kirchhoff stress, $\boldsymbol{P} : \delta \boldsymbol{F}$, is equal to the work done by the second Piola-Kirchhoff stress $\boldsymbol{S}$ and its conjugate pair, which is the Green-Lagrange strain $\boldsymbol{E}$, as $\boldsymbol{S} : \delta \boldsymbol{E}$. This is derived considering the symmetry of $\boldsymbol{S}$ in rubber elasticity. However, for LCEs, the stress tensor $\boldsymbol{S}$ is not symmetric in general due to director rotation [89]. Therefore, the advantages of a symmetric tensor cannot be utilized in this case and, we will continue to use the weak form in terms of the first Piola-Kirchhoff stress.

In a similar manner, one can formulate the weak form of the balance of linear momentum due to director vector by multiplying (5.2) with an arbitrary infinitesimal perturbation of angle $\delta \boldsymbol{n}$, which satisfies the boundary conditions

giving

$$\delta \mathbb{W}_n = \int_{\Omega_0} (\text{Div}\, \boldsymbol{\pi}_0 + \boldsymbol{g}_n) \delta \boldsymbol{n}\, dV = 0. \tag{5.12}$$

By the product rule, the divergence theorem and boundary conditions $\boldsymbol{\pi}_0 \boldsymbol{N}_0 = \boldsymbol{t}_n$, we obtain

$$\delta \mathbb{W}_n = \int_{\Omega_0} \boldsymbol{\pi}_0 : \text{Grad}\, \delta \boldsymbol{n}\, dV - \int_{\Omega_0} \boldsymbol{g}_n \cdot \delta \boldsymbol{n}\, dV - \int_{\partial \Omega_0} \boldsymbol{t}_n \cdot \boldsymbol{n}\, dA = 0. \tag{5.13}$$

The internal work done is equal to

$$\delta \mathbb{W}_{n,int} = \int_{\Omega_0} \boldsymbol{\pi}_0 : \text{Grad}\, \delta \boldsymbol{n}\, dV - \int_{\Omega_0} \boldsymbol{g}_n \cdot \delta \boldsymbol{n}\, dV, \tag{5.14}$$

and the external work done is

$$\delta \mathbb{W}_{n,ext} = - \int_{\partial \Omega_0} \boldsymbol{t}_n \cdot \boldsymbol{n}\, dA = 0. \tag{5.15}$$

5.3 Mixed variational formulation

For a hyperelastic material, the strain-energy function $\mathcal{W}$ describes the energy in the solid body. The strain-energy functions for LCEs are discussed in chapter 2. A total potential energy functional Π can be formulated based on the strain-energy function, body force and loads. This is the sum of internal and external potentials. Neglecting the external forces and loads, we have,

$$\Pi(\boldsymbol{u}, \boldsymbol{n}, \text{Grad}\, \boldsymbol{n}) = \int_{\Omega_0} \mathcal{W}^{(lce)}(\boldsymbol{F}, \boldsymbol{n})\, dV + \int_{\Omega_0} \mathcal{W}^{(3)}(\text{Grad}\, \boldsymbol{n})\, dV, \tag{5.16}$$

where

$$\mathcal{W}^{(lce)} = \mathcal{W}^{(1)} + \mathcal{W}^{(2)}., \tag{5.17}$$

The principal of stationary potential energy states that among all the kinematically admissible displacements, the one which fulfils the governing equation is that which make the potential energy functional stationary [90]. The stationary value of a functional Π can be computed by equating to zero the first variation of Π with respect to displacement $\boldsymbol{u}$ as

$$\delta_u \Pi = \int_{\Omega_0} \frac{\partial \mathcal{W}^{(lce)}}{\partial \boldsymbol{F}} : \frac{\partial \boldsymbol{F}}{\partial \boldsymbol{u}} \cdot \delta \boldsymbol{u} \, dV = 0,$$

or equivalently,

$$\delta_u \Pi = \int_{\Omega_0} \boldsymbol{P} : \delta \boldsymbol{F} \, dV = 0. \tag{5.18}$$

Similarly, the stationary value of a functional Π in direction of director $\boldsymbol{n}$ is calculated as

$$\delta_n \Pi = \int_{\Omega_0} \frac{\partial \mathcal{W}^{(3)}}{\partial \text{Grad}\, \boldsymbol{n}} : \text{Grad}\, \delta \boldsymbol{n} \, dV + \int_{\Omega_0} \frac{\partial \mathcal{W}^{(lce)}}{\partial \boldsymbol{n}} \cdot \delta \boldsymbol{n} \, dV = 0,$$

or equivalently,

$$\delta_n \Pi = \int_{\Omega_0} \boldsymbol{\pi}_0 : \text{Grad}\, \delta \boldsymbol{n} \, dV - \int_{\Omega_0} \boldsymbol{g}_n \cdot \delta \boldsymbol{n} \, dV = 0. \tag{5.19}$$

We note that the equations (5.18) and (5.19) obtained is equivalent to the principle of virtual work formulation obtained in section 5.2.

Formulation for the nearly incompressible solid material. Previously, we wrote the standard variational form of linear momentum balance equation with the displacement field being the only independent variable. While this formulation may work for some problems, it may not be best suited for the

problem where constraints are imposed on the deformation of the body. The LCE material we consider exhibit nearly incompressible property with Poisson's ratio $\upsilon > 0.45$. This imposes the restriction that the value of J should be nearly equal to 1. In the FE treatment of this problem associated with the constraint condition, erroneous solutions as well as numerical problems due to locking should be expected within the context of a displacement-based variational formulation in which only the displacement field is discretized [75]. Within the scope of incompressible or nearly incompressible materials, the volumetric locking leads to the effect that computed displacement fields are much lower in value than expected. For the detailed study of the locking phenomenon, one can refer to [91].

Mixed variational formulation represents the suitable approach to eliminate the numerical difficulties arisen from displacement-based variational formulation. The failure of displacement-based formulation within the context of a nearly incompressible material lies in the determination of pressure p which is related to the volumetric part of the strain [88]. On that account, mixed variational method separates the pressure from the total stress field and treats this as an independent variable. In the mixed variational formulation presented in this work (see [92] and [93]), besides the displacement field $\boldsymbol{u}$ and pressure field p, a third kinetic field variable, namely the dilation $\tilde{J}$, is treated and discretized independently. Using the additive split of the strain-energy function into volumetric and deviatoric parts [94], we obtain

$$\mathcal{W}^{(lce)}(\boldsymbol{F}, \boldsymbol{F}_v, \boldsymbol{A}_v, \boldsymbol{n}) = \mathcal{W}^{(lce)}_{vol}(\tilde{J}) + \mathcal{W}^{(lce)}_{dev}(\tilde{\boldsymbol{F}}, \boldsymbol{F}_v, \boldsymbol{A}_v, \boldsymbol{n}), \tag{5.20}$$

where $\tilde{\boldsymbol{F}} = J^{-\frac{1}{3}}\boldsymbol{F}$. We assume that the volumetric response of the material remains fully elastic, and the viscous response is caused by deviatoric deformation. The deviatoric part of the strain-energy function is dependent of $\tilde{\boldsymbol{F}}, \boldsymbol{n}$,

and internal variables $\boldsymbol{F}_v$ and $\boldsymbol{A}_v$. The three-field energy functional is defined as follows

$$\Pi_u\left(\boldsymbol{u}, p, \tilde{J}\right) = \int_{\Omega_0} \left[\mathcal{W}_{dev}^{(lce)}\left(\tilde{\boldsymbol{F}}(\boldsymbol{u}), \boldsymbol{F}_v, \boldsymbol{A}_v, \boldsymbol{n}\right) + W_{vol}^{(lce)}\left(\tilde{J}\right) + p\left(J - \tilde{J}\right)\right] dV. \quad (5.21)$$

The stationary value of the functional Π_u can be computed by equating to zero the variations of $\boldsymbol{u}$ with respect to three fields $\left(\boldsymbol{u}, p, \tilde{J}\right)$ using the Hu-Washizu variational principle [94]. The resulting equations, by the principle of stationary potential energy, give the variational form and the constitutive and kinematic relationship associated with the volumetric behaviour. We therefore obtain,

$$\delta_u \Pi_u = \int_{\Omega_0} \frac{\partial \mathcal{W}_{dev}^{(lce)}}{\partial \boldsymbol{F}} : \delta \boldsymbol{F}\, dV + \int_{\Omega_0} p\, \delta J\, dV = 0, \quad (5.22)$$

$$\delta_p \Pi_u = \int_{\Omega_0} \left(J - \tilde{J}\right) \delta p\, dV = 0, \quad (5.23)$$

$$\delta_{\tilde{J}} \Pi_u = \int_{\Omega_0} \left(\frac{\partial \mathcal{W}_{vol}^{(lce)}}{\partial \tilde{J}} - p\right) \delta \tilde{J}\, dV = 0. \quad (5.24)$$

The volumetric locking still emerges if the dilation $\tilde{J}$, pressure p and displacement field $\boldsymbol{u}$ are discretized based on the same interpolation function. Generally, interpolation function for $\tilde{J}$ and p are chosen to be one order less than the interpolation function for the displacement field. Since we would use linear interpolation function for the displacement field, $\tilde{J}$ and p are interpolated by a constant interpolation function over a given volume. This procedure know as *the mean dilation method* [95].

After interpolation, p, $\tilde{J}$, δp and $\delta\tilde{J}$ are constant over the integration volume. This causes (5.23) to become

$$\tilde{J} = \frac{1}{V}\int_{\Omega_0} J\, dV = \frac{v}{V}, \tag{5.25}$$

and (5.24) to become

$$p = \frac{\partial \mathcal{W}_{vol}^{(lce)}}{\partial \tilde{J}}. \tag{5.26}$$

Equation (5.25) shows that $\tilde{J} = \frac{v}{V}$ is the integral equivalent of pointwise Jacobian $J = \frac{\partial v}{\partial V}$.

One can introduce the volumetric strain-energy function as [95]

$$\mathcal{W}_{vol}^{(lce)}(\tilde{J}) = \frac{1}{2}B\left(\tilde{J}-1\right)^2, \tag{5.27}$$

which makes equation (5.26) equivalent to

$$p = B\frac{v-V}{V}, \tag{5.28}$$

where B is the bulk modulus of the LCE material. Since the variables p and $\tilde{J}$ are constant in the integral volume (element in the FE method), one can eliminate them at the nodal level of numerical calculations [75].

Since p is constant over the volume, (5.22) can be written as

$$\begin{aligned}\delta_u \Pi_u &= \int_{\Omega_0} \frac{\partial \mathcal{W}_{dev}^{(lce)}}{\partial \boldsymbol{F}} : \delta \boldsymbol{F}\, dV + p \int_{\Omega_0} \frac{\partial J}{\partial \boldsymbol{F}} : \delta \boldsymbol{F}\, dV, \\ &= \int_{\Omega_0} \left(\frac{\partial \mathcal{W}_{dev}^{(lce)}}{\partial \boldsymbol{F}} + p \frac{\partial J}{\partial \boldsymbol{F}} \right) : \delta \boldsymbol{F}\, dV, \\ &= \int_{\Omega_0} \boldsymbol{P} : \delta \boldsymbol{F}\, dV, \end{aligned} \tag{5.29}$$

where

$$\boldsymbol{P} = \frac{\partial \mathcal{W}_{dev}^{(lce)}}{\partial \boldsymbol{F}} + p \frac{\partial J}{\partial \boldsymbol{F}} = \frac{\partial \mathcal{W}_{dev}^{(lce)}}{\partial \boldsymbol{F}} + p \boldsymbol{F}^{-T} \tag{5.30}$$

is the first Piola-Kirchoff stress tensor described in terms of the deviatoric strain-energy density $\mathcal{W}_{dev}^{(lce)}$ and pressure field p.

5.4 Linearization of the variational form

The variational forms (5.19) and (5.29) are nonlinear in the displacement field $\boldsymbol{u}$ and director field $\boldsymbol{n}$. In the FE method, the solution is found by solving the system of linear equations by some iterative solution techniques like the Newton-Raphson method. To facilitate this procedure, our nonlinear system of equations must first be linearized. We linearize the weak-form equations (5.19) and (5.29) in the direction of the variable that each equation depends on. We further assume that the external loads are dead loads and independent of the displacement and director field. This assumption makes the linearization of the variational form to be dependent only on the internal

part, i.e.,

$$\delta_u \Pi = \int_{\Omega_0} \boldsymbol{P} : \delta \boldsymbol{F} \, dV, \tag{5.31}$$

$$\delta_n \Pi = \int_{\Omega_0} \boldsymbol{\pi}_0 : \operatorname{Grad} \delta \boldsymbol{n} \, dV - \int_{\Omega_0} \boldsymbol{g}_n \cdot \delta \boldsymbol{n} \, dV. \tag{5.32}$$

Linearizing the above equations 5.31 and 5.32 with respect to the displacement field $\boldsymbol{u}$ gives

$$\Delta_u \delta_u \Pi = \int_{\Omega_0} \delta \boldsymbol{F} : \Delta_u \boldsymbol{P} \, dV, \tag{5.33}$$

$$\Delta_u \delta_n \Pi = \int_{\Omega_0} \operatorname{Grad} \delta \boldsymbol{n} : \frac{d \boldsymbol{\pi}_0}{d \boldsymbol{F}} : \Delta \boldsymbol{F} \, dV - \int_{\Omega_0} \delta \boldsymbol{n} \cdot \frac{d \boldsymbol{g}_n}{d \boldsymbol{F}} : \Delta \boldsymbol{F} \, dV, \tag{5.34}$$

where $\Delta_u(\bullet)$ is the linearization operator which gives linearization of a function in the direction of $\boldsymbol{u}$.

Similarly, linearization of equations 5.31 and 5.32 with respect to the director field $\boldsymbol{n}$ implies

$$\Delta_n \delta_u \Pi = \int_{\Omega_0} \delta \boldsymbol{F} : \frac{d \boldsymbol{P}}{d \boldsymbol{n}} \cdot \Delta \boldsymbol{n} \, dV, \tag{5.35}$$

$$\Delta_n \delta_n \Pi = \int_{\Omega_0} \operatorname{Grad} \delta \boldsymbol{n} : \frac{d \boldsymbol{\pi}_0}{d \operatorname{Grad} \boldsymbol{n}} \cdot \operatorname{Grad} \Delta \boldsymbol{n} \, dV - \int_{\Omega_0} \delta \boldsymbol{n} \cdot \frac{d \boldsymbol{g}_n}{d \boldsymbol{n}} \cdot \Delta \boldsymbol{n} \, dV. \tag{5.36}$$

Equation (5.33) requires the linearization of the stress tensor $\boldsymbol{P}$ with respect to $\boldsymbol{u}$. This stress tensor is dependent upon the deformation gradient $\boldsymbol{F}$ and pressure field p, and all are ultimately dependent on the displacement field $\boldsymbol{u}$.

The linearization of the stress field 5.30 is

$$\Delta_u \boldsymbol{P} = \frac{d\boldsymbol{P}}{d\boldsymbol{F}} : \Delta\boldsymbol{F} + \frac{\partial J}{\partial \boldsymbol{F}}\Delta p. \tag{5.37}$$

The pressure p, using (5.26) and (5.27), is equal to

$$p = \frac{\partial \mathcal{W}_{vol}^{(lce)}}{\partial \tilde{J}} = B\left(\tilde{J} - 1\right), \tag{5.38}$$

and its linearization is

$$\Delta p = B\Delta\tilde{J} = \frac{B}{V}\int_{\Omega_0} \Delta J \, dV. \tag{5.39}$$

Since Δp needs to be constant within the integral volume, (5.33) takes the form

$$\Delta_u \delta_u \Pi = \int_{\Omega_0} \delta\boldsymbol{F} : \frac{d\boldsymbol{P}}{d\boldsymbol{F}} : \Delta\boldsymbol{F} \, dV + \frac{B}{V}\int_{\Omega_0} \delta\boldsymbol{F} : \frac{\partial J}{\partial \boldsymbol{F}} \, dV \int_{\Omega_0} \frac{\partial J}{\partial \boldsymbol{F}} : \Delta\boldsymbol{F} \, dV. \tag{5.40}$$

5.5 Discretization

In a standard FE procedure [94], the domain Ω_0 is divided into n_e number of subdomain Ω_e called *finite elements*. The continuous assembly of these elements make a domain Ω_0^h which approximates the original domain Ω_0 as

$$\Omega_0 \approx \bigcup_{e=1}^{n_e} \Omega_e = \Omega_0^h. \tag{5.41}$$

The typical shape of a three-dimensioned (3D) finite element is a tetrahedron or a hexahedron (see figure 5.1).

The independent variables are calculated only at the nodes of these finite

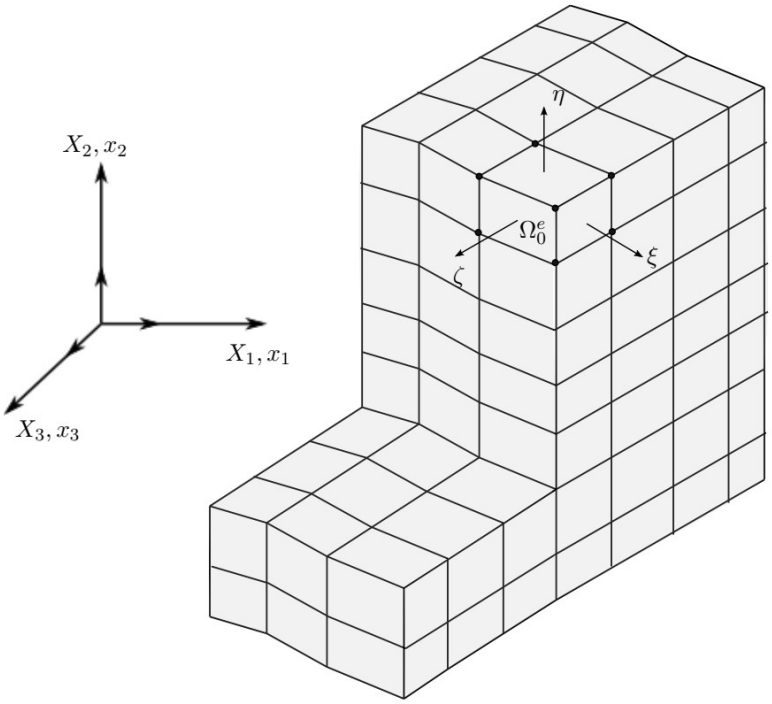


FIGURE 5.1: Division of domain into 8-node hexahedron finite elements.

elements by solving the weak form numerically. The value at other points of the element are interpolated using the nodal values by suitable interpolation function (also called shape function).

If φ denotes the independent variable, the value of the variable at point $\boldsymbol{X}$ is approximated as

$$\varphi(\boldsymbol{X}) = \sum_{i=1}^{n} N_i(\boldsymbol{X})\,\varphi_i, \tag{5.42}$$

where n is the total number of nodes in an element, $N_i(\boldsymbol{X})$ is the shape function at point $\boldsymbol{X}$ associated with the ith node, and φ_i is the value of the variable at node i.

5.5.1 Concept of isoparametric element

In general, finite elements used to divide a domain can be of different complex shapes. The formulation of the shape function for these complex geometric elements is not always simple. To facilitate this, one can use the concept of a parametric element. The parametric element is a simple shape element in the parametric space which can be easily mapped on the reference configuration by means of geometric transformation. The idea is to use the same parametric element for every real element, but the transformation is different for each element since it is defined by the position of the nodes of the actual element [94].

Figure 5.2 shows the mapping of the parametric element $\Omega^e_\square$ from the parametric space $\Omega_\square$ with coordinate system $\boldsymbol{\xi}(\xi, \eta, \zeta)$ into the reference configuration Ω^e_0 and current configuration Ω^e. The parametric element is a cube where the local coordinate spans from -1 to 1 in each direction. The origin of the coordinate system ($\xi = 0, \eta = 0, \zeta = 0$) lies internally at the geometric centre of the cube.

The mapping between the parametric space and reference configuration is described by the Jacobian $\boldsymbol{J}_e$ given as

$$\boldsymbol{J}_e = \frac{\partial \boldsymbol{X}}{\partial \boldsymbol{\xi}} = \begin{bmatrix} \dfrac{\partial X_1}{\partial \xi} & \dfrac{\partial X_2}{\partial \xi} & \dfrac{\partial X_3}{\partial \xi} \\ \dfrac{\partial X_1}{\partial \eta} & \dfrac{\partial X_2}{\partial \eta} & \dfrac{\partial X_3}{\partial \eta} \\ \dfrac{\partial X_1}{\partial \zeta} & \dfrac{\partial X_2}{\partial \zeta} & \dfrac{\partial X_3}{\partial \zeta} \end{bmatrix}. \tag{5.43}$$

Similarly, the mapping onto the current configuration is described by the Jacobian $\boldsymbol{j}_e = \dfrac{\partial \boldsymbol{x}}{\partial \boldsymbol{\xi}}$.

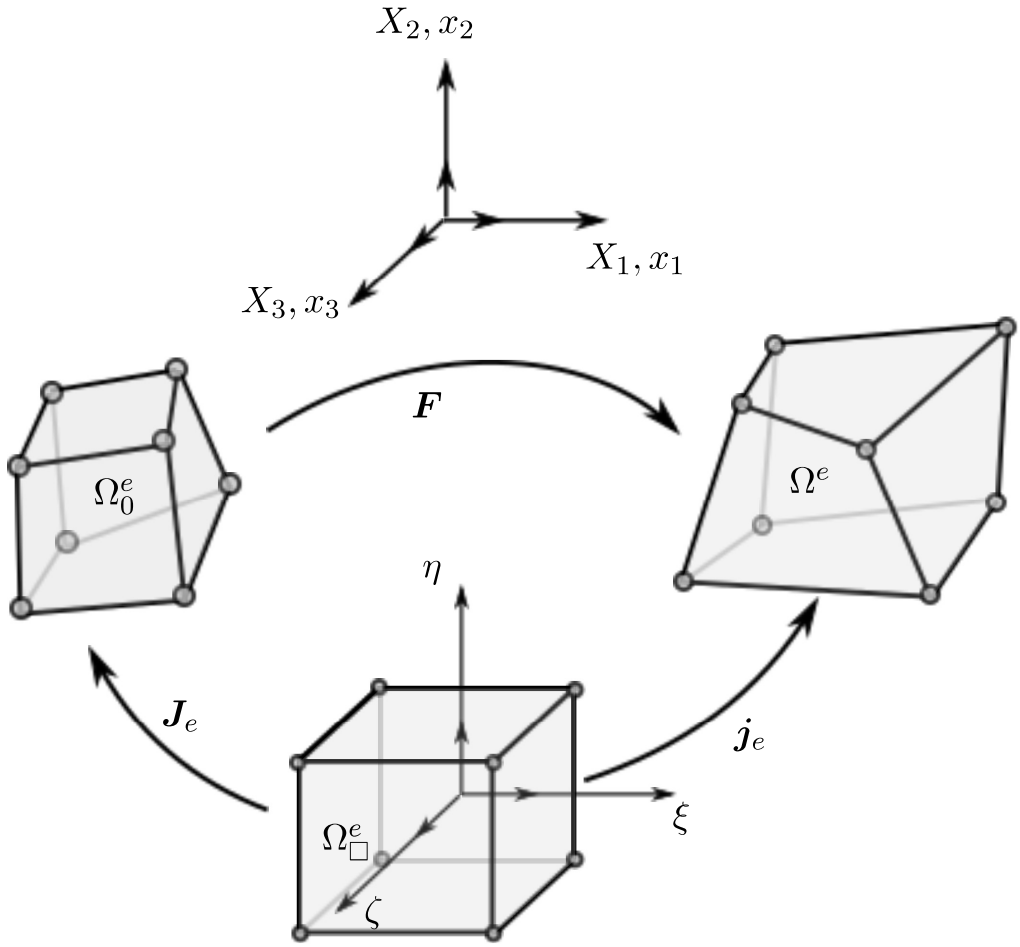


FIGURE 5.2: Isoparametric mapping of a parametric element $\Omega_\square^e$ with coordinate system $\boldsymbol{\xi}(\xi, \eta, \zeta)$ into the reference configuration Ω_0 and current configuration Ω.

In this work, we will use the 8-node hexahedral element and all further discussion will be based on this element. The actual element in the reference or current configuration can be of any 8-node hexahedral shape, but the parametric element is a cube with unit side length. The origin of the coordinate system is located at the centre of this parametric element.

The variable φ in (5.42) can now be interpolated within the parametric element as

$$\varphi(\boldsymbol{\xi}) = \sum_{i=1}^{n} N_i(\boldsymbol{\xi})\varphi_i. \tag{5.44}$$

Within the isoparametric element formulation, the same shape function $N_a(\boldsymbol{\xi})$ is used to obtain the position $\boldsymbol{X}$ of any particle on the actual element of the reference configuration from the position $\boldsymbol{\xi}$ of the corresponding particle in the parametric element. The transformation is

$$\boldsymbol{X}(\boldsymbol{\xi}) = \sum_{i=1}^{n} N_i(\boldsymbol{\xi}) \boldsymbol{X}_i. \tag{5.45}$$

The shape function $N_i(\boldsymbol{\xi})$ is usually a polynomial of value 1 at the node i and 0 at the other nodes. Also, at any point on an element, the sum of the values of all shape functions is equal to one. In this work, we will use the trilinear shape function for the 8-node hexahedral element given by

$$N_i(\boldsymbol{\xi}) = \frac{1}{8}(1 + \xi_i\xi)(1 + \eta_i\eta)(1 + \zeta_i\zeta). \tag{5.46}$$

Note that we had introduced two extra variables, namely, the pressure p and dilation $\tilde{J}$ to circumvent the numerical instabilities due to incompressibility constraints. As already discussed in section 5.3, the variables p and $\tilde{J}$ are interpolated by constant functions, which makes these variables constant over the entire element. Thus, in the mixed formulation, the displacement and nematic director fields are described by trilinear polynomial shape functions, while the pressure and dilation fields are described by constant functions. A mixed element with the shape function of order one for displacement and director, and zero for pressure is designated as a Q1P0 (see figure 5.3) element [94].

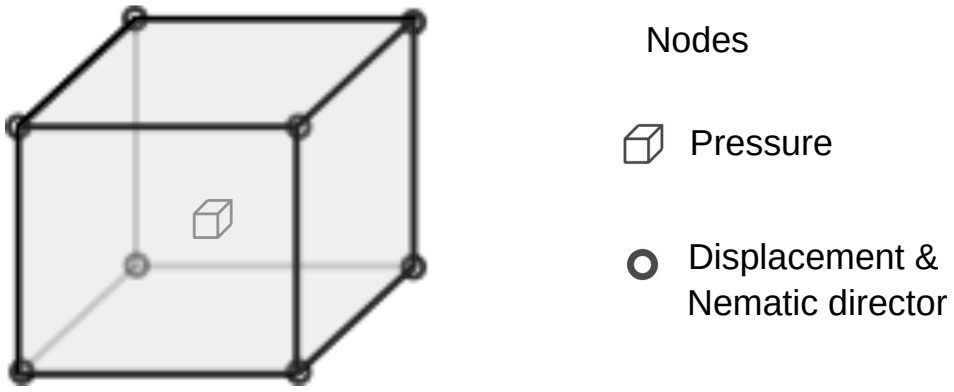


FIGURE 5.3: Q1P0 element showing pressure, displacement, and nematic director nodes.

5.5.2 Discretization of kinematic quantities

As aforementioned in section 5.5.1, the discretization of the geometry in the reference configuration for the 8-nodehexahedral element is given by

$$\boldsymbol{X} = \sum_{i=1}^{8} N_i \boldsymbol{X}_i. \tag{5.47}$$

It will be wise to represent the quantities in matrix form for ease of implementation into code. Then

$$\boldsymbol{X} = \sum_{i=1}^{8} \boldsymbol{N}_{ui} \boldsymbol{X}_{ei}^{T}, \tag{5.48}$$

where

$$\boldsymbol{X}_{ei} = \begin{bmatrix} X_1^i & X_1^i & X_1^i \end{bmatrix} \tag{5.49}$$

and

$$\boldsymbol{N}_{ui} = \begin{bmatrix} N_i & 0 & 0 \\ 0 & N_i & 0 \\ 0 & 0 & N_i \end{bmatrix}. \tag{5.50}$$

The product of $\boldsymbol{N}_{ui}$ and $\boldsymbol{X}_{ei}$ needs to be summed over each element to find the $\boldsymbol{X}$. To have a single matrix operation to interpolate $\boldsymbol{X}$, we can write

$$\boldsymbol{X} = \boldsymbol{N}_u \boldsymbol{X}_e^T, \tag{5.51}$$

where $\boldsymbol{N}_u$ and $\boldsymbol{X}_e$ are formed by the column-wise combination of $\boldsymbol{N}_{ui}$ and $\boldsymbol{X}_{ei}$, respectively, as follows

$$\boldsymbol{N}_u = \begin{bmatrix} \boldsymbol{N}_{u1} & \boldsymbol{N}_{u2} & \boldsymbol{N}_{u3} & \boldsymbol{N}_{u4} & \boldsymbol{N}_{u5} & \boldsymbol{N}_{u6} & \boldsymbol{N}_{u7} & \boldsymbol{N}_{u8} \end{bmatrix}, \tag{5.52}$$

$$\boldsymbol{X}_e = \begin{bmatrix} \boldsymbol{X}_{e1} & \boldsymbol{X}_{e2} & \boldsymbol{X}_{e3} & \boldsymbol{X}_{e4} & \boldsymbol{X}_{e5} & \boldsymbol{X}_{e6} & \boldsymbol{X}_{e7} & \boldsymbol{X}_{e8} \end{bmatrix}. \tag{5.53}$$

Here $\boldsymbol{X}_e$ contains the coordinates of all the nodes of an element in a single row matrix. It is not always possible to discretize all the quantities in a single matrix operation. Some discretization should still be in the summation form, but the single operation is adopted wherever possible.

The independent variables $\boldsymbol{u}$ and $\boldsymbol{n}$ are discretized as

$$\boldsymbol{u} = \boldsymbol{N}_u \boldsymbol{u}_e^T, \tag{5.54}$$

$$\boldsymbol{n} = \boldsymbol{N}_n \boldsymbol{n}_e^T, \tag{5.55}$$

where

$$\boldsymbol{u}_e = \begin{bmatrix} \boldsymbol{u}_{e1} & \boldsymbol{u}_{e2} & \boldsymbol{u}_{e3} & \boldsymbol{u}_{e4} & \boldsymbol{u}_{e5} & \boldsymbol{u}_{e6} & \boldsymbol{u}_{e7} & \boldsymbol{u}_{e8} \end{bmatrix}, \tag{5.56}$$

$$\boldsymbol{u}_{ei} = \begin{bmatrix} u_1^i & u_2^i & u_3^i \end{bmatrix}, \tag{5.57}$$

$$\boldsymbol{n}_e = \begin{bmatrix} \boldsymbol{n}_{e1} & \boldsymbol{n}_{e2} & \boldsymbol{n}_{e3} & \boldsymbol{n}_{e4} & \boldsymbol{n}_{e5} & \boldsymbol{n}_{e6} & \boldsymbol{n}_{e7} & \boldsymbol{n}_{e8} \end{bmatrix}, \tag{5.58}$$

$$\boldsymbol{n}_{ei} = \begin{bmatrix} , n_1^i & n_2^i & n_3^i \end{bmatrix}, \tag{5.59}$$

with $\boldsymbol{N}_n$ the shape function for the director field. Since the director field is a vector quantity similar to the displacement, $\boldsymbol{N}_n$ is same as $\boldsymbol{N}_u$.

In a similar fashion, the increment and virtual forms of the variables are interpolated as

$$\delta \boldsymbol{u} = \boldsymbol{N}_u \delta \boldsymbol{u}_e^T, \qquad \delta \boldsymbol{n} = \boldsymbol{N}_n \delta \boldsymbol{n}_e^T, \tag{5.60}$$

$$\Delta \boldsymbol{u} = \boldsymbol{N}_u \Delta \boldsymbol{u}_e^T, \qquad \Delta \boldsymbol{n} = \boldsymbol{N}_n \Delta \boldsymbol{n}_e^T. \tag{5.61}$$

For the interpolation of $\delta \boldsymbol{F}$, it is convenient to write the matrix in Voigt notation [95]

$$\delta \hat{\boldsymbol{F}} = \begin{bmatrix} \delta \boldsymbol{F}_{11} \\ \delta \boldsymbol{F}_{22} \\ \delta \boldsymbol{F}_{33} \\ \delta \boldsymbol{F}_{12} \\ \delta \boldsymbol{F}_{23} \\ \delta \boldsymbol{F}_{13} \\ \delta \boldsymbol{F}_{21} \\ \delta \boldsymbol{F}_{32} \\ \delta \boldsymbol{F}_{31} \end{bmatrix}. \tag{5.62}$$

The interpolation is obtained as

$$\delta \hat{\boldsymbol{F}} = \sum_{i=1}^{8} \boldsymbol{B}_{ui} \delta \boldsymbol{u}_{ei}^T, \tag{5.63}$$

where $\boldsymbol{B}_{ui}$ is equal to [94]

$$\boldsymbol{B}_{ui} = \begin{bmatrix} N_{i,1} & 0 & 0 \\ 0 & N_{i,2} & 0 \\ 0 & 0 & N_{i,3} \\ N_{i,2} & 0 & 0 \\ 0 & N_{i,3} & 0 \\ N_{i,3} & 0 & 0 \\ 0 & N_{i,1} & 0 \\ 0 & 0 & N_{i,1} \\ 0 & 0 & N_{i,1} \end{bmatrix}. \tag{5.64}$$

Here, $N_{i,1}$ denotes the derivative of N_i with respect to X_1, and similarly for the other indices.

The above interpolation of $\delta\hat{\boldsymbol{F}}$ contains the summation over all nodes. We can formulate these in a single operation using the matrix $\boldsymbol{B}_u$ of size 9×24 formed by appending $\boldsymbol{B}_{ui}$ column-wise, i.e.,

$$\delta\hat{\boldsymbol{F}} = \boldsymbol{B}_u \delta\boldsymbol{u}_e^T, \tag{5.65}$$

where

$$\boldsymbol{B}_u = \begin{bmatrix} \boldsymbol{B}_{u1} & \boldsymbol{B}_{u2} & \boldsymbol{B}_{u3} & \boldsymbol{B}_{u4} & \boldsymbol{B}_{u5} & \boldsymbol{B}_{u6} & \boldsymbol{B}_{u7} & \boldsymbol{B}_{u8} \end{bmatrix}. \tag{5.66}$$

Similarly, Grad $\delta\boldsymbol{n}$ in Voigt notation is $\widehat{\text{Grad}}\,\delta\boldsymbol{n}$ and is interpolated as

$$\widehat{\text{Grad}}\,\delta\boldsymbol{n} = \sum_{i=1}^{8} \boldsymbol{B}_{ni} \delta\boldsymbol{n}_{ei}^T, \tag{5.67}$$

where $\boldsymbol{B}_{ni}$ and $\boldsymbol{B}_n$ are similar to $\boldsymbol{B}_{ui}$ and $\boldsymbol{B}_u$. Thus, $\widehat{\text{Grad}}\delta\boldsymbol{n}$ is interpolated as

$$\widehat{\text{Grad}}\,\delta\boldsymbol{n} = \boldsymbol{B}_n \delta\boldsymbol{n}_e^T. \tag{5.68}$$

By analogy, interpolation of $\Delta\bar{\boldsymbol{F}}$ is $\boldsymbol{B}_u \Delta\boldsymbol{u}_e^T$ and that of $\widehat{\text{Grad}}\,\Delta\boldsymbol{n}$ is $\boldsymbol{B}_n \Delta\boldsymbol{n}_e^T$.

5.5.3 Discretization of variational formulation

With the purpose of obtaining a discretized variational form, we recall the equations (5.29) and (5.19). Since we have introduced the FE concept, it is reasonable to work on the contribution done by integral volume of the single element Ω_e. For the single element, we have the variational formulation

$$\delta_u \Pi^e = \int_{\Omega_0^e} \boldsymbol{P} : \delta\boldsymbol{F}\, dV^e, \tag{5.69}$$

$$\delta_n \Pi^e = \int_{\Omega_0^e} \boldsymbol{\pi}_0 : \text{Grad}\,\delta\boldsymbol{n}\, dV^e - \int_{\Omega_0} \boldsymbol{g}_n \cdot \delta\boldsymbol{n}\, dV^e. \tag{5.70}$$

In matrix form, the above equations become, respectively,

$$\delta_u \Pi^e = \int_{\Omega_0^e} \delta\hat{\boldsymbol{F}}^T \hat{\boldsymbol{P}}\, dV^e, \tag{5.71}$$

$$\delta_n \Pi^e = \int_{\Omega_0^e} \text{Grad}^T\, \delta\boldsymbol{n}\, \hat{\boldsymbol{\pi}}_0\, dV^e - \int_{\Omega_0} \delta\boldsymbol{n}^T \boldsymbol{g}_n\, dV^e. \tag{5.72}$$

Introducing the interpolation of $\delta\boldsymbol{F}$, $\delta\boldsymbol{u}$, $\delta\boldsymbol{n}$ and $\text{Grad}\,\delta\boldsymbol{n}$, we obtain

$$\delta_u \Pi^e = \int_{\Omega_0^e} \delta \boldsymbol{u}_e \delta \boldsymbol{B}_u^T \hat{\boldsymbol{P}} \, dV^e, \tag{5.73}$$

$$\delta_n \Pi^e = \int_{\Omega_0^e} \delta \boldsymbol{n}_e \boldsymbol{B}_n^T \hat{\boldsymbol{\pi}}_0 \, dV^e - \int_{\Omega_0} \delta \boldsymbol{n}_e \boldsymbol{N}_n^T \boldsymbol{g}_n \, dV^e. \tag{5.74}$$

Noting that the virtual nodal displacement and director vector are independent of integration, taking terms $\delta \boldsymbol{u}_e$ and $\delta \boldsymbol{n}_e$ out of the integration gives

$$\delta_u \Pi^e = \delta \boldsymbol{u}_e \int_{\Omega_0^e} \delta \boldsymbol{B}_u^T \hat{\boldsymbol{P}} \, dV^e, \tag{5.75}$$

$$\delta_n \Pi^e = \delta \boldsymbol{n}_e \left[\int_{\Omega_0^e} \boldsymbol{B}_n^T \hat{\boldsymbol{\pi}}_0 \, dV^e - \int_{\Omega_0} \boldsymbol{N}_n^T \boldsymbol{g}_n \, dV^e \right]. \tag{5.76}$$

The variational form obtained per element can also be expressed in terms of residual nodal forces and fluxes as

$$\delta_u \Pi^e = \delta \boldsymbol{u}_e \boldsymbol{R}_u^e, \tag{5.77}$$

$$\delta_n \Pi^e = \delta \boldsymbol{n}_e \boldsymbol{R}_n^e, \tag{5.78}$$

where

$$\boldsymbol{R}_u^e = \int_{\Omega_0^e} \delta \boldsymbol{B}_u^T \hat{\boldsymbol{P}} \, dV^e, \tag{5.79}$$

$$\boldsymbol{R}_n^e = \int_{\Omega_0^e} \boldsymbol{B}_n^T \hat{\boldsymbol{\pi}}_0 \, dV^e - \int_{\Omega_0} \boldsymbol{N}_n^T \boldsymbol{g}_n \, dV^e. \tag{5.80}$$

Considering that the variational form must be satisfied for any arbitrary virtual nodal displacement and director vector, the residuals $\boldsymbol{R}_u^e$ and $\boldsymbol{R}_n^e$ must be

zero in an equilibrium state.

5.5.4 Discretization of linearized variational formulation

Before proceeding to the discretization of the linearized equations, we review the need for linearizing the variational forms. The linearization is needed to solve the nonlinear set of equations by the iterative Newton-Raphson method or other similar numerical methods. Linearization of the equations gives the tangent matrices which provide the measurement of the increment in the force (or flux) due to the change in position (or director vector) in a system. The linearization of the discretized variational form (5.79) in the direction of $\boldsymbol{u}$ results in

$$\Delta_u \delta_u \Pi^e = \delta \boldsymbol{u}_e \frac{\partial \boldsymbol{R}_u^e}{\partial \boldsymbol{u}} \cdot \Delta \boldsymbol{u} = \delta \boldsymbol{u}_e \boldsymbol{K}_{uu}^e \Delta \boldsymbol{u}_e^T, \tag{5.81}$$

where $\boldsymbol{K}_{uu}^e$ is the tangent matrix that gives the change in forces at the nodes of an element due to changes in the position of nodes of that element. In the Newton-Raphson method, the tangent matrix is an operator that helps in adjusting the nodal positions (or director) so that the internal nodal forces (or fluxes) converge to being in equilibrium with the external nodal forces [95].

Discretization of linearized variational form of linear momentum balance equation. In order to calculate the tangent matrix from (5.40), we first write the equation in matrix form with integration over an element as

$$\Delta_u \delta_u \Pi^e = \int_{\Omega_0^e} \delta \hat{\boldsymbol{F}}^T \frac{d\hat{\boldsymbol{P}}}{d\hat{\boldsymbol{F}}} \Delta \hat{\boldsymbol{F}} \, dV^e + \frac{B}{V} \int_{\Omega_0} \delta \hat{\boldsymbol{F}}^T \frac{\partial J}{\partial \hat{\boldsymbol{F}}} \, dV^e \int_{\Omega_0} \left(\frac{\partial J}{\partial \hat{\boldsymbol{F}}} \right)^T \Delta \hat{\boldsymbol{F}} \, dV^e. \tag{5.82}$$

It will be convenient to discretize the individual terms appearing in the above equation. The first term is the material contribution to the linearized equation

since it contains the material law. Its discretization is

$$\begin{aligned}\Delta_u \delta\Pi^e_{u,mat} &= \int_{\Omega^e_0} \delta \boldsymbol{u}_e \boldsymbol{B}_u^T \frac{d\hat{\boldsymbol{P}}}{d\hat{\boldsymbol{F}}} \boldsymbol{B}_u \Delta \boldsymbol{u}_e^T dV^e, \\ &= \delta \boldsymbol{u}_e \int_{\Omega^e_0} \boldsymbol{B}_u^T \frac{d\hat{\boldsymbol{P}}}{d\hat{\boldsymbol{F}}} \boldsymbol{B}_u dV^e \Delta \boldsymbol{u}_e^T, \\ &= \delta \boldsymbol{u}_e \boldsymbol{K}^e_{uu,mat} \Delta \boldsymbol{u}_e^T. \end{aligned} \tag{5.83}$$

The second term in (5.82) is due to the pressure variable. Interpolating $\delta\hat{\boldsymbol{F}}$ and $\Delta\hat{\boldsymbol{F}}$ yields

$$\begin{aligned}\Delta_u \delta\Pi^e_{u,p} = \delta \boldsymbol{u}_e \frac{B}{V} \int_{\Omega^e_0} \boldsymbol{B}_u^T \frac{\partial J}{\partial \hat{\boldsymbol{F}}} dV^e \int_{\Omega^e_0} \left(\frac{\partial J}{\partial \hat{\boldsymbol{F}}}\right)^T \boldsymbol{B}_u dV^e \Delta \boldsymbol{u}_e^T \\ = \delta \boldsymbol{u}_e \boldsymbol{K}^e_{uu,p} \Delta \boldsymbol{u}_e^T. \end{aligned} \tag{5.84}$$

The total tangent matrix $\boldsymbol{K}^e_{uu}$ is the sum of the two tangent matrices $\boldsymbol{K}^e_{uu,mat}$ and $\boldsymbol{K}^e_{uu,p}$,

$$\boldsymbol{K}^e_{uu} = \boldsymbol{K}^e_{uu,mat} + \boldsymbol{K}^e_{uu,p} \tag{5.85}$$

$$= \int_{\Omega^e_0} \boldsymbol{B}_u^T \frac{d\hat{\boldsymbol{P}}}{d\hat{\boldsymbol{F}}} \boldsymbol{B}_u dV^e + \frac{B}{V} \int_{\Omega^e_0} \boldsymbol{B}_u^T \frac{\partial J}{\partial \hat{\boldsymbol{F}}} dV^e \int_{\Omega^e_0} \left(\frac{\partial J}{\partial \hat{\boldsymbol{F}}}\right)^T \boldsymbol{B}_u dV^e. \tag{5.86}$$

Similarly, the tangent matrix $\boldsymbol{K}^e_{un}$ that describes change in forces due to change in director orientation at the nodes in an element can be obtained through (5.35). Representing the equation in matrix form with integration over an element gives

$$\Delta_n \delta_u \Pi^e = \int_{\Omega^e_0} \delta\hat{\boldsymbol{F}} \frac{d\hat{\boldsymbol{P}}}{d\boldsymbol{n}} \Delta \boldsymbol{n}\, dV^e. \tag{5.87}$$

By interpolating $\delta\hat{\boldsymbol{F}}$ and $\Delta\boldsymbol{n}$, we obtain

$$\begin{aligned}\Delta_n\delta_u\Pi^e &= \delta\boldsymbol{u}_e \int\limits_{\Omega_0^e} \boldsymbol{B}_u^T \frac{d\hat{\boldsymbol{P}}}{d\boldsymbol{n}} \boldsymbol{N}_T dV^e \Delta\boldsymbol{n}_e^T, \\ &= \delta\boldsymbol{u}_e \boldsymbol{K}_{un}^e \Delta\boldsymbol{n}_e^T. \end{aligned} \tag{5.88}$$

Discretization of linearized variational form of director momentum balance equation. Two tangent matrices can be obtained from the linearized variational form of angular balance equations (5.34) and (5.36). These tangent matrices describe the change in torque (fluxes) due to change in the position and director orientation at the nodes of an element. Representing equations (5.34) and (5.36) in matrix form and integrating over an element yields

$$\Delta_u\delta\Pi_n^e = \int\limits_{\Omega_0^e} \mathrm{Grad}^T\, \delta\boldsymbol{n} \frac{d\hat{\boldsymbol{\pi}}_0}{d\hat{\boldsymbol{F}}} \Delta\hat{\boldsymbol{F}}\, dV^e - \int\limits_{\Omega_0^e} \delta\boldsymbol{n} \left(\frac{d\boldsymbol{g}_0}{d\hat{\boldsymbol{F}}}\right)^T \Delta\hat{\boldsymbol{F}}\, dV^e, \tag{5.89}$$

$$\Delta_n\delta\Pi_n^e = \int\limits_{\Omega_0^e} \widehat{\mathrm{Grad}}^T\, \delta\boldsymbol{n} \frac{d\hat{\boldsymbol{\pi}}_0}{d\widehat{\mathrm{Grad}}\,\boldsymbol{n}} \widehat{\mathrm{Grad}}\Delta\boldsymbol{n}\, dV^e - \int\limits_{\Omega_0^e} \delta\boldsymbol{n} \frac{d\boldsymbol{g}_0}{d\boldsymbol{n}} \Delta\boldsymbol{n}\, dV^e. \tag{5.90}$$

By interpolating $\delta\boldsymbol{n}$, $\Delta\boldsymbol{n}$, $\widehat{\mathrm{Grad}}\,\delta\hat{\boldsymbol{n}}$, $\widehat{\mathrm{Grad}}\,\Delta\hat{\boldsymbol{n}}$ and $\Delta\hat{\boldsymbol{F}}$ in the above equations (5.89) and (5.90), we obtain

$$\begin{aligned}\Delta_u\delta\Pi_n^e &= \delta\boldsymbol{n}_e \left[\int\limits_{\Omega_0^e} \boldsymbol{B}_n^T \frac{d\hat{\boldsymbol{\pi}}_0}{d\hat{\boldsymbol{F}}} \boldsymbol{B}_u\, dV^e, - \int\limits_{\Omega_0^e} \boldsymbol{N}_n^T \left(\frac{d\boldsymbol{g}_0}{d\hat{\boldsymbol{F}}}\right)^T \boldsymbol{B}_u\, dV^e\right] \Delta\boldsymbol{u}_e^T \\ &= \delta\boldsymbol{n}_e \boldsymbol{K}_{nu} \Delta\boldsymbol{u}_e^T, \end{aligned} \tag{5.91}$$

$$\begin{aligned}\Delta_n\delta\Pi_n^e &= \delta\boldsymbol{n}_e \left[\int\limits_{\Omega_0^e} \boldsymbol{B}_n^T \frac{d\hat{\boldsymbol{\pi}}_0}{d\widehat{\mathrm{Grad}}\,\boldsymbol{n}} \boldsymbol{B}_n\, dV^e - \int\limits_{\Omega_0^e} \boldsymbol{N}_n^T \frac{d\boldsymbol{g}_0}{d\boldsymbol{n}} \boldsymbol{N}_n\, dV^e\right] \Delta\boldsymbol{n}_e^T, \\ &= \delta\boldsymbol{n}_e \boldsymbol{K}_{nn} \Delta\boldsymbol{n}_e^T. \end{aligned} \tag{5.92}$$

We have finally obtained all the tangent matrices for an element. They are summarized below as

$$
\begin{aligned}
\boldsymbol{K}^e_{uu} &= \int_{\Omega^e_0} \boldsymbol{B}_u^T \frac{d\hat{\boldsymbol{P}}}{d\hat{\boldsymbol{F}}} \boldsymbol{B}_u dV^e + \frac{B}{V} \int_{\Omega^e_0} \boldsymbol{B}_u^T \frac{\partial J}{\partial \hat{\boldsymbol{F}}} dV^e \int_{\Omega^e_0} \left(\frac{\partial J}{\partial \hat{\boldsymbol{F}}} \right)^T \boldsymbol{B}_u dV^e, \\
\boldsymbol{K}^e_{un} &= \delta \boldsymbol{u}_e \int_{\Omega^e_0} \boldsymbol{B}_u^T \frac{d\hat{\boldsymbol{P}}}{d\boldsymbol{n}} \boldsymbol{N}_n dV^e, \\
\boldsymbol{K}^e_{nu} &= \int_{\Omega^e_0} \boldsymbol{B}_n^T \frac{d\hat{\boldsymbol{\pi}}_0}{d\hat{\boldsymbol{F}}} \boldsymbol{B}_u \, dV^e - \int_{\Omega^e_0} \boldsymbol{N}_n^T \left(\frac{d\boldsymbol{g}_0}{d\hat{\boldsymbol{F}}} \right)^T \boldsymbol{B}_u \, dV^e, \\
\boldsymbol{K}^e_{nn} &= \int_{\Omega^e_0} \boldsymbol{B}_n^T \frac{d\hat{\boldsymbol{\pi}}_0}{d\widehat{\mathrm{Grad}\, \boldsymbol{n}}} \boldsymbol{B}_n \, dV^e - \int_{\Omega^e_0} \boldsymbol{N}_n^T \frac{d\boldsymbol{g}_0}{d\boldsymbol{n}} \boldsymbol{N}_n \, dV^e.
\end{aligned}
$$

Note that there is another constraint, namely that the nematic director vector should be a unit vector, $\boldsymbol{n}^T\boldsymbol{n} = 1$. For our problems, it is possible to restrict the rotation of director in the planar domain only. In this case, we can define $\boldsymbol{n} = [\cos\theta, \sin\theta]^T$, such that the unit vector condition is automatically satisfied and the problem is simplified to finding the displacement $\boldsymbol{u}$ and the director angle θ. The strong form of this case in summarized in table 5.1. Then the elemental residual vector and tangent matrices are given as

$$
\begin{aligned}
\boldsymbol{R}^e_u &= \int_{\Omega^e_0} \delta \boldsymbol{B}_u^T \hat{\boldsymbol{P}} \, dV^e, \\
\boldsymbol{R}^e_\theta &= \int_{\Omega^e_0} \boldsymbol{B}_\theta^T \hat{\boldsymbol{\pi}}_\theta \, dV^e - \int_{\Omega_0} \boldsymbol{N}_\theta^T g_\theta \, dV^e, \\
\boldsymbol{K}^e_{uu} &= \int_{\Omega^e_0} \boldsymbol{B}_u^T \frac{d\hat{\boldsymbol{P}}}{d\hat{\boldsymbol{F}}} \boldsymbol{B}_u dV^e + \frac{B}{V} \int_{\Omega^e_0} \boldsymbol{B}_u^T \frac{\partial J}{\partial \hat{\boldsymbol{F}}} dV^e \int_{\Omega^e_0} \left(\frac{\partial J}{\partial \hat{\boldsymbol{F}}} \right)^T \boldsymbol{B}_u dV^e, \\
\boldsymbol{K}^e_{u\theta} &= \delta \boldsymbol{u}_e \int_{\Omega^e_0} \boldsymbol{B}_u^T \frac{d\hat{\boldsymbol{P}}}{d\theta} \boldsymbol{N}_\theta dV^e, \\
\boldsymbol{K}^e_{\theta u} &= \int_{\Omega^e_0} \boldsymbol{B}_\theta^T \frac{d\hat{\boldsymbol{\pi}}_\theta}{d\hat{\boldsymbol{F}}} \boldsymbol{B}_u \, dV^e - \int_{\Omega^e_0} \boldsymbol{N}_\theta^T \left(\frac{dg_\theta}{d\hat{\boldsymbol{F}}} \right)^T \boldsymbol{B}_u \, dV^e,
\end{aligned}
$$

$$\boldsymbol{K}^e_{\theta\theta} = \int_{\Omega^e_0} \boldsymbol{B}^T_\theta \frac{d\hat{\boldsymbol{\pi}}_\theta}{d\,\mathrm{Grad}\,\theta} \boldsymbol{B}_\theta \, dV^e - \int_{\Omega^e_0} \boldsymbol{N}^T_\theta \frac{dg_\theta}{d\theta} \boldsymbol{N}_\theta \, dV^e,$$

where

$$\boldsymbol{\pi}_\theta = \frac{\partial \mathcal{W}^{(3)}}{\partial \mathrm{Grad}\,\theta}\,, \qquad g_\theta = \frac{\partial \mathcal{W}^{(3)}}{\partial \theta}. \tag{5.93}$$

The stresses $\boldsymbol{P}$, $\boldsymbol{\pi}_\theta$ and g_θ, and their derivatives appearing in the tangent matrices are derived for specific free energies shown in appendix A.

TABLE 5.1: Summary of boundary value problem with variables $\boldsymbol{u}$ and θ.

The displacement field $\boldsymbol{u}(\boldsymbol{X}, t)$ and the nematic director angle field $\theta(\boldsymbol{X}, t)$ on the region Ω_0 is determined by the governing equations

$$\mathrm{Div}\,\boldsymbol{P} = 0,$$
$$\mathrm{Div}\,\boldsymbol{\pi}_\theta + g_\theta = 0,$$

with the constitutive equations

$$\boldsymbol{P} = \frac{\partial \mathcal{W}^{(lce)}_{dev}}{\partial \boldsymbol{F}} + p\boldsymbol{F}^{-T},$$
$$\boldsymbol{\pi}_\theta = \frac{\partial \mathcal{W}^{(3)}}{\partial \mathrm{Grad}\,\theta}, \qquad g_\theta = \frac{\partial \mathcal{W}^{(3)}}{\partial \theta},$$

with the initial values

$$\boldsymbol{u}(\boldsymbol{X}, t_0) = \boldsymbol{u}_0, \qquad \theta(\boldsymbol{X}, t_0) = \theta_0,$$

and boundary conditions

$$\boldsymbol{u}(\boldsymbol{X}, t) = \bar{\boldsymbol{u}}, \qquad \boldsymbol{t}_0 = \bar{\boldsymbol{t}}_0(\boldsymbol{X}, t) = \boldsymbol{P}\boldsymbol{N}_0,$$
$$\theta(\boldsymbol{X}, t) = \bar{\theta}, \qquad \boldsymbol{\pi}_\theta \boldsymbol{N}_0 = 0.$$

Global residual vectors and tangent matrices. Thus far, we have obtained the residual vectors and tangent matrices at element level from the discretization of weak form and linearized weak form. The solution of the FE formulation by the iterative process, however, requires the global residuals and tangent matrices. Global residual vectors and tangent matrices are assembled

by adding summation over all the elemental contributions fulfilling the kinematic compatibility. For example, let us take $K^{35}_{TT,23}$, which is the component K_{23} of the tangent matrix $\boldsymbol{K}^{35}_{\theta\theta}$ for element $e = 35$. This component contains the director angle contribution at node 2 by the director angle at node 3 in element 35. However, in global system, nodes 2 and 3 may be shared by the multiple elements. Therefore, contributions from the other elements for this particular nodes 2 and 3 must be accounted for in the global assembly. Symbolically, one can write

$$\boldsymbol{K}_{\theta\theta} = \bigcup_{e=1}^{n_e} \boldsymbol{K}^{e}_{\theta\theta}. \tag{5.94}$$

All the other global tangent matrices and residual vectors will be assembled in a similar manner.

5.6 Discussion

The main novelty and challenges in developing this FE formulation consists in the presence of the nematic director field as an additional independent variable and the coupling between the displacement and director fields. This coupling requires the introduction of additional tangent matrices that describe the change in forces due to change in position at the nodes and vice versa. The implementation of these tangent matrices is crucial for the convergence of the solution in the iterative process. Moreover, the presence of the director field would make the second Piola-Kirchhoff stress (and Cauchy stress) nonsymmetric, which is a departure from the classical elasticity theory as well as the classical FE formulation for elasticity. This requires the modification of the existing open-source FEBio code to accommodate the nonsymmetric stress and the additional tangent matrices. In our case, however, the structure of strain-energy function is such that direct differentiation,

$\boldsymbol{S} = \dfrac{\partial \mathcal{W}}{\partial \boldsymbol{C}}$ is not possible. One must first calculate the first Piola-Kirchhoff stress $\boldsymbol{P} = \dfrac{\partial \mathcal{W}}{\partial \boldsymbol{F}}$ and then do *push-forward* operation to obtain $\boldsymbol{S}$. This extra work does not provide any computational advantage, and thus, we have directly used the first Piola-Kirchhoff stress $\boldsymbol{P}$ in the FE formulation and code implementation.

Chapter 6

Numerical simulations

In this chapter, numerical problems are simulated to examine and discuss various aspects of the material model introduced in chapter 2 for the elastic problem, in chapter 3 for necking and in chapter 4 for the viscoelastic case. For the finite element simulations, the computer implementation was carried out by modifying existing procedures available in the open-source FEBio software [69]. Extensive changes to the FE implementation in FEBio were required to account for additional variables such as nematic director and the order parameter. These changes introduced more nonlinearity to the system as well as increased the cost of the computation.

6.1 Set up of boundary value problem

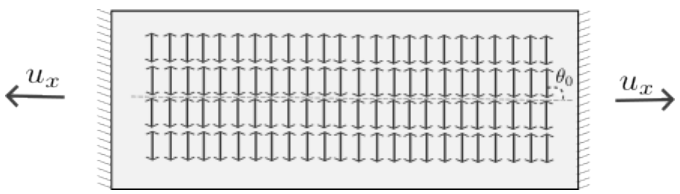


FIGURE 6.1: Boundary conditions for an LCE sample in uniaxial tensile test. The angle θ_0 is between the initial director and stretch direction. The sample is stretched equally at both ends by applying a displacement u_x.

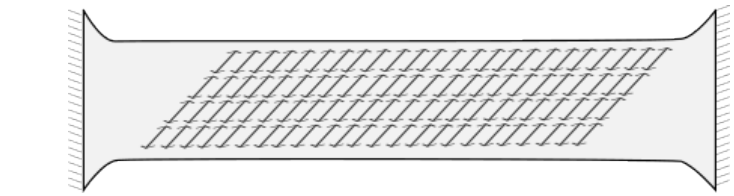
For a uniaxial tensile test, a thin monodomain LCE sample is considered. An exemplary schematic diagram of the setup is shown in figure 6.1. In the elastic case, the model parameters $\mu^{(1)}$, $\mu^{(2)}$, anisotropic parameter a, and Frank constant K were not obtained by fitting any experimental data but were chosen to have similar values to those in the literature [81]. The bulk modulus is taken equal to $B = 1000(\mu^{(1)} + \mu^{(2)})$. For each experiment, the LCE sample has length L, width H and initial director $\boldsymbol{n}_0 = [\cos\theta_0, \sin\theta_0, 0]^T$ as shown in figure 6.1. We perturb the initial angle θ_0 by a small angle of 0.5° in order to obtain the instabilities that we wish to investigate in the LCE sample. All our simulation is for 3-dimensional samples, we restrict the rotation of the director in the main plane only by setting the third component of the director equal to 0. Similarly to the experimental setup, to study the instabilities in an LCE, we fix the displacement and nematic director at the right and left boundary of the specimen, and then stretch equally at both ends (see figure 6.2).

6.2 Simulation of elastic model for an LCE

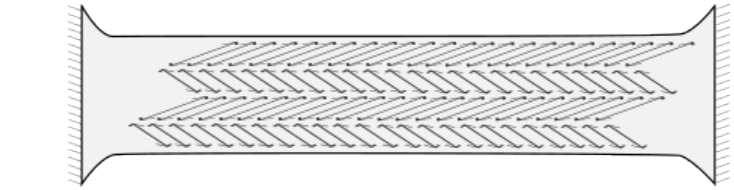
We simulate the elastic model of an LCE sample with the following strain-energy density function introduced in chapter 2:

$$\mathcal{W} = \frac{1}{2}\mu^{(1)}\left(\operatorname{tr}\left(\boldsymbol{F}^T\boldsymbol{F}\right) - 3\right) + \frac{1}{2}\mu^{(2)}\left(\operatorname{tr}\left(\boldsymbol{G}_0^2\boldsymbol{F}^T\boldsymbol{G}^{-2}\boldsymbol{F}\right) - 3\right) + \frac{1}{2}K\,\mathrm{Grad}\,\theta\cdot\mathrm{Grad}\,\theta. \tag{6.1}$$

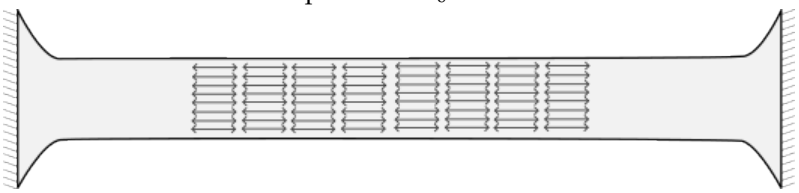
The constitutive model (6.1) is implemented to capture the uniform rotation of the director angle as well as shear striping, depending on the initial director angle θ_0. The uniform rotation (see figure 6.2(a)) is obtained when the initial director angle $\theta_0 < 85^\circ$ in which case there is bias for the LC molecules



(a) Uniform rotation of director angle when $\theta_0 < 85°$.



(b) Alternate rotation of director angle forming shear stripes when $\theta_0 = 90°$.



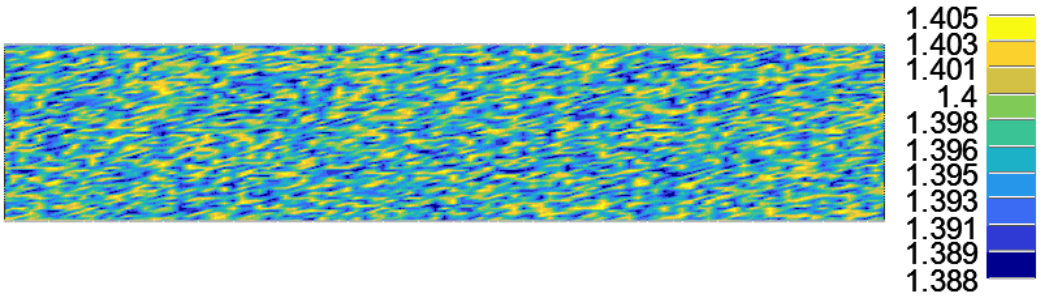
(c) Full rotation of director angle.

FIGURE 6.2: Schematic diagram depicting rotation of the director angle in a stretched LCE sample.

to rotate in the direction of the initial inclination [30]. The LCE sample will present shear striping pattern (see figure 6.2(b)) when the initial director is nearly perpendicular to the stretch direction. Both the uniform rotation for $\theta_0 = 80°$ and parallel stripes pattern for $\theta_0 = 90°$ are simulated. Furthermore, effects on the number of stripes due the geometry (aspect ratio of LCE sample) and frank constant K will be analysed. Similarly, effects of ratio $\frac{\mu^{(1)}}{\mu^{(2)}}$ and anisotropy parameter a on the critical strain at which stripes occur will also be compared with the theoretical values.

6.2.1 Stretching at angle $\theta_0 = 80°$ to initial director

The sample of aspect ratio 5 (length / width = 5/1) is taken for the simulation. The purpose of the investigation is the uniform rotation of the director angle towards the stretching direction and the stress-strain relationship. The



(a) Undeformed, $\lambda = 1$



(b) Deformed, $\lambda = 2$

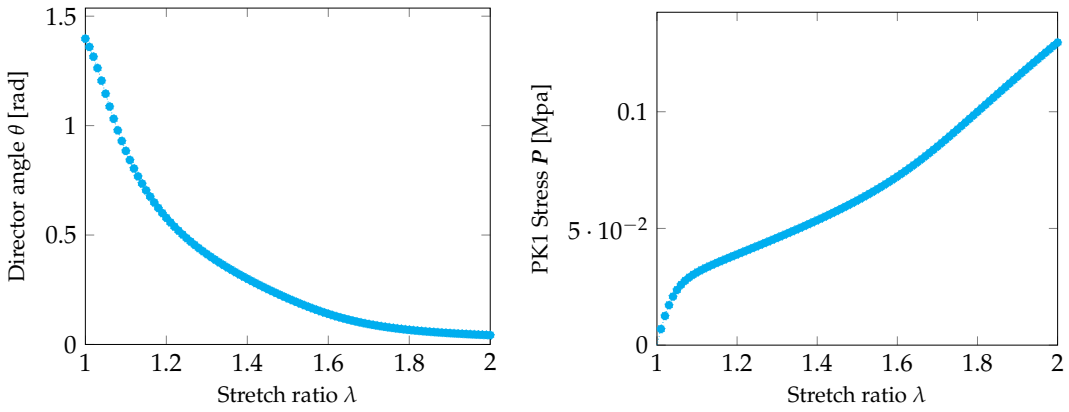
FIGURE 6.3: Director angle θ[rad] of the uniaxial stretch simulation when $\theta_0 = 80^\circ$ at different stretch ratios.

material parameters are listed in Table 6.1.

TABLE 6.1: Material parameters when $\theta_0 = 80^\circ$ leading to uniform director rotation.

parameters	$\mu^{(1)}$	$\mu^{(2)}$	a	K
units	MPa	MPa	-	N
values	3×10^{-1}	1×1^{-1}	5.5	1×10^{-2}

Figure 6.3 shows the director angle in the undeformed state as well as when the sample is stretched by twice its original length. One can see that, after the deformation, all molecules become parallel to the loading direction. One observes in figure 6.4(a) that the angle rotates very fast at the beginning and flattens out towards the end of the stretch. Similarly, the stress rises rapidly at the beginning of the process, then the slope decreases in the middle region of the graph and again rises when the director becomes nearly parallel to the loading direction (see figure 6.4(b)).



(a) Director angle vs stretch ratio.

(b) Nominal stress vs stretch ratio.

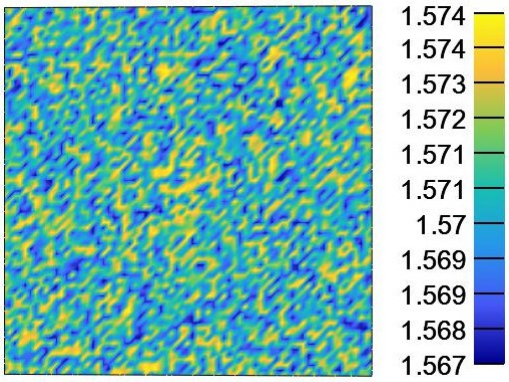
FIGURE 6.4: FE simulation result of uniaxial stretch when $\theta_0 = 80^\circ$ leading to uniform rotation.

6.2.2 Stretching at angle $\theta_0 = 90^\circ$ to initial director

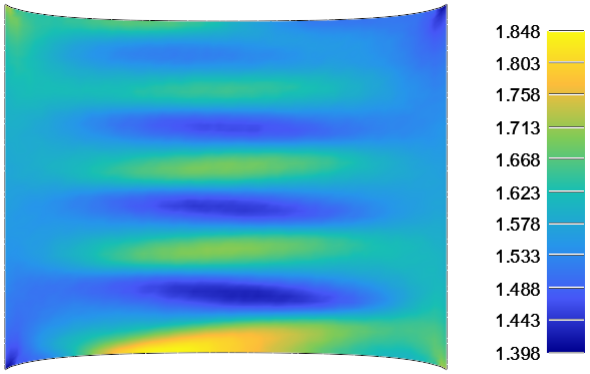
The purpose of this simulation is the investigation of parallel shear stripes due to the alternate rotation of the director angle. We consider a square sample (10mm$\times$10mm) for this study. The initial parameters used are recorded in Table 6.2. Figure 6.5(b) shows the first nucleation of the shear stripes at the critical strain ($\lambda_c = 1.20$). The critical strain is within the range of theoretical predictions (see chapter 2). After the critical strain is nucleated, there is sharp increase in the rate of rotation of director angle (see figure 6.6(a)) in either direction. However, the stress-strain slope is lower than that before the critical strain (see figure 6.6(b)). This shows that the sample has entered into a region of semi-soft elasticity.

TABLE 6.2: Material parameters when $\theta_0 = 90^\circ$ leading to alternate shear stripes.

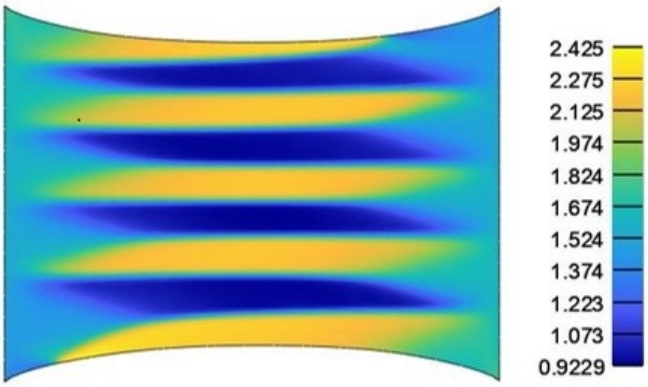
parameters	$\mu^{(1)}$	$\mu^{(2)}$	a	K
units	MPa	MPa	-	N
values	5×10^{-1}	5×10^{-1}	5.5	1×10^{2}



(a) Undeformed, $\lambda = 1$



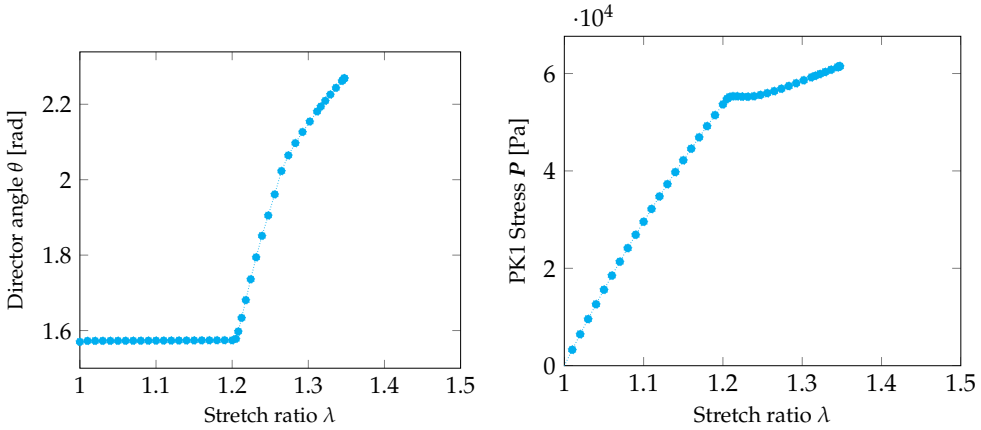
(b) Nucleation of shear domains, $\lambda = \lambda_c = 1.208$



(c) Shear domains, $\lambda = 1.3223$

FIGURE 6.5: Director angle θ[rad] in the uniaxial stretch simulation when $\theta_0 = 90$ at different stretch ratios.

Effects of Frank constant and length of the sample on the width of shear stripes. Rotation of the director vector in nematic LCE requires an energy



(a) Director angle vs strain.

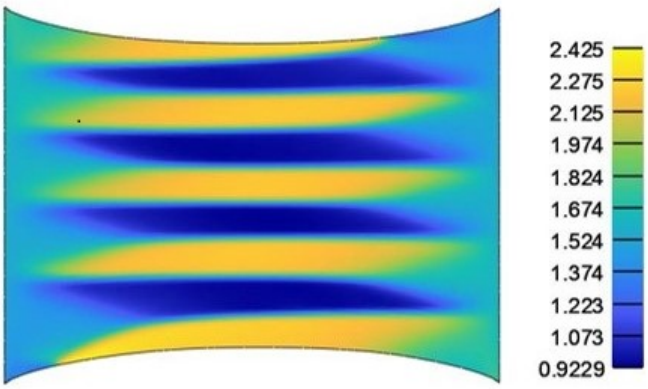
(b) Nominal stress vs strain.

FIGURE 6.6: FE simulation result of uniaxial stretch when $\theta_0 = 90^\circ$ leading to alternate shear stripes.

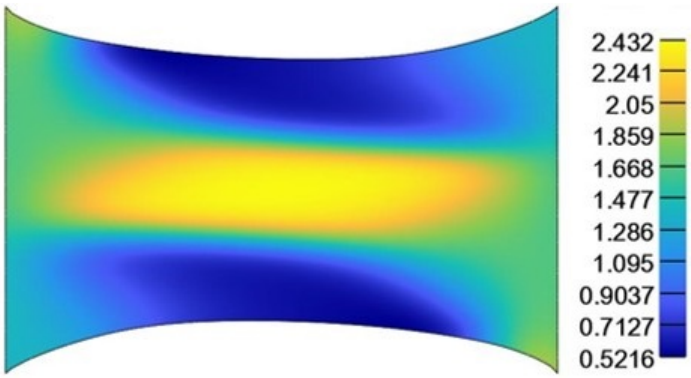
expenditure known as Frank energy [1]. Therefore, the values of Frank constant would affect the response of deformation in LCEs. A nematic penetration depth $\xi \approx \left(K/\mu\right)^{1/2}$ is the characteristic size for the director distortion to be confined in the nematic LCE. The width of the shear stripes are proportional to the penetration depth and length of the sample as $h \approx (L\xi)^{1/2}$ [1]. Therefore, the width of the stripes h increases as the penetration depth ratio ξ increases, and also when the initial length L of the undeformed sample increases.

Figure 6.7 shows the shear stripes for different values of Frank constant K while other parameter remains as listed in table 6.2. One can observe the decrease in the number of stripes and increase in their width when the value of the Frank constant increases. When the Frank constant increases by 100 times (compare figure 6.7(a) and 6.7(b)), the number of stripes decreases by a third. One can reason that the width of the stripes is also increased by a third.

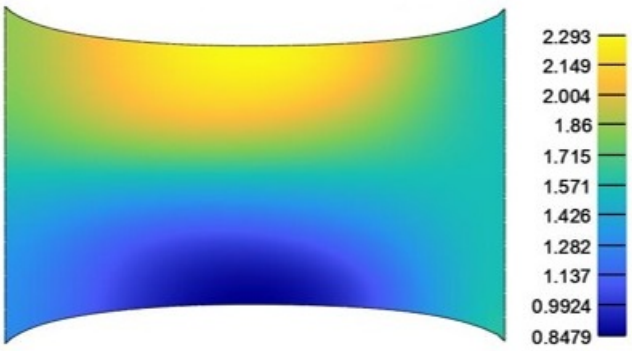
Similarly, when the length of the sample is changed keeping the width constant and all the material parameters as in Table 6.2, there is also a change in the number of shear stripes. Figure 6.8 shows that the number of stripes is



(a) $K = 1 \times 10^2$



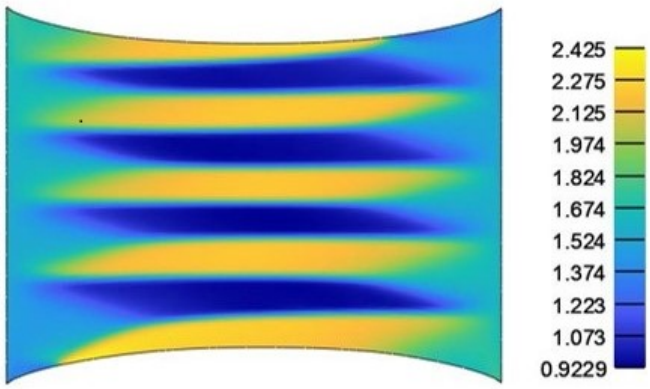
(b) $K = 1 \times 10^4$



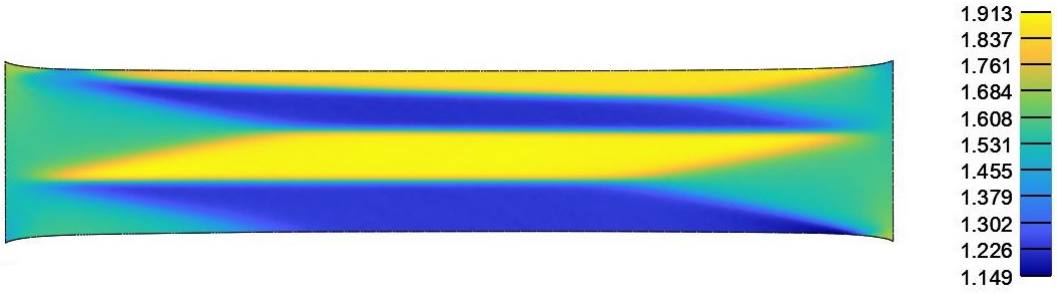
(c) $K = 1 \times 10^5$

FIGURE 6.7: Width and number of shear stripes at different values of the Frank constant K. The index shows the director angle θ in radian.

nearly halved when the length is quadrupled. These simulation results are in line with the theory in chapter 3.



(a) Initial aspect ratio 1 (10×10 undeformed sample)



(b) Initial aspect ratio 4 (40×10 undeformed sample)

FIGURE 6.8: Width and number of shear stripes at different lengths of the undeformed LCE sample. The index shows the director angle θ in radian.

6.3 Simulation of necking in an LCE sample

The second material model that we simulate corresponds to the following strain-energy density function to capture necking in an LCE sample, which is given as

$$\begin{aligned}\mathcal{W} =& \frac{1}{2}\mu^{(1)}\left(\text{tr}\left[\text{Cof}\left(\boldsymbol{F}^T\boldsymbol{F}\right)\right]-3\right)+\frac{1}{2}\mu^{(2)}\left(\text{tr}\left(\boldsymbol{G}_0^2\boldsymbol{F}^T\boldsymbol{G}^{-2}\boldsymbol{F}\right)-3\right)\\ &+\frac{1}{2}K\,\text{Grad}\,\theta\cdot\text{Grad}\,\theta. \end{aligned} \tag{6.2}$$

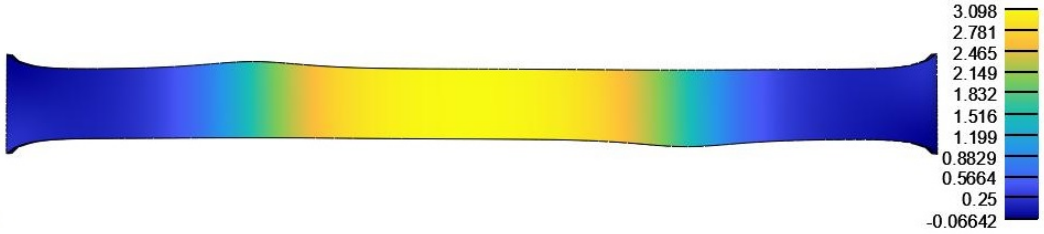
Unlike in the previous simulations, where the anisotropy parameter a was constant, here a varies with the deformation as

$$a = \frac{1+2Q}{1-Q}, \qquad Q = \frac{3}{4}(\lambda - 1)\,. \tag{6.3}$$

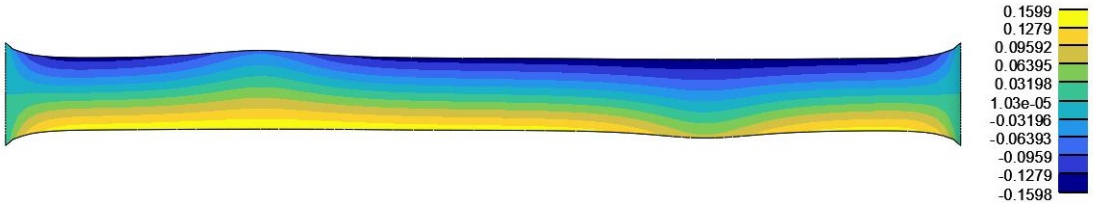
Then necking is observed when the sample is stretched (see figure 6.9). The formation of necking at the end of the sample agrees qualitatively with the experimental observations (see figure 1.2). The value of model coefficients are, in this case, $\mu^{(1)} = 1 \times 10^{-1}$ MPa, $\mu^{(1)} = 1$ MPa and $K = 1 \times 10^{-2}$N. The length of the undeformed sample is 5mm$\times$1mm and the initial director angle is $\theta_0 = 90^\circ$ to the stretch direction.



(a) Direction angle θ[rad] at the infinitesimal stretch.



(b) Director angle θ[rad] orientation after the formation of necking.



(c) Displacement $\boldsymbol{u}_y$[mm] in the Y-direction showing necking.

FIGURE 6.9: FE simulation of necking phenomena in LCE sample.

6.4 Simulation of the viscoelastic model

Within this section, we explore numerically the computer implementation of our viscoelastic LCE model to evaluate its performance. We simulate the response of an LCE sample under uniaxial tensile loading and unloading with various initial director angle. Frank's constant is $K = 10^{-11}$N, the bulk modulus is $B = 1000(\mu_{eq}^{(1)} + \mu_{eq}^{(2)})$ and small perturbations of 0.5° for the initial angles are used throughout the simulations. The numerical results compared with experimental data from [55] at different strain rates. The new model coefficients are calibrated to data sets using a nonlinear least squares procedure implemented in Matlab.

6.4.1 Vertical initial director

An LCE sample of length 30mm, width 6.1 mm, and thickness of 0.63mm [53] divided into 2500 elements is clamped at both ends then extended in the longitudinal direction under controlled displacement and various strain rate. Both loading and unloading conditions are considered. The equilibrium model coefficients are set to $\mu_{eq}^{(1)} = \mu_{eq}^{(2)} = 0.25$ MPa and the nonequilibrium model coefficients to $\mu_{neq}^{(1)} = \mu_{neq}^{(2)} = 2.5$ MPa, while the viscosity parameters are $\eta^{(1)} = 20$ MPa·s and $\eta^{(2)} = 200$ MPa·s. The anisotropy parameter is $a = 4.0$ (corresponding to $Q = 0.5$).

In figure 6.10, shear stripes form under longitudinal tensile loading. In one strip, the director rotates clockwise, while in the other strip, the director rotates anticlockwise.

The associated longitudinal first Piola-Kirchhoff stress as the stretch ratio changes in loading and unloading is plotted in figure 6.11. In this plot, a drop in longitudinal stress is observed when the stretch ratio is around $\lambda = 1.5$.

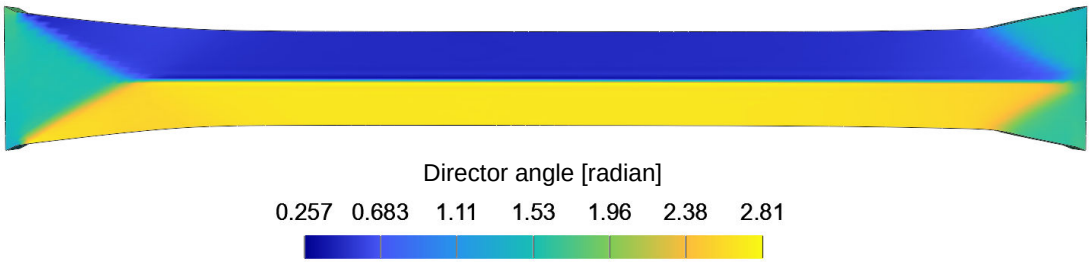


FIGURE 6.10: Shear striping developed in LCE sample with vertical initial director ($\theta_0 = 90°$) when extended horizontally at strain $\lambda - 1 = 0.5$ and strain rate $\dot{\lambda} = 0.1\%\,\mathrm{s}^{-1}$. In this simulation, $\mu_{eq}^{(1)} = \mu_{eq}^{(2)} = 0.25$ MPa, $\mu_{neq}^{(1)} = \mu_{neq}^{(2)} = 2.5$ MPa, $\eta^{(1)} = 20$ MPa·s, $\eta^{(2)} = 200$ MPa·s, and $a = 4.0$.

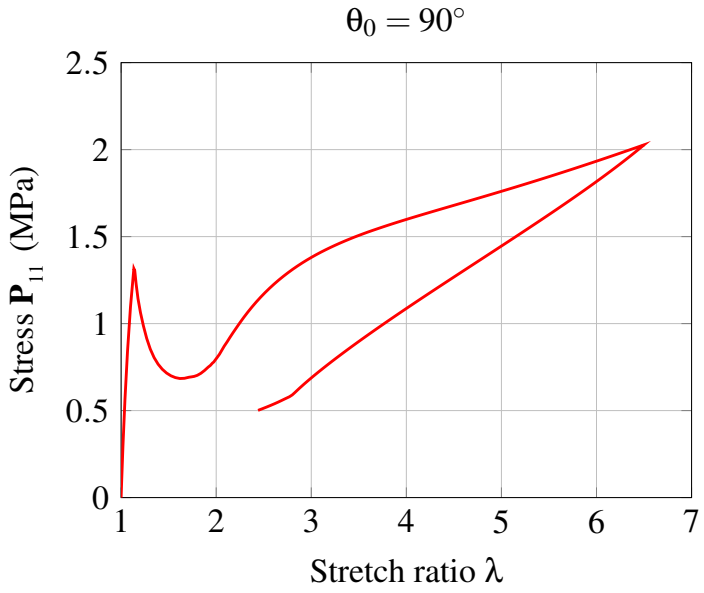


FIGURE 6.11: Finite element simulation results for the LCE sample response under uniaxial tensile loading and unloading perpendicularly to the initial director.

This is due to the director rotating instead of the polymeric network stretching, and the associated shear stripes forming to minimise energy.

6.4.2 Non-vertical initial director

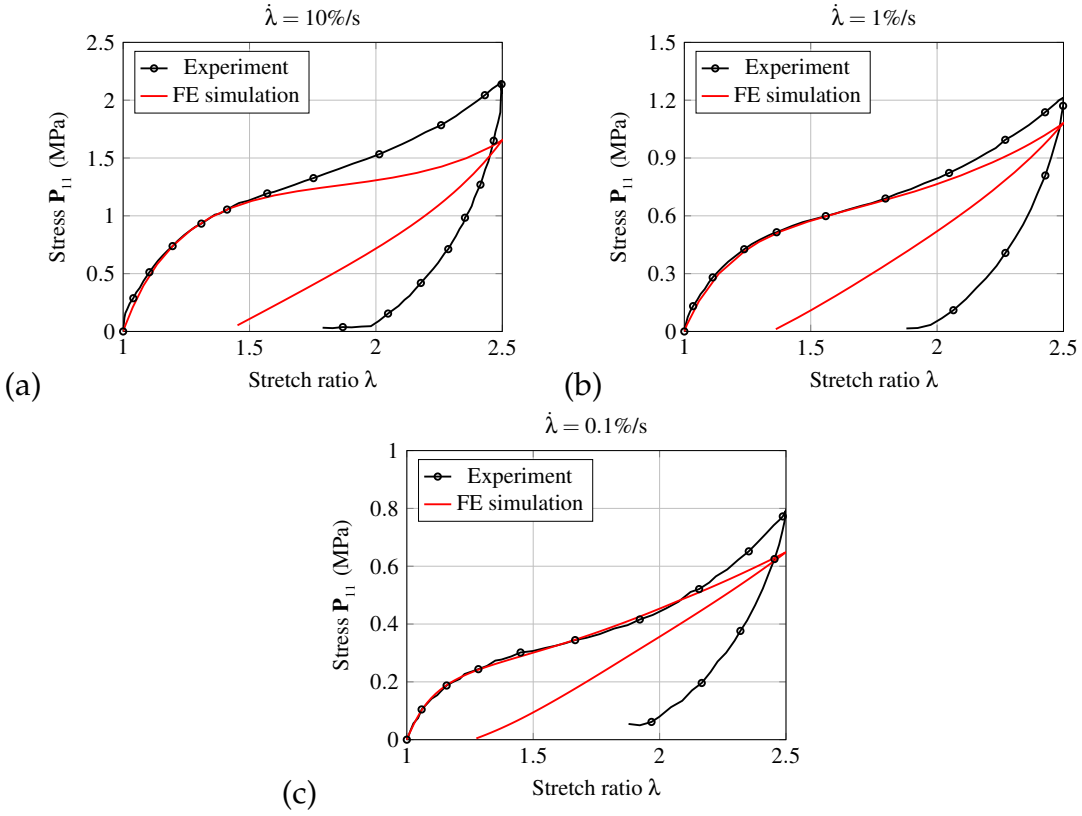


FIGURE 6.12: Finite element simulation results for the LCE sample response under uniaxial tensile loading and unloading when the initial director angle is $\theta_0 = 45°$ compared to experimental data [55] at different strain rates: (a) $\dot{\lambda} = 10\%$ s^{-1}, (b) $\dot{\lambda} = 1\%$ s^{-1} and (c) $\dot{\lambda} = 0.1\%$ s^{-1}.

LCE samples of length 30mm, width 5mm, thickness 0.3mm [55], and initial director angle $\theta_0 = 30°, 45°, 60°$ divided into 2500 elements were stretched at loading rates of 10% s^{-1}, 1% s^{-1}, and 0.1% s^{-1}, respectively. The material parameters were calibrated to the stress-strain response of the sample with an initial director $\theta_0 = 45°$ [55]. Although no equilibrium stress-strain relationship was available, equilibrium moduli $\mu_{eq}^{(1)} = 0.04$ MPa and $\mu_{eq}^{(2)} = 0.4$

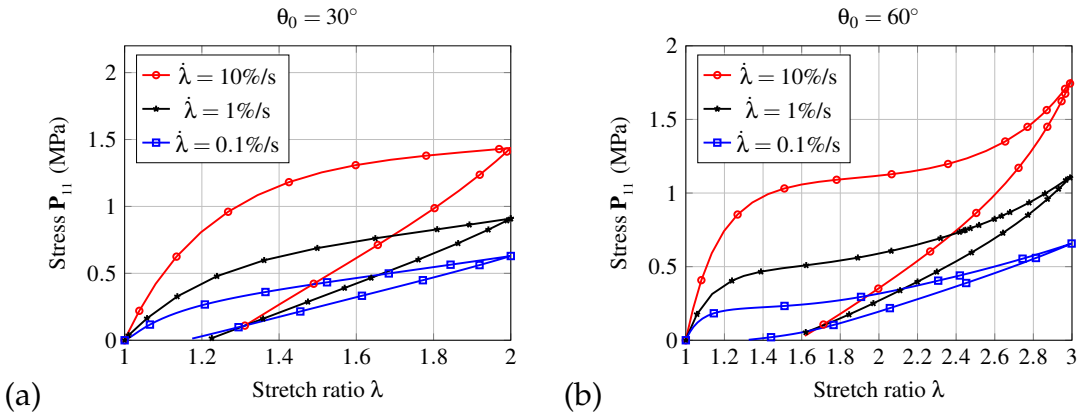


FIGURE 6.13: Finite element simulation results for the LCE sample response under uniaxial tensile loading and unloading at different strain rates when the initial director angle is equal to: (a) $\theta_0 = 30°$ and (b) $\theta_0 = 60°$.

MPa were chosen, assuming that the equilibrium stress stays lower than the one with strain rate of 0.1% s^{-1}. The values of the nonequilibrium modulus $\mu_{neq}^{(2)} = 0.1$ MPa and viscosity parameter $\eta^{(2)} = 10$ MPa·s were determined to match the graph. Different values for the nonequilibrium modulus $\mu_{neq}^{(1)}$ and viscosity parameter $\eta^{(1)}$ were obtained at different strain rates. The nematic parameter a was found to be linearly varying with the strain. As a corresponds to the current configuration, it means that molecular order evolves linearly with the deformation, in addition to director re-orientation. When the initial value was set to $a_0 = 5.5$ (corresponding the scalar order parameter of $Q_0 = 0.6$), this parameter reached a maximum value of $a_{\lambda max}$ at a maximum stretch ratio λ_{max} in the direction of the tensile load (this maximum stretch ratio may be different for different test samples with different initial director angle). When $\theta_0 = 45°$ and $\lambda_{max} = 2.5$, calibrated nonequilibrium modulus $\mu_{neq}^{(1)}$, viscosity parameter $\eta^{(1)}$, and maximum nematic parameter $a_{\lambda max}$ are recorded in Table 6.3 and the results are compared to the dataset in figure 6.12. Since we have employed a single Maxwell element on each branch, the model is restricted to a single relaxation time. Because physical

material exhibits relaxation across a spectrum of time scales, a single element cannot capture the multi-time scale response of the material resulting in rate-dependent material parameters. Incorporating multiple Maxwell elements in parallel introduce the multiple span of relaxation times enabling the model to capture the multi-time scale response while keeping the material parameters independent of the strain rate [96].

TABLE 6.3: Model parameters calibrated to experimental data for different strain rates.

$\dot{\lambda}$ (% s^{-1})	$\mu_{neq}^{(1)}$ (MPa)	$\eta^{(1)}$ (MPa·s)	a_0 (-)	$a_{\lambda max}$ (-)
10	1.8	70	5.5	1.5
1	1.0	250	5.5	2.0
0.1	0.65	750	5.5	3.0

Our LCE viscoelastic model demonstrates good agreement with the experimental data at lower strains. However, it tends to underestimate the stress at higher strain. This discrepancy is likely attributed to the use of a neo-Hookean-based model. Experiments [55] suggest a sharp increase in the stiffness of the LCE material as strain increases and eventually fracture of the sample. The neo-Hookean model does not take account of sample stiffening at higher rates and assumes that the sample can be stretched forever with constant stiffness.

Figure 6.12 shows the simulated results when the initial director angle is $\theta_0 = 45^\circ$, along with the experimental data. The results when $\theta_0 \in \{30^\circ, 60^\circ\}$ are shown in figure 6.13. We observe the three distinct regions in the graph. First, the LCE is relatively stiff with stress increasing linearly and steeply as stretch increases. With further stretch, the curve flattens into a plateau with little increase in stress relative to the stretch. This region is driven by director

rotation. Once the LC rotation is completed, stress is due to the stretching in the polymeric network. Then the LCE becomes stiffer again and the plotted curve turns upward.

The influence of various model parameters on the response of the uniaxially stretched LCE sample when $\theta_0 = 45^\circ$ at $\dot{\lambda} = 1\%\ \mathrm{s}^{-1}$ are discussed below. Due to the nonlinearity of the calibration problem, the optimal values of the calibrated parameters are not unique. This lack of uniqueness is expected as we are calibrating a non-linear model against a single experiment dataset. This occurs because a single loading condition is insufficient to decouple the distinct physical contribution of each material parameters. However, this limitation can be resolved by combining test results across different loading modes (eg. tension, shear, and compression), varied strain rate, and different boundary and initial conditions, which provides the mathematical constraints to find a unique set of material parameters. Setting $\mu_{eq}^{(1)} = 0.04$ MPa and $\mu_{eq}^{(2)} = 0.4$ MPa, the other parameters are as listed in table 6.3, except for those whose specific effect is being investigated.

Effect of anisotropy parameter a

The influence of the natural shape parameter a is shown in figure 6.14. Since this nematic parameter is related to the scalar uniaxial scalar order parameter Q, the stress plateaus for a in the interval where polymeric network extension is dominated by director rotation. In this semi-soft region, a higher shape parameter a (or higher order parameter Q) causes a lower stress response. Moreover, the semi-soft region starts earlier for a highly ordered sample (high a or high Q) and appears to hold the plateau for longer. It is seen in figure 6.14(a) that the residual strain is also larger when the nematic

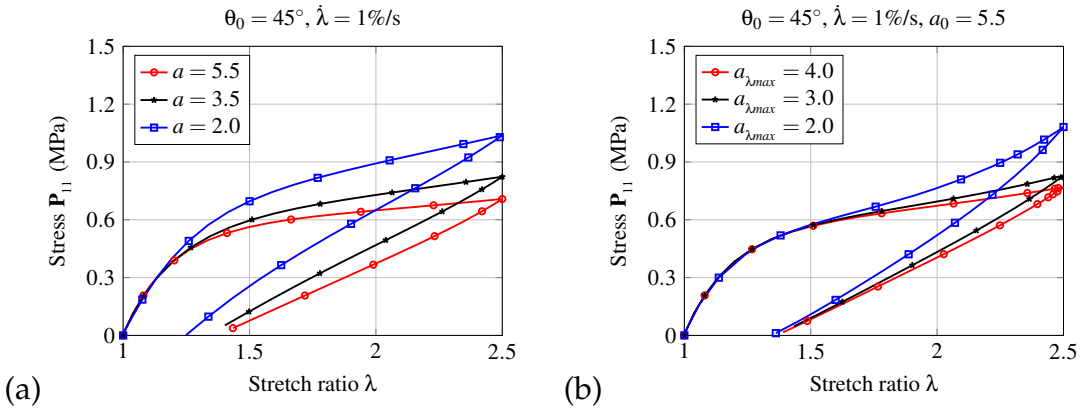


FIGURE 6.14: Finite element simulation results for the LCE sample response under uniaxial tensile loading and unloading when the initial director angle is $\theta_0 = 45^\circ$ at $\dot{\lambda} = 1\%\ \mathrm{s}^{-1}$ with model parameter values as recorded in Table 6.3 except for those listed in the legend: (a) constant shape parameter a and (b) linearly varying a when the reference value is $a_0 = 5.5$.

parameter a is larger. For experimental observations on nematic order variation with deformation, see for example [34].

Effect of constitutive parameters $\mu_{neq}^{(1)}$ and $\eta^{(1)}$ for viscous director rotation

Figures 6.15(a) and 6.15(b) show the influence of the nonequilibrium shear modulus $\mu_{neq}^{(1)}$ and viscosity parameter $\eta^{(1)}$, respectively. These constitutive parameters capture the viscous response due to director rotation. In particular, $\mu_{neq}^{(1)}$ dictates the relaxation rate of director rotation towards equilibrium. A higher $\mu_{neq}^{(1)}$ acts against the deformation so that the loading curve is higher. Also, the unloading curve is significantly lower compared to the loading curve, resulting in a wider hysteresis loop and larger residual strain for higher $\mu_{neq}^{(1)}$. It can be seen from the graph that a lower value of $\mu_{neq}^{(1)}$ leads to a thinner hysteresis curve, i.e., the director relaxes faster.

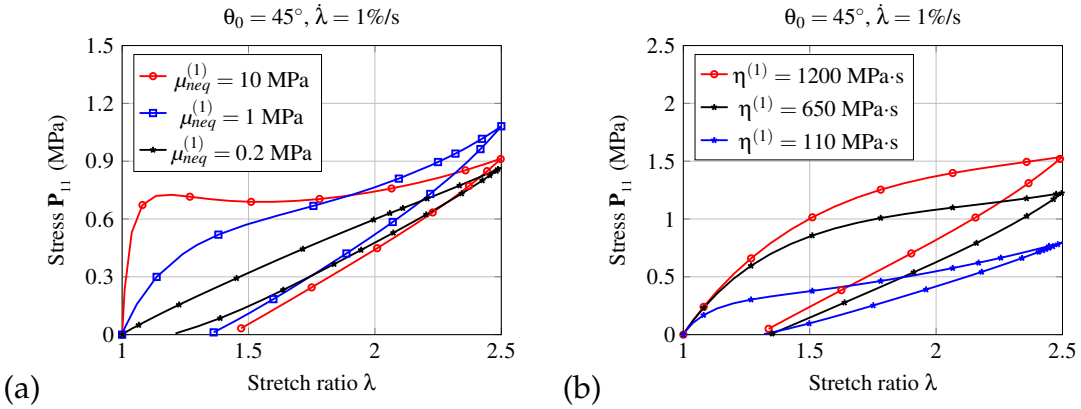


FIGURE 6.15: Finite element simulation results for the LCE sample response under uniaxial tensile loading and unloading when the initial director angle is $\theta_0 = 45°$ at $\dot{\lambda} = 1\%\ \mathrm{s}^{-1}$ with model parameter values as recorded in Table 6.3 except for those listed in the legend: (a) nonequilibrium shear modulus $\mu_{neq}^{(1)}$ and (b) viscosity parameter $\eta^{(1)}$.

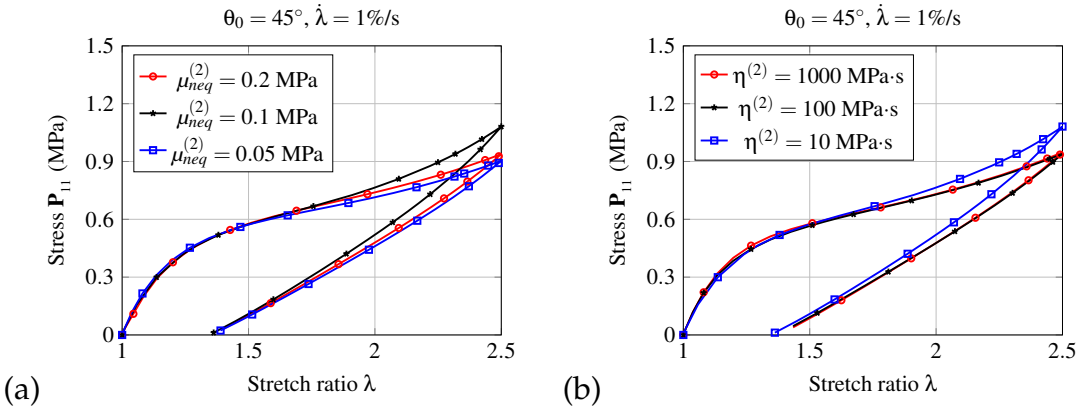


FIGURE 6.16: Results from the finite element simulation of uniaxial tension response of an LCE with initial director angle $\theta_0 = 45°$ at $\dot{\lambda} = 1\%\ \mathrm{s}^{-1}$ with model parameter values as recorded in Table 6.3 except for those listed in the legend: (a) nonequilibrium shear modulus $\mu_{neq}^{(2)}$ and (b) viscosity parameter $\eta^{(2)}$.

Effect of constitutive parameters $\mu_{neq}^{(2)}$ and $\eta^{(2)}$ for viscous polymer network

The effect of the nonequilibrium shear modulus $\mu_{neq}^{(2)}$ and viscosity parameter $\eta^{(2)}$ is shown in the figures 6.16(a) and 6.16(b), respectively. These model parameters describe the viscous response due to the network deformation. Since the experiment is mostly rotation dominated, i.e., the semi-soft region occupies the larger range, changes in these parameter cause little change in the stress response. Their effect is evident later when the network deformation becomes predominant and the director rotation is almost complete.

Chapter 7

Conclusion

Liquid crystal elastomers (LCEs) are soft materials in which liquid crystal (LC) rod-like molecules, known as mesogens, are covalently attached to a polymer network, typically through one end via a flexible spacer. Although anchored within the polymer matrix, these mesogens retain the ability to reorient, a property that is essential for the physical behaviour of LCEs and for the nematic–isotropic phase transition. Their reorientation can be triggered by external stimuli such as heat or light, leading to macroscopic shape changes in the material, but it can also arise from mechanical loading. Thus, deformation of the polymer network can influence the rotation of the LC director, and conversely, director rotation can affect the network deformation. For this reason, it is important to develop models that capture both processes and account for their distinct elastic and viscous responses.

In this thesis, we focus on the theoretical and computational modelling of the elastic and viscous behaviour in nematic LCEs subjected to mechanical loads, and combine the viscoelastic response of the polymeric network with the viscoelastic rotation of the nematic director. A finite element framework is devised and implemented to approximate the nonlinear elastic and viscoelastic behaviours computationally.

Within this modelling approach, we demonstrate both theoretically and numerically the occurrence of deformation localisation in nematic elastomers through two instability mechanisms: necking and shear striping, which can arise when certain nematic LCEs are subjected to uniaxial tensile stress. In the case of necking, the scalar uniaxial order parameter varies, reflecting the transition from polydomain to monodomain induced by mechanical stretching. In contrast, for shear striping the order parameter remains fixed, consistent with experimental observations. Our finite element simulations successfully capture both of these localisation phenomena and illustrate how different material parameters influence the response during loading and unloading.

The modelling framework presented here can be extended in several directions:

- The neo-Hookean-type components used in the present formulation of the viscoelastic LCE model can be replaced by other nonlinear constitutive functions within the same viscoelastic structure;
- The model can be enriched to incorporate additional couplings between mechanical forces and environmental stimuli;
- Our approach could be generalised to include probabilistic model parameters, which would provide a way to represent material variability [3].

These extensions would also increase the number of parameters that must be supported by reliable experimental evidence. Experimental investigations involving more complex loading conditions motivated by specific applications are therefore essential for a deeper understanding of these materials.

Appendix A

Stresses and their derivatives

This appendix contains details of the stresses and their derivatives for the strain-energy density used in this thesis. The stresses and their derivatives are derived using the standard continuum mechanics approach found in the book [97].

A.1 Strain-energy density function

$$\mathcal{W}^{(1)}(\boldsymbol{F}) = \frac{1}{2}\mu_1 \left(\mathrm{tr}\left(\boldsymbol{F}^T\boldsymbol{F}\right) - 3\right)$$
$$\mathcal{W}^{(2)}(\boldsymbol{F},\theta) = \frac{1}{2}\mu_2 \left(\mathrm{tr}\left(\boldsymbol{G}_0^2\boldsymbol{F}^T\boldsymbol{G}^{-2}\boldsymbol{F}\right) - 3\right)$$
$$\mathcal{W}^{(lce)}(\boldsymbol{F},\theta) = \mathcal{W}^{(1)} + \mathcal{W}^{(2)}$$
$$\mathcal{W}^{(3)}(\mathrm{Grad}\,\theta) = \frac{1}{2}K\,\mathrm{Grad}\,\theta\cdot\mathrm{Grad}\,\theta$$

Using the isochoric part $\tilde{\boldsymbol{F}} = J^{-\frac{1}{3}}\boldsymbol{F}$, we get

$$\tilde{\mathcal{W}}^{(1)} = \frac{1}{2}\mu_1 \left(\mathrm{tr}\left(\tilde{\boldsymbol{F}}^T\tilde{\boldsymbol{F}}\right) - 3\right)$$
$$\tilde{\mathcal{W}}^{(2)} = \frac{1}{2}\mu_2 \left(\mathrm{tr}\left(\boldsymbol{G}_0^2\tilde{\boldsymbol{F}}^T\boldsymbol{G}^{-2}\tilde{\boldsymbol{F}}\right) - 3\right)$$
$$\tilde{\mathcal{W}}^{(lce)} = \tilde{\mathcal{W}}^{(1)} + \tilde{\mathcal{W}}^{(2)}$$

Stresses

$$\boldsymbol{P} = \frac{\partial \tilde{\mathcal{W}}^{(lce)}}{\partial \boldsymbol{F}} + pJF^{-T} = \frac{\partial \tilde{\mathcal{W}}^{(1)}}{\partial \boldsymbol{F}} + \frac{\partial \tilde{\mathcal{W}}^{(2)}}{\partial \boldsymbol{F}} + pJ\boldsymbol{F}^{-T}$$
$$\frac{\partial \tilde{\mathcal{W}}^{(1)}}{\partial \boldsymbol{F}} = \mu_1 J^{-\frac{2}{3}} \left(-\frac{1}{3} \left(\boldsymbol{F} : \boldsymbol{F} \right) \boldsymbol{F}^T + \boldsymbol{F} \right)$$
$$\frac{\partial \tilde{\mathcal{W}}^{(2)}}{\partial \boldsymbol{F}} = \mu_2 J^{-\frac{2}{3}} \left(-\frac{1}{3} \left(\boldsymbol{F}\boldsymbol{G}_0^2 : \boldsymbol{G}^{-2}\boldsymbol{F} \right) \boldsymbol{F}^T + \boldsymbol{G}^{-2}\boldsymbol{F}\boldsymbol{G}_0^2 \right)$$

$$\begin{aligned} \boldsymbol{\pi}_\theta &= \frac{\partial W^{(3)}}{\partial \mathrm{Grad}\, \theta} \\ &= K\, \mathrm{Grad}\, \theta \end{aligned}$$

$$\begin{aligned} g_\theta &= -\frac{\partial \tilde{\mathcal{W}}^{(2)}}{\partial \theta} \\ &= -\frac{1}{2}\mu_2 \,\mathrm{tr} \left(\boldsymbol{G}_0^2 \tilde{\boldsymbol{F}}^T \frac{\partial \boldsymbol{G}^{-2}}{\partial \theta} \tilde{\boldsymbol{F}} \right) \end{aligned}$$

Derivative of stresses

$$\frac{\partial \boldsymbol{P}}{\partial \boldsymbol{F}} = \frac{\partial^2 \tilde{\mathcal{W}}^{(lce)}}{\partial \boldsymbol{F}^2} + p\frac{\partial JF^{-T}}{\partial \boldsymbol{F}} = \frac{\partial^2 \tilde{\mathcal{W}}^{(1)}}{\partial \boldsymbol{F}^2} + \frac{\partial^2 \tilde{\mathcal{W}}^{(2)}}{\partial \boldsymbol{F}^2} + p\frac{\partial J\boldsymbol{F}^{-T}}{\partial \boldsymbol{F}}$$
$$\frac{\partial^2 \tilde{\mathcal{W}}^{(1)}}{\partial \boldsymbol{F}^2} = \mu_1 J^{-\frac{2}{3}} \left(-\frac{1}{3} \left(\boldsymbol{F} : \boldsymbol{F} \right) \boldsymbol{F}^T + (\boldsymbol{I} \otimes \boldsymbol{I}) - \frac{2}{3} \frac{\partial \tilde{\mathcal{W}}^{(1)}}{\partial \boldsymbol{F}} \odot \boldsymbol{F}^{-T} \right)$$
$$\frac{\partial \tilde{\mathcal{W}}^{(2)}}{\partial \boldsymbol{F}} = \mu_2 J^{-\frac{2}{3}} \left(-\frac{1}{3} \left(\boldsymbol{F}\boldsymbol{G}_0^2 : \boldsymbol{G}^{-2}\boldsymbol{F} \right) \boldsymbol{F}^T + \left(\boldsymbol{G}^{-2} \otimes \boldsymbol{G}_0^2 \right) - \frac{2}{3} \frac{\partial \tilde{\mathcal{W}}^{(2)}}{\partial \boldsymbol{F}} \odot \boldsymbol{F}^{-T} \right)$$
$$\frac{\partial JF^{-T}}{\partial \boldsymbol{F}} = \left(\boldsymbol{F}^{-T} \odot \frac{\partial J}{\partial \boldsymbol{F}} \right) + J \left(-\boldsymbol{F}^{-T} \otimes \boldsymbol{F}^{-T} \right)^t$$

The definition of higher tensor product '$\otimes$' and '$\odot$' as well as that of transpose $(\cdot)^t$ are as defined in the book [97], which are

$$(\boldsymbol{A} \otimes \boldsymbol{B})_{ijkl} = A_{ik}B_{lj}$$

$$(\boldsymbol{A} \odot \boldsymbol{B})_{ijkl} = A_{ij}B_{kl}$$

$$(\boldsymbol{A} \otimes \boldsymbol{B})^t_{ijkl} = A_{il}B_{kj}$$

$$\begin{aligned}\frac{\partial \boldsymbol{P}}{\partial \theta} &= \frac{\partial}{\partial \theta}\left(\frac{\partial \tilde{\mathcal{W}}^{(2)}}{\partial \boldsymbol{F}}\right) \\ &= \mu_2 J^{-\frac{2}{3}}\left(-\frac{1}{3}\left(\boldsymbol{F}\boldsymbol{G}_0^2 : \boldsymbol{G}^{-2}\boldsymbol{F}\right)\boldsymbol{F}^T + \frac{\partial \boldsymbol{G}^{-2}}{\partial \boldsymbol{F}}\boldsymbol{G}_0^2\right)\end{aligned}$$

$$\frac{\partial g_\theta}{\partial \boldsymbol{F}} = -\frac{\partial \boldsymbol{P}}{\partial \theta}$$

$$\frac{\partial \boldsymbol{\pi}_\theta}{\partial \mathrm{Grad}\,\theta} = K\boldsymbol{I}$$

$$\begin{aligned}\frac{\partial g_\theta}{\partial \theta} &= -\frac{\partial}{\partial \theta}\left(\frac{\partial \tilde{\mathcal{W}}^{(2)}}{\partial \theta}\right) \\ &= -\frac{1}{2}\mu_2\,\mathrm{tr}\left(\boldsymbol{G}_0^2\tilde{\boldsymbol{F}}^T\frac{\partial^2 \boldsymbol{G}^{-2}}{\partial \theta^2}\tilde{\boldsymbol{F}}\right)\end{aligned}$$

Bibliography

[1] M. Warner and E. M. Terentjev. *Liquid Crystal Elastomers*. Oxford, UK: Oxford University Press, USA, 2007, p. 424. ISBN: 9780199214860.

[2] E. M. Terentjev. "Liquid crystal elastomers: 30 years after". In: *Macromolecules* 58 (2025), pp. 2792–2806. DOI: 10.1021/acs.macromol.4c01997.

[3] L. A. Mihai, D. Mistry, T. Raistrick, H. F. Gleeson, and A. Goriely. "A mathematical model for the auxetic response of liquid crystal elastomers". In: *Philosophical Transactions of the Royal Society A: Mathematical, Physical and Engineering Sciences* 380.2234 (Aug. 2022). DOI: 10.1098/rsta.2021.0326.

[4] P. G. de Gennes, M. Hébert, and R. Kant. "Artificial muscles based on nematic gels". In: *Macromolecular Symposia* 113 (1997), pp. 39–49. DOI: 10.1002/masy.19971130107.

[5] J. H. Kim, S. E. Lee, and B. H. Kim. "Applications of flexible and stretchable three-dimensional structures for soft electronics". In: *Soft Science* 3 (2023), p. 16. DOI: 10.20517/ss.2023.07.

[6] P. Rothemund, Y. Kim, R. H. Heisser, X. Zhao, R. F. Shepherd, and C. Keplinger. "Shaping the future of robotics through materials innovation". In: *Nature Materials* 20 (2021), pp. 1582–1587. DOI: 10.1038/s41563-021-01158-1.

[7] T. J. White and D. J. Broer. "Programmable and adaptive mechanics with liquid crystal polymer networks and elastomers". In: *Nature Materials* 14 (2015), pp. 1087–1098. DOI: 10.1038/nmat4433.

[8] E. Asgari, A. Robichaud, P. V. Cicek, and A. Shih. "Liquid crystal elastomers in soft micro electromechanical systems: a review of recent developments". In: *Journal of Material Chemistry C* 12 (2024), pp. 15359–15381. DOI: 10.1039/d4tc03282a.

[9] Z. C. Jiang, Q. Liu, Y. Y. Xiao, and Y. Zhao. "Liquid crystal elastomers for actuation: A perspective on structure-property-function relation". In: *Progress in Polymer Science* 153.11 (2024), p. 101829. DOI: 10.1016/j.progpolymsci.2024.101829.

[10] J. M. Speregen and T. J. White. "Liquid crystalline elastomers in soft robotics: assessing promise and limitations, Advanced Robotics Research, e202500150". 2025. DOI: 10.1002/adrr.202500150.

[11] T. Xiao, J. Wu, and Y. Zhang. "Recent advances in the design, fabrication, actuation mechanisms and applications of liquid crystal elastomers". In: *Soft Science* 3 (2024), p. 11. DOI: 10.20517/ss.2023.03.

[12] X. Tian, Y. Guo, O. M. Zhang J.and Ivasishin, J. Jia, and J. Yan. "Fiber Actuators Based on Reversible Thermal Responsive Liquid Crystal Elastomer". In: *Small* 20.24 (Jan. 2024). ISSN: 1613-6829. DOI: 10.1002/smll.202306952.

[13] Y. Zhu, Z. Ma, A. Sun, and Q. Wei. "Thermal responses of 3D-printed liquid crystal elastomer microcubes". In: *Liquid Crystals* 52.7–8 (May 2025), pp. 631–638. ISSN: 1366-5855. DOI: 10.1080/02678292.2025.2499853.

[14] S. Liu, K. Huang, K. Wang, and B. Wang. "Programmable deformation of liquid crystal elastomer plates subjected to concentrated light illumination". In: *Mechanics of Materials* 175 (Dec. 2022), p. 104501. ISSN: 0167-6636. DOI: 10.1016/j.mechmat.2022.104501.

[15] Y. Qiu, D. Ge, H. Wu, K. Li, and P. Xu. "Self-rotation of a liquid crystal elastomer rod under constant illumination". In: *International Journal of Mechanical Sciences* 283 (Dec. 2024), p. 109665. ISSN: 0020-7403. DOI: 10.1016/j.ijmecsci.2024.109665.

[16] Y. Qiu and K. Li. "Light-powered self-striking liquid crystal elastomer hammers inspired by mantis shrimp". In: *Communications in Nonlinear Science and Numerical Simulation* 146 (July 2025), p. 108802. ISSN: 1007-5704. DOI: 10.1016/j.cnsns.2025.108802.

[17] Y. Nemati, Q. Yang, F. Sohrabi, J. V. I. Timonen, C. Sánchez-Somolinos, M. Honkanen, H. Zeng, and A. Priimagi. "Magneto-Photochemically Responsive Liquid Crystal Elastomer for Underwater Actuation". In: *ACS Applied Materials & Interfaces* 17.3 (Jan. 2025), pp. 5316–5325. ISSN: 1944-8252. DOI: 10.1021/acsami.4c14704.

[18] L. A. Mihai. "A theoretical model for power generation via liquid crystal elastomers". In: *Mathematics and Mechanics of Solids* 29.6 (2023), pp. 1198–1215. DOI: 10.1177/10812865231193735.

[19] H. Zhao, Z. Chen, J. Li, Y. Luo, Z. Peng, G. Mao, R. Xiao, and J. Mao. "Spatiotemporally programmed dielectric liquid crystal elastomer: Electro-reversible 3D morphing via inverse 4D printing". In: *Science Advances* 11.48 (Nov. 2025). ISSN: 2375-2548. DOI: 10.1126/sciadv.aeb2289.

[20] S. M. Clarke and E. M. Terentjev. "Slow stress relaxation in randomly disordered nematic elastomers and gels". In: *Physical Review Letters* 81.20 (1998), pp. 4436–4439. DOI: 10.1103/PhysRevLett.81.4436.

[21] T. S. Hebner, C. N. Bowman, and T. J. White. "Influence of Orientational Genesis on the Actuation of Monodomain Liquid Crystalline Elastomers". In: *Macromolecules* 54.9 (Apr. 2021), pp. 4023–4029. ISSN: 1520-5835. DOI: 10.1021/acs.macromol.1c00437.

[22] J. Küpfer and H. Finkelmann. "Nematic liquid single crystal elastomers". In: *Die Makromolekulare Chemie, Rapid Communications* 12.12 (Dec. 1991), pp. 717–726. ISSN: 0173-2803. DOI: 10.1002/marc.1991.030121211.

[23] N. A. Traugutt, R. H. Volpe, M. S. Bollinger, M. O. Saed, A. H. Torbati, K. Yu, Natalia Dadivanyan, and C. M. Yakacki. "Liquid-crystal order during synthesis affects main-chain liquid-crystal elastomer behavior". In: *Soft Matter* 13.39 (2017), pp. 7013–7025. ISSN: 1744-6848. DOI: 10.1039/c7sm01405h.

[24] K. Urayama, E. Kohmon, M. Kojima, and T. Takigawa. "Polydomain-Monodomain Transition of Randomly Disordered Nematic Elastomers with Different Cross-Linking Histories". In: *Macromolecules* 42.12 (May 2009), pp. 4084–4089. ISSN: 1520-5835. DOI: 10.1021/ma9004692.

[25] G. R. Mitchell, F. Davis, and W. Guo. "Strain-induced transitions in liquid-crystal elastomers". In: *Physical Review Letters* 71 (1993), pp. 2947–2950. DOI: 10.1103/PhysRevLett.71.2947.

[26] I. Kundler and H. Finkelmann. "Strain-induced director reorientation in nematic liquid single crystal elastomers". In: *Macromolecular Rapid Communications* 16.9 (Sept. 1995), pp. 679–686. ISSN: 1521-3927. DOI: 10.1002/marc.1995.030160908.

[27] L. Golubović and T. C. Lubensky. "Nonlinear elasticity of amorphous solids". In: *Physical Review Letters* 63 (1989), pp. 1082–1085. DOI: 10.1103/PhysRevLett.63.1082.

[28] D. E. Carlson, E. Fried, and S. Sellers. "Force-free states, relative strain, and soft elasticity in nematic elastomers". In: *Journal of Elasticity* 69 (2002), pp. 161–180. DOI: 10.1023/A:1027377904576.

[29] H. Finkelmann, I. Kundler, E. M. Terentjev, and M. Warner. "Critical stripe-domain instability of nematic elastomers". In: *Journal de Physique* II.7 (1997), pp. 1059–1069. DOI: 10.1051/jp2:1997171.

[30] H. Higaki, T. Takigawa, and K. Urayama. "Nonuniform and Uniform Deformations of Stretched Nematic Elastomers". In: *Macromolecules* 46.13 (June 2013), pp. 5223–5231. ISSN: 1520-5835. DOI: 10.1021/ma400771z.

[31] I. Kundler and H. Finkelmann. "Director reorientation via stripe-domains in nematic elastomers: influence of cross-link density, anisotropy of the network and smectic clusters". In: *Macromolecular Chemistry and Physics* 199.4 (1998), pp. 677–686. DOI: 10.1002/(SICI)1521-3935(19980401)199:4%3C677::AID-MACP677%3E3.0.CO;2-E.

[32] A. Petelin and M. Čopič. "Observation of a soft mode of elastic instability in liquid crystal elastomers". In: *Physical Review Letters* 103 (2009), p. 077801. DOI: 10.1103/PhysRevLett.103.077801.

[33] A. Petelin and M. Čopič. "Strain dependence of the nematic fluctuation relaxation in liquid-crystal elastomerss". In: *Physical Review E* 82 (2010), p. 011703. DOI: 10.1103/PhysRevE.82.011703.

[34] R. V. Talroze, E. R. Zubarev, S. A. Kuptsov, A. S. Merekalov, T. I. Yuranova, N. A. Plate, and H. Finkelmann. "Liquid crystal acrylate-based networks: polymer backbone-LC order interaction". In: *Reactive and Functional Polymers* 41 (1999), pp. 1–11. DOI: 10.1016/S1381-5148(99)00032-2.

[35] E. R. Zubarev, S. A. Kuptsov, T. I. Yuranova, R. V. Talroze, and H. Finkelmann. "Monodomain liquid crystalline networks: reorientation mechanism from uniform to stripe domains". In: *Liquid Crystals* 26 (1999), pp. 1531–1540. DOI: 10.1080/026782999203869.

[36] P. Bladon, E. M. Terentjev, and M. Warner. "Transitions and instabilities in liquid crystal elastomers". In: *Physical Review E: Rapid Communications* 47.6 (1993), pp. 3838–3840. DOI: 10.1103/PhysRevE.47.R3838.

[37] P. Bladon, E. M. Terentjev, and M. Warner. "Deformation-induced orientational transitions in liquid crystal elastomers". In: *Journal de Physique* II.4 (1994), pp. 75–91. DOI: 10.1051/jp2:1994100.

[38] S. Conti. "Soft elastic response of stretched sheets of nematic elastomers: a numerical study". In: *Journal of the Mechanics and Physics of Solids* 50.7 (July 2002), pp. 1431–1451. DOI: 10.1016/s0022-5096(01)00120-x.

[39] A. DeSimone and G. Dolzmann. "Material instabilities in nematic elastomers". In: *Physica D: Nonlinear Phenomena* 136.1-2 (2000), pp. 175–191. DOI: S0167-2789(99)00153-0.

[40] A. DeSimone and L. Teresi. "Elastic energies for nematic elastomers". In: *The European Physical Journal E* 29.2 (June 2009), pp. 191–204. DOI: 10.1140/epje/i2009-10467-9.

[41] E. Fried and S. Sellers. "Free-energy density functions for nematic elastomers". In: *Journal of the Mechanics and Physics of Solids* 52.7 (2004), pp. 1671–1689. DOI: 10.1016/j.jmps.2003.12.005.

[42] E. Fried and S. Sellers. "Orientational order and finite strain in nematic elastomers". In: *The Journal of Chemical Physics* 123.4 (2005), p. 043521. DOI: 10.1063/1.1979479.

[43] E. Fried and S. Sellers. "Soft elasticity is not necessary for striping in nematic elastomers". In: *Journal of Applied Physics* 100.4 (Aug. 2006), p. 043521. DOI: 10.1063/1.2234824.

[44] L. A. Mihai and A. Goriely. "Likely striping in stochastic nematic elastomers". In: *Mathematics and Mechanics of Solids* 25.10 (May 2020), pp. 1851–1872. ISSN: 1741-3028. DOI: 10.1177/1081286520914958.

[45] L. A. Mihai and A. Goriely. "Instabilities in liquid crystal elastomers". In: *MRS Bulletin* 46.9 (June 2021), pp. 784–794. ISSN: 1938-1425. DOI: 10.1557/s43577-021-00115-2.

[46] B. L. Mbanga, F. Ye, J. V. Selinger, and R. L. Selinger. "Modeling elastic instabilities in nematic elastomers". In: *Physical Review E* 82.5 (2010), p. 051701. DOI: 10.1103/PhysRevE.82.051701.

[47] M. Soltani, K. Raahemifar, A. Nokhosteen, F. M. Kashkooli, and E. L. Zoudani. "Numerical Methods in Studies of Liquid Crystal Elastomers". In: *Polymers* 13.10 (May 2021), p. 1650. DOI: 10.3390/polym13101650.

[48] X. He, Y. Zheng, Q. He, and S. Cai. "Uniaxial tension of a nematic elastomer with inclined mesogens". In: *Extreme Mechanics Letters* 40 (Oct. 2020), p. 100936. ISSN: 2352-4316. DOI: 10.1016/j.eml.2020.100936.

[49] M. Li, Y. Yan, S. Xu, G. Wang, J. Wu, and X. Q. Feng. "Surface effect on the necking of hyperelastic materials". In: *Current Applied Physics* 38 (2022), pp. 91–98. DOI: 10.1016/j.cap.2022.03.010.

[50] L. R. G. Treloar. "Stress-strain data for vulcanized rubber under various types of deformation". In: *Transactions of the Faraday Society* 40 (1944), pp. 59–70. DOI: 10.1039/TF9444000059.

[51] A. Azoug, V. Vasconcellos, J. Dooling, M. Saed, C. M. Yakacki, and T. D. Nguyen. "Viscoelasticity of the polydomain-monodomain transition in main-chain liquid crystal elastomers". In: *Polymer* 98 (Aug. 2016), pp. 165–171. ISSN: 0032-3861. DOI: 10.1016/j.polymer.2016.06.022.

[52] A. Hotta and E. M. Terentjev. "Long-time stress relaxation in polyacrylate nematic liquid crystalline elastomers". In: *Journal of Physics: Condensed Matter* 13.50 (Nov. 2001), pp. 11453–11464. ISSN: 1361-648X. DOI: 10.1088/0953-8984/13/50/305.

[53] C. P. Martin Linares, N. A. Traugutt, M. O. Saed, A. Martin Linares, C. M. Yakacki, and T. D. Nguyen. "The effect of alignment on the rate-dependent behavior of a main-chain liquid crystal elastomer". In: *Soft Matter* 16.38 (2020), pp. 8782–8798. ISSN: 1744-6848. DOI: 10.1039/d0sm00125b.

[54] D. R. Merkel, Rajib K. Shaha, Christopher M. Yakacki, and Carl P. Frick. "Mechanical energy dissipation in polydomain nematic liquid crystal elastomers in response to oscillating loading". In: *Polymer* 166 (Mar. 2019), pp. 148–154. ISSN: 0032-3861. DOI: 10.1016/j.polymer.2019.01.042.

[55] C. Wei, S. Cao, Y. Zhou, D. Lin, and L. Jin. "Rate-dependent stress-order coupling in main-chain liquid crystal elastomers". In: *Soft Matter* 19.41 (2023), pp. 7923–7936. ISSN: 1744-6848. DOI: 10.1039/d3sm00770g.

[56] S. Paparini, G. G. Giusteri, and L. A. Mihai. "Shape instabilities driven by topological defects in nematic polymer networks". In: *Journal of Elasticity* 157 (2025), p. 69. DOI: 10.1007/s10659-025-10160-6.

[57] R. Poudel, Y. Şengül, and L. A. Mihai. "Deformation localisation in stretched liquid crystal elastomers". In: *Mechanics of Soft Materials* 6.1 (Oct. 2024), p. 8. ISSN: 2524-5619. DOI: 10.1007/s42558-024-00063-2.

[58] T. Sato and K. Yoshimoto. "Recent developments on multiscale simulations for rheology and complex flow of polymers". In: *Korea-Australia Rheology Journal* 36.4 (Oct. 2024), pp. 253–269. ISSN: 2093-7660. DOI: 10.1007/s13367-024-00112-2.

[59] Z. Yang and Z. Meng. "A Review of Computational Modeling of Polymer Composites and Nanocomposites". In: *Polymers* 18.4 (Feb. 2026), p. 443. ISSN: 2073-4360. DOI: 10.3390/polym18040443.

[60] S. M. Clarke and E. M. Terentjev. "Slow stress relaxation in liquid crystal elastomers and gels". In: *Faraday Discussions* 112 (1999), pp. 325–333. DOI: 10.1039/a808847k.

[61] P. Martinoty, P. Stein, H. Finkelmann, H. Pleiner, and H. R. Brand. "Mechanical properties of mono-domain side chain nematic elastomers". In: *European Physics Journal E - Soft Matter* 14.4 (2004), pp. 311–321. DOI: 10.1140/epje/i2003-10154-y.

[62] K. Urayama, S. Honda, and T. Takigawa. "Slow dynamics of shape recovery of disordered nematic elastomers". In: *Physical Review E* 74.4 (Oct. 2006), p. 041709. ISSN: 1550-2376. DOI: 10.1103/physreve.74.041709.

[63] A. E. H. Chehade, B. Shen, C. M. Yakacki, T. D. Nguyen, and S. Govindjee. "Finite element modeling of viscoelastic liquid crystal elastomers". In: *International Journal for Numerical Methods in Engineering* 125.16 (May 2024), e7510. ISSN: 1097-0207. DOI: 10.1002/nme.7510.

[64] Z. Wang, A. E. H. Chehade, S. Govindjee, and T. D. Nguyen. "A nonlinear viscoelasticity theory for nematic liquid crystal elastomers". In: *Journal of the Mechanics and Physics of Solids* 163 (June 2022), p. 104829. DOI: 10.1016/j.jmps.2022.104829.

[65] C. Chung, C. Luo, C. M. Yakacki, B. Song, K. Long, and K. Yu. "Revealing the unusual rate-dependent mechanical behaviors of nematic liquid crystal elastomers". In: *International Journal of Solids and Structures* 292 (Apr. 2024), p. 112712. ISSN: 0020-7683. DOI: 10.1016/j.ijsolstr.2024.112712.

[66] Y. Jiang, Z. Xu, R. Xiao, S. Govindjee, and T. D. Nguyen. "A viscoelastic micro-stretch theory for monodomain nematic liquid crystal elastomers". In: *Journal of the Mechanics and Physics of Solids* 207 (2025), p. 106412. DOI: 10.1016/j.jmps.2025.106412.

[67] Y. Zhou, C. Wei, and L. Jin. "A modified semi-soft model of liquid crystal elastomers: Application to elastic and viscoelastic responses". In: *Journal of the Mechanics and Physics of Solids* 196 (Mar. 2025), p. 106027. ISSN: 0022-5096. DOI: 10.1016/j.jmps.2025.106027.

[68] F. Concas and M. Groß. "Dynamic large strain formulation for nematic liquid crystal elastomers". In: *Continuum Mechanics and Thermodynamics* 36 (May 2024), pp. 969–992. ISSN: 1432-0959. DOI: 10.1007/s00161-024-01307-2.

[69] S. A. Maas, B. J. Ellis, G. A. Ateshian, and J. A. Weiss. "FEBio: Finite Elements for Biomechanics". In: *Journal of Biomechanical Engineering* 134.1 (Jan. 2012). ISSN: 1528-8951. DOI: 10.1115/1.4005694.

[70] R. Poudel, Y. Şengül, and L. A. Mihai. "A numerical model for the viscoelastic behaviour of liquid crystal elastomers". In: *Engineering with Computers* 42.4 (2026). ISSN: 1435-5663. DOI: 10.1007/s00366-026-02352-y.

[71] N. Mahardika, T. Raistrick, and H. Mihai L. A.and Wang. "All-atom molecular dynamics simulations of nematic liquid crystal elastomers". In: *International Journal of Solids and Structures* 291 (Apr. 2024), p. 112717. ISSN: 0020-7683. DOI: 10.1016/j.ijsolstr.2024.112717.

[72] E. M. Terentjev. "Liquid-crystalline elastomers". In: *Journal of Physics: Condensed Matter* 11.24 (Jan. 1999), R239–R257. DOI: 10.1088/0953-8984/11/24/201.

[73] S. Chandrasekhar. *Liquid Crystals*. Title from publisher's bibliographic system (viewed on 05 Oct 2015). Cambridge: Cambridge University Press, 1992. 1480 pp. ISBN: 9780511622496.

[74] P. G. de Gennes. *The physics of liquid crystals.* 2nd ed. Oxford: Clarendon Press, 1995, p. 597. ISBN: 0198517858.

[75] G. A. Holzapfel. *Nonlinear Solid Mechanics. A Continuum Approach for Engineering*. Wiley, 2000, p. 455. ISBN: 9780471823193.

[76] V. A. Eremeyev, L. P. Lebedev, and H. Altenbach. *Foundations of Micropolar Mechanics*. Heidelberg: Springer Berlin Heidelberg, 2013. ISBN: 9783642283536. DOI: 10.1007/978-3-642-28353-6.

[77] C. Truesdell and R. Toupin. "The Classical Field Theories". In: *Principles of Classical Mechanics and Field Theory / Prinzipien der Klassischen Mechanik und Feldtheorie*. Springer Berlin Heidelberg, 1960, pp. 226–858. ISBN: 9783642459436. DOI: 10.1007/978-3-642-45943-6_2.

[78] B. D. Coleman and W. Noll. "The thermodynamics of elastic materials with heat conduction and viscosity". In: *Archive for Rational Mechanics and Analysis* 13.1 (Dec. 1963), pp. 167–178. ISSN: 1432-0673. DOI: 10.1007/bf01262690.

[79] J. Küpfer and H. Finkelmann. "Liquid crystal elastomers: Influence of the orientational distribution of the crosslinks on the phase behaviour and reorientation processes". In: *Macromolecular Chemistry and Physics* 195.4 (Apr. 1994), pp. 1353–1367. ISSN: 1521-3935. DOI: 10.1002/macp.1994.021950419.

[80] G. C. Verwey, M. Warner, and E. M. Terentjev. "Elastic Instability and Stripe Domains in Liquid Crystalline Elastomers". In: *Journal de Physique II* 6.9 (Sept. 1996), pp. 1273–1290. DOI: 10.1051/jp2:1996130.

[81] L. A. Mihai. *Stochastic Elasticity. A Nondeterministic Approach to the Nonlinear Field Theory*. Cham, Switzerland: Springer International Publishing, 2022. DOI: 10.1007/978-3-031-06692-4.

[82] S. V. Fridrikh and E. M. Terentjev. "Polydomain-monodomain transition in nematic elastomers". In: *Physical Review E* 60.2 (Aug. 1999), pp. 1847–1857. ISSN: 1095-3787. DOI: 10.1103/physreve.60.1847.

[83] J. Sivaloganathan and S. J. Spector. "On the Stability of Incompressible Elastic Cylinders in Uniaxial Extension". In: *Journal of Elasticity* 105.1–2 (Mar. 2011), pp. 313–330. ISSN: 1573-2681. DOI: 10.1007/s10659-011-9330-9.

[84] S. Okamoto, S. Sakurai, and K. Urayama. "Effect of stretching angle on the stress plateau behavior of main-chain liquid crystal elastomers". In: *Soft Matter* 17.11 (2021), pp. 3128–3136. ISSN: 1744-6848. DOI: 10.1039/d0sm02244f.

[85] A. Fukunaga, K. Urayama, T. Takigawa, A. DeSimone, and L. Teresi. "Dynamics of Electro-Opto-Mechanical Effects in Swollen Nematic Elastomers". In: *Macromolecules* 41.23 (Nov. 2008), pp. 9389–9396. ISSN: 1520-5835. DOI: 10.1021/ma801639j.

[86] S. Reese and S. Govindjee. "A theory of finite viscoelasticity and numerical aspects". In: *International Journal of Solids and Structures* 35.26–27 (Sept. 1998), pp. 3455–3482. ISSN: 0020-7683. DOI: 10.1016/s0020-7683(97)00217-5.

[87] G. Destrade M.and Saccomandi and I. Sgura. "Methodical fitting for mathematical models of rubber-like materials". In: *Proceedings of the Royal Society A: Mathematical, Physical and Engineering Sciences* 473.2198 (Feb. 2017), p. 20160811. ISSN: 1471-2946. DOI: 10.1098/rspa.2016.0811.

[88] O. C. Zienkiewicz. *Finite Element Method. Its Basis and Fundamentals*. Ed. by Robert L. Taylor, Jianzhong Zhu, and Olek C Zienkiewicz. 7th ed. The Finite Element Method Ser. Oxford: Elsevier Science and Technology, 2013. 1753 pp. ISBN: 9780080951355.

[89] D. R. Anderson, D. E. Carlson, and E. Fried. "A Continuum-Mechanical Theory for Nematic Elastomers". In: *Journal of Elasticity* 56.1 (1999), pp. 33–58. DOI: 10.1023/a:1007647913363.

[90] J. N. Reddy. *Energy principles and variational methods in applied mechanics*. Third edition. Newark: John Wiley and Sons, Incorporated, 2017. 1973 pp. ISBN: 9781119087397.

[91] T. J. R. Hughes, ed. *The finite element method. Linear static and dynamic finite element analysis*. Mineola, NY: Dover Publications, 2000. 682 pp. ISBN: 1621985881.

[92] J. C. Simo, R. L. Taylor, and K. S. Pister. "Variational and projection methods for the volume constraint in finite deformation elasto-plasticity". In: *Computer Methods in Applied Mechanics and Engineering* 51.1–3 (Sept. 1985), pp. 177–208. ISSN: 0045-7825. DOI: 10.1016/0045-7825(85)90033-7.

[93] J. C. Simo. "On a fully three-dimensional finite-strain viscoelastic damage model: Formulation and computational aspects". In: *Computer Methods in Applied Mechanics and Engineering* 60.2 (Feb. 1987), pp. 153–173. ISSN: 0045-7825. DOI: 10.1016/0045-7825(87)90107-1.

[94] P. Wriggers. *Nonlinear Finite Element Methods*. Berlin, Heidelberg: Springer Berlin / Heidelberg, 2008. 1566 pp. ISBN: 9783540710011.

[95] J. Bonet and R. D. Wood. *Nonlinear Continuum Mechanics for Finite Element Analysis*. Cambridge: Cambridge University Press, Mar. 2008. ISBN: 9780511755446. DOI: 10.1017/cbo9780511755446.

[96] John D. Ferry. *Viscoelastic properties of polymers*. 3. ed. New York [u.a.]: Wiley, 1980. 641 pp. ISBN: 9780471048947.

[97] M. Itskov. *Tensor Algebra and Tensor Analysis for Engineers: With Applications to Continuum Mechanics*. Springer International Publishing, 2019. ISBN: 9783319988061. DOI: 10.1007/978-3-319-98806-1.